

PHASE FIELD MODELING OF CRACK GROWTH IN SHAPE MEMORY  
CERAMICS

by

Ehsan Moshkelgosh



A dissertation

submitted in partial fulfillment

of the requirements for the degree of

Doctor of Philosophy in Materials Science and Engineering

Boise State University

May 2021

© 2021

Ehsan Moshkelgosha

ALL RIGHTS RESERVED

BOISE STATE UNIVERSITY GRADUATE COLLEGE

**DEFENSE COMMITTEE AND FINAL READING APPROVALS**

of the dissertation submitted by

Ehsan Moshkelgosha

Dissertation Title: Phase Field Modeling of Crack Growth in Shape Memory Ceramics

Date of Final Oral Examination: 07 April 2021

The following individuals read and discussed the dissertation submitted by student Ehsan Moshkelgosha, and they evaluated their presentation and response to questions during the final oral examination. They found that the student passed the final oral examination.

Mahmood Mamivand, Ph.D. Chair, Supervisory Committee

Peter Mullner, Ph.D. Member, Supervisory Committee

Brian Jaques, Ph.D. Member, Supervisory Committee

Mohsen Asle Zaem, Ph.D. External Committee Member

The final reading approval of the dissertation was granted by Mahmood Mamivand, Ph.D., Chair of the Supervisory Committee. The dissertation was approved by the Graduate College.

DEDICATION

*To the loving memory of my mother*  
*Thank you for loving me and helping me*  
*I miss you dearly*  
*You are always in my heart*

## ACKNOWLEDGMENTS

I would like to thank my advisor Dr. Mahmood Mamivand for all his trust, encouragement, and supports. I am sincerely honored and grateful for all the knowledge and support I received from him throughout my research. His valuable advice has benefited me significantly during my research career.

I would also like to thank Dr. Peter Mullner, Dr. Brian Jaques, and Dr. Mohsen Asle Zaeem for serving as my committee members. A special thanks to my family for all the prayers and sacrifices they made to me. I strongly believe all I have in my life is because of their prayers.

Finally, my biggest thank would go to my adorable wife, Maryam, for the love and peace that she gave me. Unless she provided me a warm and lovely family, I would not reach any of my goals during my Ph.D.

## ABSTRACT

Shape memory ceramics (SMCs) are promising candidates for actuators in extreme environments such as high temperature and corrosive applications. Despite outstanding energy dissipation, compared to metallic shape memory materials, SMCs suffer from a sudden brittle fracture. While the interaction of crack propagation and phase transformation in SMCs has been the subject of several experimental and theoretical studies, mainly at the macroscale, the fundamental understanding of the dynamic interaction of crack propagation and martensitic transformation is poorly understood. This dissertation attempts to provide a mathematical model for crack propagation in transformable zirconia to address the shortage of classical methods. This dissertation uses the phase field framework to fully couple the martensitic transformation to the variational formulation of brittle fracture.

Firstly, the model is parameterized for single crystal zirconia, which experiences tetragonal to monoclinic transformation during crack propagation. For mode I of fracture, the opening mode, crack shows an unusual propagation path that is in good agreement with the experiments and indicates the significant role of phase transformation on the crack propagation path. The investigation on the effect of lattice orientation on crack propagation shows that the lattice orientation has a significant influence not only on the crack propagation path but also on the magnitude of the transformation toughening.

Secondly, the model is parameterized for tetragonal polycrystalline zirconia, and the experimental data from literature were used to validate the model. The model predicts

the three dominant crack propagation patterns which were observed experimentally, including the secondary crack initiation, crack branching, and grain bridging. The model shows the critical role of texture engineering in toughening enhancement. Polycrystalline zirconia samples with grains that make low angles between the a-axis in the tetragonal phase and the crack plane, show higher transformation toughening, due to maximum hydrostatic strain release perpendicular to the crack tip. The model also shows the grain boundary engineering as a way to enhance the transformation toughening. The maximum fracture toughness occurs at a specific grain size, and further coarsening or refinement reduces the fracture toughness. This optimum grain size is the consequence of the competition between the toughening enhancement and MT suppression with grain refinement.

Finally, we parameterized the model for the 3D single crystal zirconia, which experienced stress- and thermal-induced tetragonal to monoclinic transformation. The developed 3D model considers all 12 monoclinic variants, making it possible to acquire realistic microstructures. Surface uplifting, self-accommodated martensite pairs formation, and transformed zone fragmentation were observed by the model, which agrees with the experimental observations. The influence of the crystal lattice orientation is investigated in this study, which reveals its profound effects on the transformation toughening and crack propagation path.

## TABLE OF CONTENTS

DEDICATION.....	iv
ACKNOWLEDGMENTS.....	v
ABSTRACT .....	vi
LIST OF TABLES .....	x
LIST OF FIGURES .....	xi
LIST OF ABBREVIATIONS.....	xv
CHAPTER ONE: INTRODUCTION.....	1
CHAPTER TWO: METHODS.....	8
Phase Field Method .....	8
PF Modeling of the T→M Transformation .....	12
Chemical Free Energy.....	14
Elastic Strain Energy.....	15
The Variational Formulation for PF Modeling of Crack Growth.....	16
Theory of Brittle Fracture.....	18
Phase Field Approximation for Fracture Energy.....	19
Combining the Variational Formulation of Crack Growth and the T→M Transformation.....	21
CHAPTER THREE: SINGLE CRYSTAL MODEL.....	24
Result .....	24
Model Verification .....	27



Temporal and Spatial Evolution of Concurrent T→M Transformation and Crack Propagation in A Single Crystal Tetragonal Zirconia.....	28
The Effect of Crystal Lattice Orientation.....	31
Crack Propagation in Transformable Versus Untransformable Zirconia .....	35
Conclusion.....	40
CHAPTER FOUR: POLYCRYSTALLINE MODEL .....	42
Polycrystalline Model Generation .....	42
Results .....	43
Model Verification.....	46
Temporal and Spatial Evolution of Concurrent T→M Transformation and Crack Propagation in Polycrystalline Zirconia.....	51
The Effects of Lattice Orientation .....	59
The Effects of The Grain Size on The Fracture of Polycrystalline Zirconia .....	67
The Effects of Grain Boundaries Strength .....	71
Conclusion.....	74
CHAPTER FIVE: THREE-DIMENSIONAL MODEL.....	75
Crystallography of Tetragonal to Monoclinic Transformation in Zirconia .....	75
Results .....	77
Model Verification.....	79
Temporal and Spatial Evolution of Crack Propagation in Transformable Domains .....	81
The Effects of Crystal Lattice Orientation .....	84
Conclusion.....	91
CHAPTER SIX: CONCLUSION AND FUTURE WORKS .....	93
REFERENCES.....	97

## LIST OF TABLES

Table 1.	Elastic constants for monoclinic zirconia (GPa) [49].	26
Table 2.	Elastic constants for tetragonal zirconia (GPa) [49].	26
Table 3.	Numerical values used for calculation.	26
Table 4.	Monoclinic zirconia elastic constants (Gpa) [49].	45
Table 5.	Tetragonal zirconia elastic constants (Gpa) [49,100].	45
Table 6.	Numerical parameters utilized in the model calculations.	45
Table 7.	Parameters applied in the model.	78

## LIST OF FIGURES

Figure 1.	(a) Diffuse interface: properties evolve continuously between their equilibrium values in the neighboring grains. (b) Sharp interface: properties are discontinuous at the interface.[74] .....11
Figure 2.	Schematic illustration of possible variants of the monoclinic phase during t→m transformation in 2D [75]. .....13
Figure 3.	Phase field approximation of the crack surface. In PF modeling of crack growth, we use the PF variable $\phi(\mathbf{r}, t) \in [0, 1]$ as the order parameter, with $\phi = 1$ shows the crack and $\phi = 0$ indicates that the body is uncracked. ....18
Figure 4.	The geometry and boundary conditions of a single-edge-notched square plate subjected to tension loading. ....25
Figure 5.	Comparison of the coupled PF simulation of martensitic transformation and crack propagation result with the experiment [20,70]. ....27
Figure 6.	The co-evolution of t→m transformation and crack propagation in zirconia under the mode I loading for lattice orientation angle of zero degrees, $\theta = 0^\circ$ . ....29
Figure 7.	The stress–strain curve for single crystal tetragonal zirconia under uniaxial tension and its corresponding microstructure evolution and deformed shapes.....30
Figure 8.	The effect of crystal lattice orientation on the crack growth in a single crystal tetragonal zirconia under the mode I loading. The left and right columns show the concurrent evolution of t→m transformation and crack growth at the times of 600 s and 3500 s, respectively. ....33
Figure 9.	The stress-strain curve for crack growth in tetragonal zirconia single crystal with different lattice orientation angles. The loading rate and simulation time are consistent for all simulations. Lattice orientations of $50^\circ$ and $90^\circ$ show the maximum and minimum transformation toughening, respectively. ....35

Figure 10.	The comparison between crack propagation in single crystal tetragonal zirconia with and without phase transformation. The left column shows the crack propagation in untransformable zirconia (phase transformation is artificially turned off), the middle column shows the crack growth in transformable zirconia, and the right column shows the corresponding microstructure for the transformable case. ....	36
Figure 11.	The stress-strain curve for transformable and untransformable single crystal tetragonal zirconia upon loading to crack growth initiation. ....	37
Figure 12.	Comparisons between crack propagation path in elastic isotropic, elastic anisotropic, and transformable elastic anisotropic models show that the MT is the dominant physics in SMCs cracking. ....	39
Figure 13.	Energy release rate versus crack extension for a single crystal zirconia for $\sigma=900$ and 1100 MPa. Dynamic evolution of the microstructure during the crack propagation and its associated toughening effects, lead to higher energy release rate for 900 MPa compared to 1100 MPa for crack extensions between 120 nm to 250 nm. ....	40
Figure 14.	Algorithm of polycrystalline geometry and mesh generation with distinct internal grain boundaries. ....	43
Figure 15.	The geometry and boundary conditions of the polycrystalline domain embedded in the tetragonal domain. ....	44
Figure 16.	(a,b) Micrographs showing the secondary crack nucleation, ahead of the primary crack, and backward growth and bending toward the primary crack [71]. (c,d) Simulation results showing the evidence of a secondary crack and its interaction with the primary crack. (e,f) Simulation results showing both microstructure evolution and crack growth simultaneously. (MV1 = Monoclinic Variant 1, MV2 = Monoclinic Variant 2, T = Tetragonal). ....	48
Figure 17.	(a) Micrograph showing a primary crack growth and branching. One branch grows while the other branch stops growing [71]. (b,c) Simulation results showing the crack branching and closer of one branch. (d,e) Simulation results showing both microstructure evolution and crack growth simultaneously. (MV1 = Monoclinic Variant 1, MV2 = Monoclinic Variant 2, T = Tetragonal) ....	50
Figure 18.	(a,b) Micrographs showing interaction between a growing crack and a grain at two stages of crack growth (same location) [71]. (c,d) Simulation results showing the crack grain bridging. (e,f) Simulation results showing both microstructure evolution and crack growth simultaneously. (MV1 = Monoclinic Variant 1, MV2 = Monoclinic Variant 2, T = Tetragonal)....	51

Figure 19.	Polycrystalline configuration and lattice orientation variation in different grains. ....	52
Figure 20.	The co-evolution of MT and Mode I fracture in TPZ. ....	54
Figure 21.	The stress-strain curve for a faulted TPZ along with the co-evolution of crack and MT. ....	55
Figure 22.	Crack growth in untransformable TPZ results in an expected, the nearest route to the straight line, crack growth path (a). MT leads to an anomaly crack propagation route in transformable TPZ (b). (MV1 = Monoclinic Variant 1; MV2 = Monoclinic Variant 2, T = Tetragonal). ....	57
Figure 23.	The stress-strain curve, along with the crack propagation for transformable and untransformable TPZ. ....	58
Figure 24.	The crystal lattice orientation effects on the Mode I transgranular crack propagation in TPZ. The first column shows the lattice orientation angle ranges for each grain. The second column is the microstructure at the onset of crack growth. The last column is the crack growth path and amount for each microstructure (all are at the same time, 3500 s). (MV1 = Monoclinic Variant 1, MV2 = Monoclinic Variant 2, T = Tetragonal). ...	62
Figure 25.	The stress-strain curve for the Mode I transgranular fracture in tetragonal zirconia with different lattice orientation configuration. (LOR: lattice orientation; $R = GGBGG = 1$ ). ....	63
Figure 26.	The crystal lattice orientation effects on the Mode I intergranular crack propagation in TPZ. The first column shows the lattice orientation angle ranges of each microstructure. The second column is the microstructure at the onset of crack growth. The last column is the crack growth path and amount for each microstructure (all are at the same time, 3500 s). (MV1 = Monoclinic Variant 1, MV2 = Monoclinic Variant 2, T = Tetragonal). ...	66
Figure 27.	The stress-strain curve for the Mode I intergranular fracture in tetragonal zirconia with different lattice orientation configurations. (LOR: lattice orientation; $R = 0.2$ ). Microstructures with low angle grains show higher resistance to crack growth. See Figure 4 for angle interpretation. ....	67
Figure 28.	The effects of grain size on the crack propagation in TPZ. The first column is the crack propagation in each microstructure at $t = 3500$ s. The second column depicts the microstructure at the onset of the crack growth, $t = 600$ s. The last column is the crack growth pattern at $t = 3500$ s along with the corresponding microstructure. (MV1 = Monoclinic Variant 1, MV2 = Monoclinic Variant 2, T = Tetragonal). ....	70

Figure 29.	The stress-strain curve for the transgranular crack propagation in the TPZ with different average grain sizes ( $D_{\text{grain}}$ ). .....	71
Figure 30.	The fracture propagation path in TPZ with different fracture energy ratio ( $R$ ), the ratio of grain boundary fracture energy to the fracture energy inside the grains. The crack tends to depart from the grain boundaries when the ratio increases. ....	73
Figure 31.	Schematic representation of possible monoclinic variants derived from the correspondence $C$ , i.e., $c_i$ become $c_m$ [76]. .....	76
Figure 32.	The feasible monoclinic variants and their self-accommodating variants in $t \rightarrow m$ transformation [76]. .....	77
Figure 33.	The boundary conditions and geometry of a cube with an initial crack. ..	78
Figure 34.	PF model simulation result for martensitic transformation and crack propagation in a 3D single crystal zirconia (a) and comparison with the experiment (b) (c) [109]. .....	80
Figure 35.	Observation of the fragmented transformed plane in both simulation (a)-(b) and experiment, AFM (c) [109]. .....	81
Figure 36.	The concurrent evolution of $t \rightarrow m$ transformation and monoclinic variants reorientation with crack propagation in 3D single crystal zirconia in isosurface ( $\eta = 0.5$ ). (Vacant domain is tetragonal, yellow is monoclinic variant $ABC$ , cyan is monoclinic variant $ABC$ , and brown is crack) .....	83
Figure 37.	Microstructure and crack pattern in 3D single crystal zirconia with different lattice orientations. The first column shows the microstructure at $t = 200$ s, the second column shows the microstructure at $t = 2000$ s, and the last column shows the crack pattern at $t = 2000$ s. ....	87
Figure 38.	The temporal and spatial co-evolution of MT and crack for lattice orientation of 30 degrees in 3D single crystal zirconia. ....	89
Figure 39.	The Isosurface plots of the crack propagation in a single crystal zirconia for lattice orientation of 30 degrees around $b_r$ -axis. ....	91

## LIST OF ABBREVIATIONS

SMCs	Shape Memory Ceramics
3D	Three-Dimensional
MT	Martensitic Transformation
t→m	Tetragonal to Monoclinic
PF	Phase Field
2D	Two-Dimensional
TPZ	Tetragonal Polycrystalline Zirconia
MV1	Monoclinic Variant 1
MV2	Monoclinic Variant 2
T	Tetragonal
LOR	Lattice Orientation
AFM	Atomic Force Microscopy

## CHAPTER ONE: INTRODUCTION

SMCs offer many advantages compared to shape memory metallic alloys, including higher strength, higher operating temperature, better thermal stability, and superior oxidation/corrosion resistance [1]. Among the currently available SMCs, zirconia ( $ZrO_2$ )-based ceramics have received the most interest and attention because of their similarity to shape memory alloys in terms of mechanical-thermal actuation due to a reversible martensitic transformation (MT) mechanism [1]. Zirconia has a wide range of applications from biomedical to aerospace industries [2–6]. Most of these applications benefit from the superior fracture toughness of zirconia ceramics which originates from the stress-induced tetragonal to monoclinic ( $t \rightarrow m$ ) transformation [7,8]. The tensile stress field at the crack tip promotes the  $t \rightarrow m$  transformation, then the transformation strains change the stress state around the crack tip and lead to the toughening effect [9].

Garvie et al. [10] were the first who showed that it is possible to gain a significant increase in zirconia strength by making the tetragonal phase stable at room temperature. Tetragonal stabilization is feasible by adding oxide dopants or reducing the grain sizes. Both techniques reduce the tetragonal to monoclinic transformation temperature by decreasing the transformation driving force.

The stabilized zirconia is resistant to crack propagation, as the stress concentration at the crack tip excites the tetragonal to monoclinic ( $t \rightarrow m$ ) transformation. This transformation results in a considerable shear strain (0.16) and volume expansion (0.04) that will create a domain with large compressive stresses



leading to crack tip closure and preventing the crack growth, which enhances the toughening property of zirconia [7].

Despite the superior properties of zirconia, such as applicability for a wider range of temperatures and higher energy absorption, compared to the metallic shape memory materials [11], their widespread application is limited due to their brittleness and low fatigue life. While recent studies [11] have shown that increasing the fatigue life is possible by reducing the sample size, due to reducing the presences of some defects such as grain boundaries, we still lack the fundamental knowledge of how martensitic transformation (MT) and cracks interact concurrently.

Transformation toughening effect in zirconia ceramics has been the subject of several studies in past years [12–17]. Hannink et al. [7] and Kelly and Rose [8] have provided comprehensive reviews on this subject. Generally, there are two main approaches to assess the toughening effects of the phase transformation. The first approach computes the shielding effect of the phase transformation [12] by using the concept of linear elastic fracture mechanics. The second technique evaluates the fracture energy resulting from the phase transformation associated with a growing crack [13]. These models aimed to investigate the toughening effects of MT. However, they lacked the dynamics of phase transformation and its morphological dependence on boundary conditions, external loadings, and crystal orientation in their formulation. In this work, we use the phase field (PF) method to formulate a coupled model that concurrently captures both the physics of MT and crack propagations and their interactions.

Classically, the fracture of transformable brittle materials was primarily studied at macroscale [13,15,18,19]. Evans and Cannon [20] conducted a thorough study to unravel

the mechanisms underlying transformation toughening in brittle transformable materials. Based on their results, materials chemistry and microstructure are the dominant parameters impacting toughening mechanisms [21–23]. One drawback of these classical models is that they assumed the transformed zone *in priori*, and the dynamic and concurrent interaction of crack growth and MT is ignored. Besides, due to the nature of these macroscale models, they did not have the effects of defects, such as grain boundaries, on crack growth. The microstructure has a significant effect on the SMCs mechanical properties. For instance, grain size influences the effectiveness of MT and the development of microcracks [24]. The complexity of the fracture mechanics in SMCs is due to several mechanisms like MT, microcracks formation, crack deflection, and crack bridging [24]. Numerous circumstances, such as microstructure discontinuities (grain boundaries, second phases, inclusions, etc.), local stress states, or environments, would have profound influences on the crack paths, causing deflection and branching [24].

To address the limitations of the classical fracture mechanics models for SMCs and advance the fundamental understating of SMCs degradation, we have developed a mesoscale microstructure-informed model to study the dynamic interaction of concurrent crack growth and MT. For this purpose, we couple the Ginzburg-Landau equations of MT to the variational formulation of brittle fracture. These two models are also known as phase-field (PF) models of MT and crack growth.

In the last two decades, the PF method has become a successful technique for modeling a wide range of moving boundary problems, including solid state phase transformation [25–29], crack propagation [30–34], solidification [35–38], etc. PF modeling of MT, which is the mechanism of  $t \rightarrow m$  transformation, was primarily

developed by Khachaturyan, Wang, and Chen [27,39] based on the PF microelasticity theory of Khachaturyan and time dependent Ginzburg–Landau kinetic equations. Along with Khachaturyan and his co-workers, several other groups developed different forms of PF models for MT which have been comprehensively reviewed by Mamivand et al. [40]. Being applied to the wide range of different MTs, including cubic to tetragonal [41,42], hexagonal to orthorhombic [43–45], cubic to monoclinic [46], and tetragonal to monoclinic [8,47–49], the PF method has shown the capability of capturing the most important features of MTs.

Similar to MT, the PF method has attracted considerable attention in fracture mechanics [30,50–53] because of its relatively easier numerical implementation for fracture. In PF fracture, we utilize a scalar field, a so-called phase field, to represent the discrete cracks. Therefore, a crack in the PF method is not a discontinuity, and the transition from crack to the material is smooth. This diffuse interface modeling of crack enables the PF fracture to model the crack initiation, propagation, and branching behaviors in a robust manner in complex patterns. In addition, in the PF modeling, the crack propagation behavior can be combined with other physical phenomena such as phase transformation smoothly.

Generally, there are two types of PF models for crack growth, one developed in the physics community [33,54–58] and the other developed in the mechanics community [30,32,50,59–63]. These two communities have used completely different concepts and methods to formulate the crack growth in the PF framework. The physics community used the Ginzburg-Landau [64] formalism to model the crack propagation. However, the mechanics community used the variational formulation of classical Griffith's theory of

brittle fracture originally developed by Francfort and Marigo [65]. Ambati et al. [66] have holistically reviewed the PF modeling of crack growth and the differences between the two communities' models. In this work, we use the mechanics community models because they are tightly related to the well-established and understood Griffith's theory, widely applied by engineers. Due to the highly anisotropic nature of elasticity in tetragonal and monoclinic zirconia, we adopt an anisotropic elastic PF model for crack growth [67,68]. Zhao et al. [69] have studied the crack growth in zirconia by coupling the PF model of  $t \rightarrow m$  transformation originally developed by our group with the crack growth model of the physics community [33,54–58]. Zhao et al.'s work was limited in terms of predicting the crack propagation path. To overcome this limitation and explain the experimentally observed anomaly crack growth path in zirconia [20,70], we have constructed a new PF model for crack growth in zirconia based on our experimentally validated PF model of  $t \rightarrow m$  transformation and the mechanics communities diffuse interface framework of crack propagation. This work advances the crack propagation modeling in SMCs by capturing the concurrent dynamics of MT and crack propagation. We benchmark the model's predictability by validating the model's predictions against the experimental observations.

The dissertation outline is as follows. In chapter two, we first describe the PF governing equations of  $t \rightarrow m$  transformation and the variational formulation of crack growth for elastic anisotropic materials, followed by the process of combining MT and crack growth.

In chapter three, we present the coupled PF model predictions for the single crystal model. We validate the results by comparing them to the experimental results.

Temporal and spatial evolution of concurrent crack propagation and phase transformation is provided, and the effects of lattice orientation on the fracture toughening and crack growth routes are analyzed. Subsequently, we present the conclusions in the final section.

In chapter four, the model is parametrized for the polycrystalline zirconia and the result is provided. We study the interaction of MT and crack growth with grain boundaries, this is particularly important because several studies noted that pure zirconia has an intergranular fracture mode while yttrium stabilized zirconia and alumina-zirconia have a transgranular fracture [24,71]. In this chapter, we explain the algorithm that we used to generate two-dimensional (2D) polycrystalline geometry and mesh. The result validated by comparing with the experimental observation. Additionally, the effect of grain size on the fracture toughening and crack growth path is provided.

In chapter five, the developed phase field model is extended to a three dimensional model. Twelve different order parameters have assigned to all possible monoclinic variants. We provide a brief description of the crystallography of  $t \rightarrow m$  transformation in zirconia. Then, we validate the model by comparing the results with the experimental observations. We elaborate the temporal and spatial evolution of simultaneous fracture and MT in 3D and study the influence of lattice orientation on the fracture, crack pattern, and toughening in 3D zirconia single crystal. Finally, the key findings are summarized.

This dissertation leads to the following peer-reviewed papers;

- 1) Ehsan Moshkelgosha, Mahmood Mamivand, (2019, November). "Anisotropic Phase-Field Modeling of Crack Growth in Shape Memory Ceramics: Application to Zirconia". In ASME International Mechanical Engineering Congress and

Exposition (Vol. 59490, p. V012T10A064). American Society of Mechanical Engineers. doi:10.1115/IMECE2019-11695.

- 2) Ehsan Moshkelgosha, Mahmood Mamivand, " Phase field modeling of crack propagation in shape memory ceramics – Application to zirconia", Computational Materials Science, Volume 174, (2020), 109509, ISSN 0927-0256, <https://doi.org/10.1016/j.commatsci.2019.109509>.
- 3) Ehsan Moshkelgosha, M. Mamivand, Concurrent modeling of martensitic transformation and crack growth in polycrystalline shape memory ceramics, Engineering Fracture Mechanics, (2020) 107403. doi:10.1016/j.engfracmech.2020.107403.
- 4) Ehsan Moshkelgosha, Mahmood Mamivand, " Three-dimensional Phase Field Modeling of Fracture in Shape Memory Ceramics" Submitted to International Journal of Mechanical Sciences, March 2021
- 5) Lupercio, AE, Moshkelgosha, E, Winters, RC, et al. " Ball-on-ring test validation for equibiaxial flexural strength testing of engineered ceramics " International Journal of Ceramic Engineering and Science, 2021; 00: 1– 12. [72] <https://doi.org/10.1002/ces2.10085>

## CHAPTER TWO: METHODS

In this chapter, we derive the governing equations of MT in the context of the PF framework. Then, we will provide the details of the variational model of crack propagation in elastically anisotropic materials, and finally, we will couple these two models to investigate the effect of MT on crack propagation and vice versa.

The result provided in this chapter is published as a research paper [73] in the ASME International Mechanical Engineering Congress and Exposition (Volume 12, November 2019, IMECE2019-11695, <https://doi.org/10.1115/IMECE2019-11695>)

### **Phase Field Method**

The phase-field method has become an important and extremely versatile technique for simulating microstructure evolution at the mesoscale. Thanks to the diffuse-interface approach, it allows us to study the evolution of arbitrary complex grain morphologies without any presumption on their shape or mutual distribution. It is also straightforward to account for different thermodynamic driving forces for microstructure evolution, such as bulk and interfacial energy, elastic energy and electric or magnetic energy, and the effect of different transport processes, such as mass diffusion, heat conduction and convection.

Most materials are heterogeneous on the mesoscale. Their microstructure consists of grains or domains, which differ in structure, orientation and chemical composition. The physical and mechanical properties on the macroscopic scale highly depend on the shape, size and mutual distribution of the grains or domains. It is, therefore, extremely important

to gain insight in the mechanisms of microstructure formation and evolution. However, extensive theoretical and experimental research are hereto required, as microstructure evolution involves a large diversity of often complicated processes. Moreover, a microstructure is inherently a thermodynamic unstable structure that evolves in time. Within this domain, the phase-field method has become a powerful tool for simulating the microstructural evolution in a wide variety of material processes, such as solidification, solid-state phase transformations, precipitate growth and coarsening, martensitic transformations and grain growth.

The microstructures considered in phase-field simulations typically consist of a number of grains. The shape and mutual distribution of the grains is represented by functions that are continuous in space and time, the phase-field variables. Within the grains, the phase-field variables have nearly constant values, which are related to the structure, orientation and composition of the grains. The interface between two grains is defined as a narrow region where the phase-field variables gradually vary between their values in the neighboring grains. This modeling approach is called a diffuse-interface description. The evolution of the shape of the grains, or in other words the position of the interfaces, as a function of time, is implicitly given by the evolution of the phase-field variables.

An important advantage of the phase-field method is that, thanks to the diffuse-interface description, there is no need to track the interfaces (to follow explicitly the position of the interfaces by means of mathematical equations) during microstructural evolution. Therefore, the evolution of complex grain morphologies, typically observed in technical alloys, can be predicted without making any a priori assumption on the shape of



the grains. The temporal evolution of the phase field variables is described by a set of partial differential equations, which are solved numerically. Different driving forces for microstructural evolution, such as a reduction in bulk energy, interfacial energy and elastic energy, can be considered. The phase-field method has a phenomenological character: the equations for the evolution of the phase-field variables are derived based on general thermodynamic and kinetic principles; however, they do not explicitly deal with the behavior of the individual atoms. As a consequence, material specific properties must be introduced into the model through phenomenological parameters that are determined based on experimental and theoretical information. Nowadays, the phase-field technique is very popular for simulating processes at the mesoscale level. The range of applicability is growing quickly, amongst other reasons because of increasing computer power.

There is a wide variety of phase-field models, but common to all is that they are based on a diffuse-interface description. The interfaces between domains are identified by a continuous variation of the properties within a narrow region, Figure 1.a, which is different from the more conventional approaches for microstructure modeling.

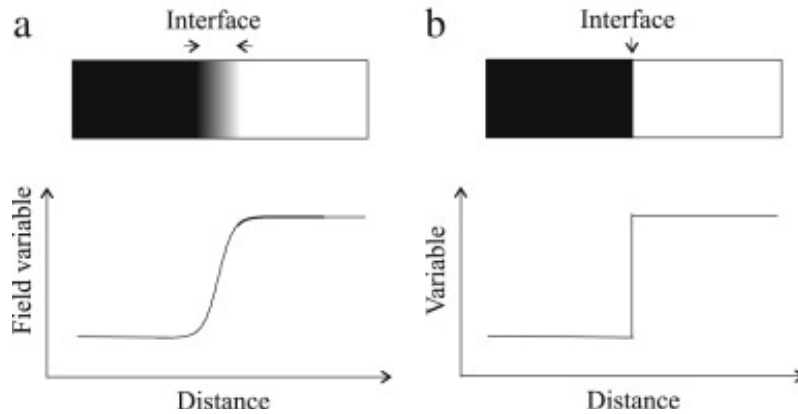


**Figure 1. (a) Diffuse interface: properties evolve continuously between their equilibrium values in the neighboring grains. (b) Sharp interface: properties are discontinuous at the interface.[74]**

In conventional modeling techniques for phase transformations and microstructural evolution, the interfaces between different domains are considered to be infinitely sharp, Figure 1.b, and a multi-domain structure is described by the position of the interfacial boundaries. For each domain, a set of differential equations is solved along with flux conditions and constitutive laws at the interfaces. In the diffuse-interface approach, the microstructure is represented by means of a set of phase-field variables that are continuous functions of space and time. Within the domains, the phase-field variables have the same values as in the sharp interface model (see Figure 1.a). However, the transition between these values at interfaces is continuous. The position of the interfaces is thus implicitly given by a contour of constant values of the phase-field variables and the kinetic equations for microstructural evolution are defined over the whole system. Using a diffuse-interface description, it is possible to predict the evolution of complex grain morphologies as well as a transition in morphology.

### PF Modeling of the T→M Transformation

In this dissertation, we build on the PF model of t→m transformation in zirconia, originally developed by Mamivand et al.[23,49,75,76]. We briefly describe the PF model of t→m transformation in zirconia and refer the interested readers to the original papers for more details [49]. In the PF method, a multidomain microstructure can be described by a set of PF variables, also known as order parameters. In the case of the t→m transformation, PF variables are the possible variants of the monoclinic phase. Variants are all possible monoclinic unit cells which are crystallographically self-similar and obey colored symmetry point group operations in a dichromatic complex between the two phases [75]. This is simplistically schematized in Figure 2.

We use the non-conserved order parameters  $\eta_p(\vec{r}, t)$  to represent the content of the  $p^{th}$  monoclinic variant, where  $r$  is the position vector of the material point and  $t$  refers to time. During the MT, the value of  $\eta_p$  varies from 0 to 1. When  $\eta_p = 1$ , the monoclinic phase exists, and when  $\eta_p = 0$ , it is either one of the other monoclinic variants or the parent tetragonal phase.

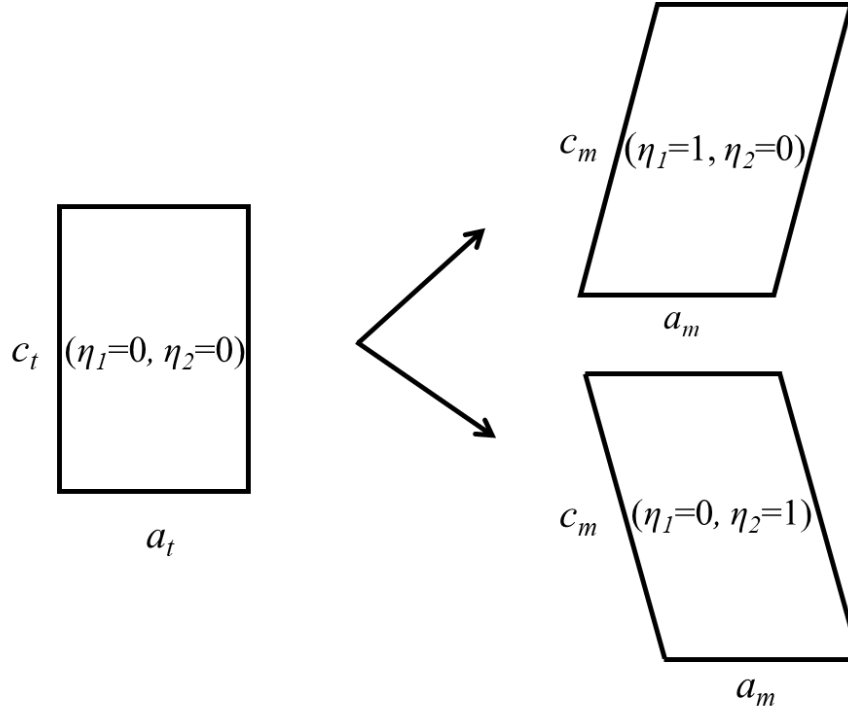


**Figure 2. Schematic illustration of possible variants of the monoclinic phase during  $t \rightarrow m$  transformation in 2D [75].**

The Ginzburg Landau equation has a phenomenological character and relates the rate of order parameter to the variational derivative of total free energy to the order parameter [77]:

$$\frac{\partial \eta_p(\vec{r}, t)}{\partial t} = -L \frac{\delta F}{\delta \eta_p(\vec{r}, t)} + \zeta_p(\vec{r}, t) \quad p = 1, \dots, n, \quad (1)$$

where  $\eta_p$  represent the  $p^{th}$  variant of monoclinic,  $L$  is the kinetic coefficient,  $F$  is the total free energy of the system,  $\frac{\delta F}{\delta \eta_p(\vec{r}, t)}$  is the thermodynamic driving force for the spatial and temporal evolution of  $\eta_p$  and  $\zeta_p(\vec{r}, t)$  is the Langevin noise describing the thermal fluctuation [27,64].

For the MT process, the total free energy can be written as the summation of chemical free energy and elastic strain energy

$$F = F_{ch} + F_{el}. \quad (2)$$

### Chemical Free Energy

Chemical free energy is the driving force of MT and primarily originates from the difference of Gibbs free energy between tetragonal and monoclinic phases. Considering the interfacial energies between the co-existing phases we can write the total chemical free energy as [27]:

$$F_{ch} = \int_V \left[ f(\eta_1, \eta_2, \dots, \eta_n) + \frac{1}{2} \sum_{p=1}^n \beta_{ij}(p) \nabla_i \eta_p \nabla_j \eta_p \right] dV \quad n = 1, \dots, p, \quad (3)$$

where  $\beta_{ij}(p)$  is the positively defined gradient energy coefficient tensor and  $\nabla$  is the gradient operator. The bulk chemical free energy  $f(\eta_1, \eta_2, \dots, \eta_n)$  for improper transformation can be expressed as a sixth-order Landau polynomial

$$f(\eta_1, \eta_2, \dots, \eta_n) = \Delta G \left[ \frac{a}{2} (\eta_1^2 + \eta_2^2 + \dots + \eta_n^2) - \frac{b}{4} (\eta_1^4 + \eta_2^4 + \dots + \eta_n^4) + \frac{c}{6} (\eta_1^2 + \eta_2^2 + \dots + \eta_n^2)^3 \right], \quad (4)$$

where  $\Delta G$  is the chemical driving force which stands for the difference between the specific free energy of the parent phase and the product phase.  $a$ ,  $b$  and  $c$  are the expansion coefficients of the Landau polynomial at a fixed temperature.

We assume that the positive gradient energy coefficient is isotropic ( $\beta_{ij} = \beta \delta_{ij}$ ); therefore the chemical free energy can be simplified as:

$$F_{ch} = \int_V \left[ f(\eta_1, \eta_2, \dots, \eta_n) + \frac{1}{2} \sum_{p=1}^n \beta (\nabla_i \eta_p)^2 \right] dV. \quad (5)$$

### Elastic Strain Energy

An important part of the free energy in MT is the strain energy which stems from the lattice mismatch between the parent, here tetragonal, and product phases, here monoclinic. Unlike chemical free energy which drives the MT, strain energy opposes the phase transformation. Following Khachaturyan [78] the strain energy can be expressed as a function of the transformation-induced stress free strain  $\varepsilon_{ij}^0(\vec{r})$ . Stress free strain characterize the degree of lattice mismatch between the parent and product phases and since we are using the diffusive interface description, we need to express the stress free strain in terms of order parameters; therefore, the local stress free strain is related to order parameters through [27]:

$$\varepsilon_{ij}^0(\vec{r}) = \sum_{p=1}^n \varepsilon_{ij}^{00}(p) \eta_p^2(\vec{r}), \quad (6)$$

where  $\varepsilon_{ij}^{00}(p)$  is the transformation strain of  $p^{th}$  variant. The elastic strain energy of a system is given by:

$$F_{el} = \frac{1}{2} \int_V \sigma_{ij} \varepsilon_{ij}^{el} dV = \frac{1}{2} \int_V C_{ijkl} \varepsilon_{kl}^{el} \varepsilon_{ij}^{el} dV, \quad (7)$$

where the elastic strain  $\varepsilon_{ij}^{el}(\vec{r})$  is the difference between the total strain,  $\varepsilon_{ij}^{tot}(\vec{r})$ , and the stress free strain,  $\varepsilon_{ij}^0(\vec{r})$ :

$$\varepsilon_{ij}^{el}(\vec{r}) = \varepsilon_{ij}^{tot}(\vec{r}) - \varepsilon_{ij}^0(\vec{r}) = \varepsilon_{ij}^{tot}(\vec{r}) - \sum_p \varepsilon_{ij}^{00}(p) \eta_p^2(\vec{r}) = \frac{1}{2} \left( \frac{\partial u_i(\vec{r})}{\partial r_j} + \frac{\partial u_j(\vec{r})}{\partial r_i} \right) - \sum_p \varepsilon_{ij}^{00}(p) \eta_p^2(\vec{r}). \quad (8)$$

We consider inhomogeneous elasticity and define a smooth transition from t→m elastic constants through the following equation,

$$C_{ijkl} = P(\sum_{i=1}^n \eta_i)C^M + (1 - P(\sum_{i=1}^n \eta_i))C^T, \quad (9)$$

where  $C^M$  and  $C^T$  are monoclinic and tetragonal elastic constants respectively,  $n$  is the number of order parameters and

$$P(\eta) = \eta^3(6\eta^2 - 15\eta + 10). \quad (10)$$

Thus the total free energy for the phase transformation is:

$$F = \int_V \left[ f(\eta_1, \eta_2, \dots, \eta_n) + \frac{1}{2} \sum_{p=1}^n \beta (\Delta\eta_p)^2 \right] dV + \frac{1}{2} \int_V C_{ijkl} \varepsilon_{ij}^{el} \varepsilon_{kl}^{el} dV. \quad (11)$$

### The Variational Formulation for PF Modeling of Crack Growth

Before we describe the details of the PF modeling of crack propagation, it is worthwhile to briefly review the standard computational techniques in fracture mechanics. Generally, researchers categorize the fracture mechanics numerical models into two approach categories: discrete and continuous. The discrete approach simulates fractures as discontinuities. From a numerical point of view, how computational modelers propagate cracks depends on model use; they either break elements with finite element models or split nodes and reconnect springs when using spring network models [79]. Two drawbacks are that the discretization must change topology because of fracture growth, and that fracture propagation is restricted to follow mesh lines. Modelers can overcome these disadvantages either by using remeshing techniques [80] or by using advanced approaches, such as cohesive zone modeling [81] or the enriching displacement method [82].

On the other hand, continuous approaches, e.g., peridynamics, gradient damage, or phase-field models, consider the intact and fractured areas as a whole, without the need to introduce discontinuities. Among continuous approaches, phase-field modeling has recently emerged as a competitive method to describe fracture phenomena. In general, the phase-field approach, to model systems with sharp interfaces, consists of incorporating a continuous field variable—the so-called “order parameter”—which differentiates between multiple physical phases within a given system through a smooth transition. In the context of fracture, such order parameter (the crack phase field) describes the smooth transition between the fully broken and intact material phases, thus approximating the sharp crack discontinuity. The evolution of the crack phase-field as a result of external loading conditions models the fracture process. What makes the phase-field approach particularly attractive is its ability to elegantly simulate complicated fracture processes, including crack initiation, propagation, merging, and branching, in general situations and for three-dimensional (3D) geometries, without the need for additional ad-hoc criteria.

The phase-field model tracks propagating cracks automatically given the evolution of the smooth crack field on a fixed mesh. This leads to a significant advantage over discrete fracture description methods. Therefore, it is the perfect candidate to enable a seamless transition between describing continuum damage and discrete crack propagation phases. The main advantages of the phase-field approach are that the method: (1) conducts all calculations on the initial undeformed topology; (2) has the ability to simulate complex fracturing processes, such as branching, joining, propagation, or nucleation, without the need for additional criteria; and (3) handles heterogeneous media without any additional rule.



For variational modeling of crack growth, we have primarily used the models developed in Ref. [30,51,60,83,84] and describe it briefly in below.

### Theory of Brittle Fracture

To describe the PF formulation of crack propagation, consider a material body  $\Omega \subset \mathbb{R}^d$  ( $d \in \{1, 2, 3\}$ ) with a boundary of  $\partial\Omega$  which contains an internal discontinuity boundary  $\Gamma$ , e.g. crack. Similar to the PF model of MT, we define the displacement of the body  $\Omega$  at time  $t$  as  $\vec{u}(\vec{r}, t)$  in which  $\vec{r}$  is the position vector and  $t$  is time. The time-dependent Dirichlet boundary conditions fulfill the displacement field,  $u_i(\vec{r}, t) = g_i(\vec{r}, t)$ , on  $\partial\Omega_{gi} \in \Omega$ , and also the time-dependent Neumann conditions apply on the  $\partial\Omega_{hi} \in \Omega$ . We also consider a body force  $\vec{b}(\vec{r}, t)$  acting on the body  $\Omega$  and a traction  $f(r, t)$  acting on the boundary  $\partial\Omega_{hi}$ .

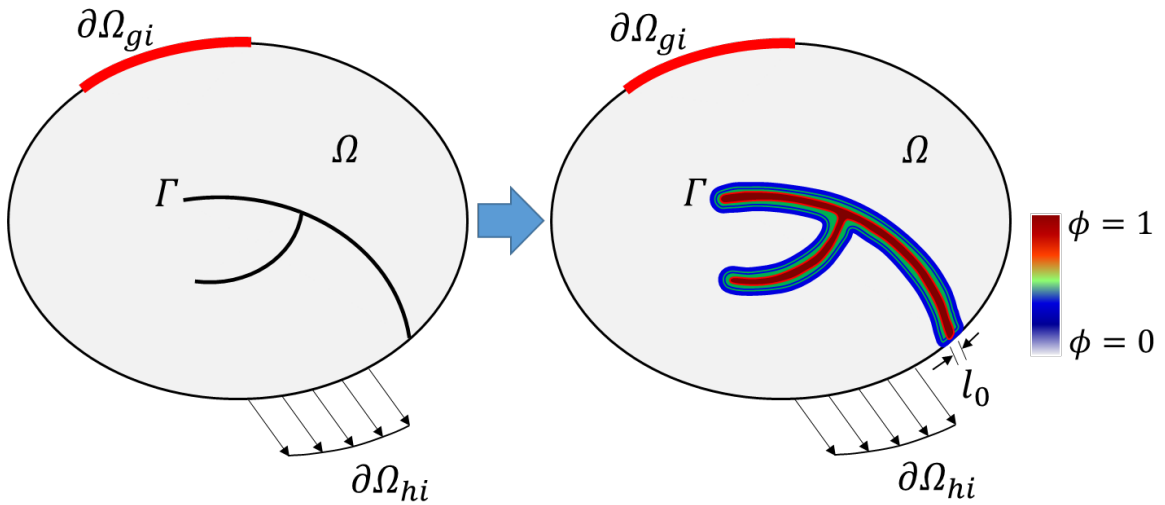


**Figure 3.** Phase field approximation of the crack surface. In PF modeling of crack growth, we use the PF variable  $\phi(r, t) \in [0, 1]$  as the order parameter, with  $\phi = 1$  shows the crack and  $\phi = 0$  indicates that the body is uncracked.

The PF modeling of crack propagation is fundamentally based on the pioneering work of Francfort and Marigo's [65] who developed the variational formulation of the

Griffith's theory. Their model declares that the minimum energy needed for producing a cracked surface per unit area is equal to the critical fracture energy density  $G_c$ , which is also commonly referred as the critical energy release rate [85]. For materials which do not experience ad hoc physics, such as MT, the total potential energy  $\Psi_{pot}(u, \Gamma)$  is consist of the elastic energy  $\psi_\varepsilon(\varepsilon)$ , fracture energy, and energy due to the external forces:

$$\Psi_{pot}(u, \Gamma) = \int_{\Omega} \psi_\varepsilon(\varepsilon) d\Omega + \int_{\Gamma} G_c dS - \int_{\Omega} b \cdot u d\Omega - \int_{\partial\Omega_{h_i}} f \cdot u dS, \quad (12)$$

where  $\varepsilon = \varepsilon(\vec{u})$  is the linear strain tensor defined by,

$$\varepsilon_{ij} = \frac{1}{2} \left( \frac{\partial u_i}{\partial r_j} + \frac{\partial u_j}{\partial r_i} \right). \quad (13)$$

### Phase Field Approximation for Fracture Energy

Similar to the PF modeling of MT, we need a PF variable to describe the cracked and intact domains. We use the PF variable  $\phi(r, t) \in [0, 1]$ , with  $\phi = 1$  shows the crack and  $\phi = 0$  indicates that the body is uncracked (see Figure 3). Based on this diffusive crack topology, we can express the crack surface density per unit volume of the solid body by [30],

$$\gamma(\phi, \nabla\phi) = \left[ \frac{\phi^2}{2l_0} + \frac{l_0}{2} \frac{\partial\phi}{\partial r_i} \frac{\partial\phi}{\partial r_i} \right] d\Omega, \quad (14)$$

where  $l_0$  adjusts the passing zone of the PF variable from 0 to 1.  $l_0$  is called the length scale parameter that represents the shape of a crack. Increasing  $l_0$  would widen the crack region and vice versa. By integration of Eq. 14 over the crack domain, the fracture energy could be expressed by,

$$\int_{\Gamma} G_c dS = \int_{\Omega} G_c \left[ \frac{\phi^2}{2l_0} + \frac{l_0}{2} \frac{\partial \phi}{\partial r_i} \frac{\partial \phi}{\partial r_i} \right] d\Omega. \quad (15)$$

To avoid crack growth in compression, a unilateral contact formulation is utilized. This goal can be achieved by implementing two different methods [86]; 1) by dividing the strain tensor into positive and negative strain parts (see [30,87]), or; 2) by decomposing the strain tensor into spherical and deviatoric strain components (see [62]). It is hard to implement the first technique in an application for anisotropic materials because there is no general formulation for the elastic tensor. Therefore we use the second technique in the present work following Ref. [62]. We decompose the elastic strain into deviatoric  $\varepsilon_{dev}$  and spherical  $\varepsilon_{sph}$  parts. Then, it is considered that the crack is produced by expansion only (positive spherical part) and shear: [86]

$$\psi_{\varepsilon}(\varepsilon, \phi) = \begin{cases} \frac{1}{2} g(\phi) [\varepsilon : C^0 : \varepsilon] & \text{if } tr(\varepsilon) \geq 0 \\ \frac{1}{2} [\varepsilon_{sph} : C^0 : \varepsilon_{sph}] + g(\phi) [\varepsilon_{dev} : C^0 : \varepsilon_{dev}] & \text{if } tr(\varepsilon) < 0 \end{cases}, \quad (16)$$

where  $tr(\varepsilon)$  is the trace operator for a second-order strain tensor and  $C^0$  expresses the initial elastic tensor of the material. It is presumed that the degradation function  $g(\phi)$  in Eq. 16 has the following simple form:

$$g(\phi) = (1 - k)(1 - \phi)^2 + k. \quad (17)$$

The function  $g(\phi)$  is defined in a way that  $g'(\phi = 1) = 0$  to ensure that the strain energy density function would be a finite value as the domain is locally damaged and  $g(0) = 1$  to guarantee that the material is uncracked.  $g(\phi = 1) = 0$  is the limit for a fully damaged material. The quadratic function  $(1 - \phi)^2$  is defined to make sure about

the presence of a regular solution [68]. Further possibilities like quartic function or cubic functions have been presented in [55,88]. The insignificant value  $k \ll 1$  is often implemented to keep the well-posedness of the solution for partially fractured parts of the field [86].

Now we can define elastic tensor as the following format:

$$C(\phi) = g(\phi)C^0 + k_0 \mathbf{1} \otimes \mathbf{1} [1 - g(\phi)] \text{sign}^-(\text{tr}(\varepsilon)), \quad (18)$$

where the sign function  $\text{sign}^-(x) = 1$  if  $x < 0$  and  $\text{sign}^-(x) = 0$  if  $x \geq 0$ . The strain energy can be rewritten as:

$$\psi_\varepsilon(\varepsilon, \phi) = \frac{1}{2} [\varepsilon : C(\phi) : \varepsilon]. \quad (19)$$

### **Combining the Variational Formulation of Crack Growth and the T→M Transformation**

In this section, we combine the variational formulation of crack propagation with the PF formulation of t→m transformation to develop a model that tracks the co-evolution of the MT and crack propagation. We construct the total free energy functional by summing up the Eq. 11 and Eq. 12.

$$\begin{aligned} \Psi_{pot}(u, \Gamma) = & \int_{\Omega} \psi_\varepsilon(\varepsilon) d\Omega + \int_{\Gamma} G_c dS + \int_{\Omega} f(\eta_1, \eta_2, \dots, \eta_n) + \\ & \frac{1}{2} \sum_{p=1}^n \beta_{ij}(p) \nabla_i \eta_p \nabla_j \eta_p d\Omega - \int_{\Omega} b \cdot u d\Omega - \int_{\partial\Omega h_t} f \cdot u dS. \end{aligned} \quad (20)$$

By replacing  $\psi_\varepsilon(\varepsilon)$  from Eq. 19 and  $G_c$  from Eq. 15 and  $f(\eta_1, \eta_2, \dots, \eta_n)$  from Eq. 4 we have:

$$\begin{aligned}
\Psi_{pot}(u, \Gamma) = & \int_{\Omega} \frac{1}{2} [\varepsilon: C_{ijkl}(\phi): \varepsilon] d\Omega + \int_{\Omega} G_c \left[ \frac{\phi^2}{2l_0} + \frac{l_0}{2} \frac{\partial \phi}{\partial r_i} \frac{\partial \phi}{\partial r_i} \right] d\Omega + \\
& \int_{\Omega} \Delta G \left[ \frac{a}{2} (\eta_1^2 + \eta_2^2 + \dots + \eta_n^2) - \frac{b}{4} (\eta_1^4 + \eta_2^4 + \dots + \eta_n^4) + \frac{c}{6} (\eta_1^2 + \eta_2^2 + \dots + \right. \\
& \left. \eta_n^2)^3 \right] d\Omega + \frac{1}{2} \sum_{p=1}^n \beta_{ij}(p) \nabla_i \eta_p \nabla_j \eta_p d\Omega - \int_{\Omega} b \cdot u d\Omega - \int_{\partial\Omega_{hi}} f \cdot u dS.
\end{aligned} \tag{21}$$

The variation of the functional  $\Psi_{pot}$  can be derived and its first variation should be zero, which leads to the following governing equations:

$$2(1-k)(1-\phi)[\varepsilon: C_h: \varepsilon] - 2\Psi_c(\phi - l_0^2 \nabla^2 \phi) = 0, \tag{22}$$

$$\text{where } \Psi_c = \frac{G_c}{2l_0} \text{ and } C_h = \frac{1}{2} (C_{ijkl} - k_0 \mathbf{1} \otimes \mathbf{1} \text{sign}^-(\text{tr}(\varepsilon))).$$

To consider loading and unloading histories, Miehe et al. [30] introduced the strain history functional, which is defined in by:

$$\mathcal{H}(r, t) = \max_{\tau \in [0, t]} \{ (1-k)[\varepsilon: C_h: \varepsilon] \}. \tag{23}$$

By replacing Eq. 23 in the Eq. 22, we have:

$$(1-\phi)\mathcal{H} - \Psi_c(\phi - l_0^2 \nabla^2 \phi) = 0. \tag{24}$$

Finally, by some mathematical operation we obtain:

$$\left(1 + \frac{\mathcal{H}}{\Psi_c}\right) \phi - l_0^2 \nabla^2 \phi = \frac{\mathcal{H}}{\Psi_c}. \tag{25}$$

The Ginzburg-Landau equation for t→m transformation, Eq. 1, by considering the given energy functional of the coupled PF model is:

$$\frac{\partial \eta_p(\vec{r}, t)}{\partial t} = -L \left( -\beta \nabla^2 \eta_p(\vec{r}, t) + \frac{\partial f}{\partial \eta_p(\vec{r}, t)} + \frac{\delta F_{el}}{\delta \eta_p(\vec{r}, t)} \right) + \zeta_p(\vec{r}, t) \quad p = 1, \dots, n \tag{26}$$

where  $f$  was defined in Eq. 4, and

$$\begin{aligned}
\frac{\delta F_{el}}{\delta \eta_p(\vec{r}, t)} = & -\frac{1}{2} C_{ijkl}(\phi) \varepsilon_{kl}^{00}(p) \eta_p(\vec{r}, t) \left( u_{i,j}(\vec{r}) + u_{j,i}(\vec{r}) \right) + \\
& C_{ijkl}(\phi) \varepsilon_{kl}^{00}(p) \eta_p(\vec{r}, t) \sum_{z=1}^n \varepsilon_{ij}^{00}(z) \eta_z^2(\vec{r}, t) - \frac{1}{2} C_{ijkl}(\phi) \varepsilon_{ij}^{00}(p) \eta_p(\vec{r}, t) (u_{k,l}(\vec{r}) + \\
& u_{l,k}(\vec{r})) + C_{ijkl}(\phi) \varepsilon_{ij}^{00}(p) \eta_p(\vec{r}, t) \sum_{z=1}^n \varepsilon_{kl}^{00}(z) \eta_z^2(\vec{r}, t)
\end{aligned} \quad (27)$$

L in Eq. 26, which is called the mobility parameter, is considered to incrementally rising from 0 to a constant  $L_0$  while  $\phi$  changes from 0 to 0.8 and then stays a constant until  $\phi$  becomes 1.

Eventually, we have to use the combination of Eqs. 25 and 26 along with the following mechanical equilibrium equations to find the displacement of the domain.

$$\frac{\partial \sigma_{ij}}{\partial r_j} = 0 \Rightarrow C_{ijkl}(\phi) \left[ \frac{1}{2} (u_{k,lj}(\vec{r}) + u_{l,kj}(\vec{r})) - \sum_p \varepsilon_{kl}^{00}(p) \frac{\partial}{\partial r_j} (\eta_p^2(\vec{r})) \right] = 0 \quad (28)$$

Eqs. 25, 26, and 28 are solved in the finite element package COMSOL Multiphysics considering the boundary and load conditions which are discussed in the next chapters.

## CHAPTER THREE: SINGLE CRYSTAL MODEL

In this chapter, we parametrize the developed model to the single crystal zirconia and provide the result. This study reveals the effect of microstructure evolution and phase transformation on the crack growth of shape memory ceramics.

The result provided in this chapter is published as a research paper [89] in the Computational Materials Science Journal (Volume 174, March 2020, 109509, <https://doi.org/10.1016/j.commatsci.2019.109509>)

### **Result**

To study the crack growth in a single crystal tetragonal zirconia, we consider an edge cracked square plate with domain dimensions of  $2 \mu\text{m} \times 2 \mu\text{m}$  with plane strain assumption, see Figure 4. We note that in 2D there are two possible variants for monoclinic, Figure 2, while the number of possible monoclinic variants in 3D is 12. However, not all 12 monoclinic variants have an equal chance for formation. Experimental observations and theoretical calculations [90–92] have shown that the transformation of the a-axis and c-axis in tetragonal to the a-axis and c-axis in monoclinic, respectively, is the most dominant transformation path, due to the small strain energy associated with it. Therefore, in the 2D model in this chapter, we have studied the plane which includes  $a_t$  (a-axis in tetragonal) and  $c_t$  (c-axis in tetragonal). Therefore, the 2D model is able to predict the experimentally observed morphologies during  $t \rightarrow m$  as was discussed in more details in Ref. [49].

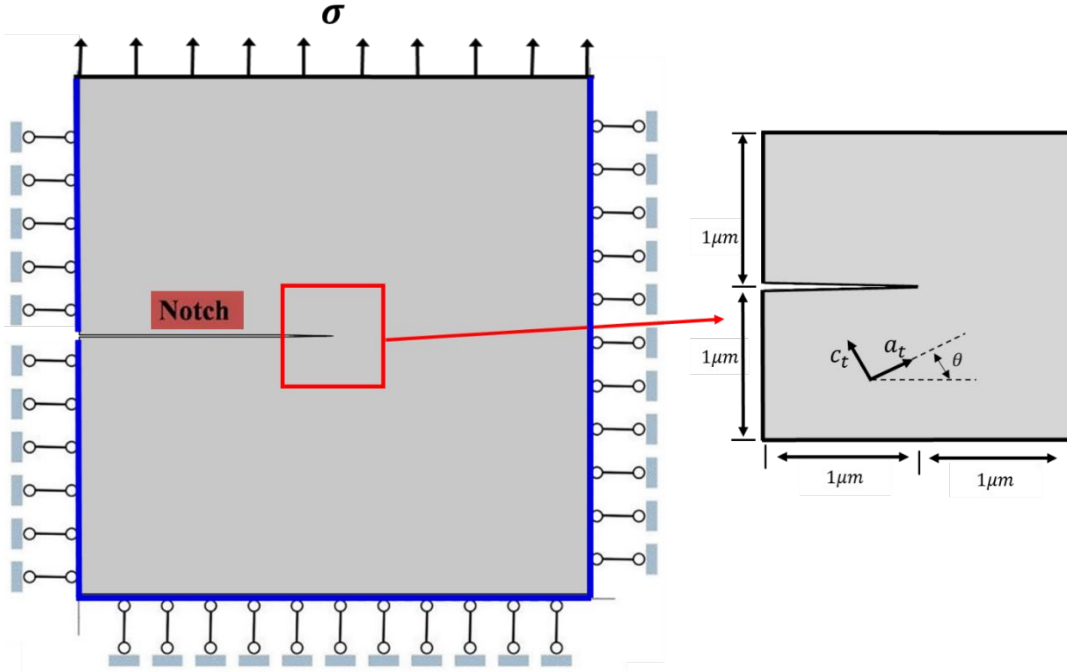


**Figure 4.** The geometry and boundary conditions of a single-edge-notched square plate subjected to tension loading.

In Figure 4, a time dependent tensile load is applied to the upper boundary of the model. We apply a constant load increment rate of  $\Delta\sigma = 1 \text{ MPa/s}$  to ensure the convergence.

We consider the Langevin noise in Eq. 1 to be zero and impose a randomly distributed initial condition for the phase transformation order parameters. The initial condition for displacement is zero in the whole domain, and boundary conditions for the  $i^{\text{th}}$  order parameter are periodic and

$$n \cdot \nabla \eta_i = 0, \quad i = 1, \dots, p. \quad (29)$$

The input parameters of the model are listed in Table 1, Table 2 and Table 3.



**Table 1. Elastic constants for monoclinic zirconia (GPa) [49].**

$C_{11}$	$C_{22}$	$C_{33}$	$C_{44}$	$C_{55}$	$C_{66}$
361	408	258	100	81	126

$C_{12}$	$C_{13}$	$C_{16}$	$C_{23}$	$C_{26}$	$C_{36}$	$C_{45}$
142	55	-21	196	31	-18	-23

**Table 2. Elastic constants for tetragonal zirconia (GPa) [49].**

$C_{11}$	$C_{33}$	$C_{44}$	$C_{66}$	$C_{12}$	$C_{13}$
327	264	59	64	100	62

**Table 3. Numerical values used for calculation.**

Temperature (K) [49]	1170
Chemical driving force, $(J.mol^{-1})$ [49]	800 ( $36.8 \times 10^6 J.m^{-3}$ )
Gradient energy coefficient, $\beta (J.m^{-1})$ [49]	$1 \times 10^{-8}$
Energy density coefficient, $a$ [49]	0.14
Energy density coefficient, $b$ [49]	12.42
Energy density coefficient, $c$ [49]	12.28
Kinetic coefficient, $L (m^3.J^{-1}.s^{-1})$	$2 \times 10^{-9}$
Critical energy release rate, $G_c (J.m^{-2})$ [69]	4.33
Crack elasticity modification parameter, $k$	$1 \times 10^{-9}$
The length parameter, $l_0 (nm)$	20
t→m transformation strains, $\varepsilon^{00}$ [49]	$\varepsilon^{00}(1) = \begin{bmatrix} 0.0049 & 0.0761 \\ 0.0761 & 0.0180 \end{bmatrix}$ $\varepsilon^{00}(2) = \begin{bmatrix} 0.0049 & -0.0761 \\ -0.0761 & 0.0180 \end{bmatrix}$

### Model Verification

We verified our model by simulating the crack propagation path of an edge crack in an elastic anisotropic single crystal tetragonal zirconia under the mode I loading. Since the lattice orientation was not identified in the experiment, we picked a lattice orientation angle,  $\theta$ , of  $150^\circ$ . This choice reproduced similar martensitic laths as the experimental observations. PF simulation results show that the phase transformation starts from the crack tip which is consistent with the experimental observations [20,70] and previous models [23,69].  $t \rightarrow m$  initiation at the crack tip is due to high local stresses at the crack tip which provides enough strain energy to trigger  $t \rightarrow m$  transformation. While the crack is expected to propagate in a straight line because of the Mode I loading, the PF simulation shows that crack would deviate from the straight path and deflect upward. This anomaly crack growth path was also observed in experimental studies of crack growth in  $\text{ZrO}_2 - 18 \text{ mol } \% \text{ CeO}$  [20], Figure 5.

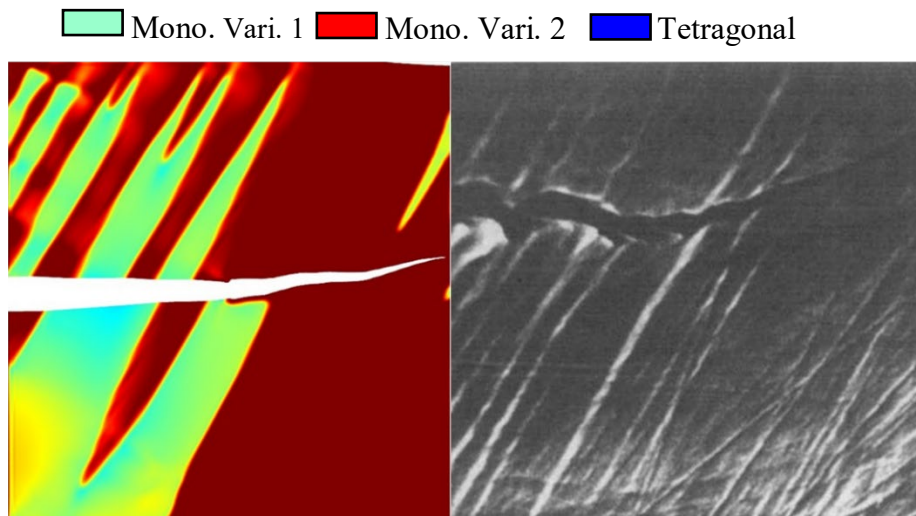


**Figure 5.** Comparison of the coupled PF simulation of martensitic transformation and crack propagation result with the experiment [20,70].

## Temporal and Spatial Evolution of Concurrent T→M Transformation and Crack Propagation in A Single Crystal Tetragonal Zirconia

In this section, we investigate the propagation of an edge crack, mode I, in a single crystal tetragonal zirconia. In these simulations, we consider the lattice orientation angle to be zero degrees, i.e.  $\theta = 0^\circ$  in Figure 4, which indicates that the  $a_t$  axis in the tetragonal phase is horizontal.

Figure 6 shows the temporal and spatial co-evolution of t→m transformation and crack propagation under the mode I of fracture. Initially, the whole domain is tetragonal. Since the thermal driving force is not adequate to initiate the t→m transformation, external loading is needed. As we apply the external loading ( $1 \text{ MPa/s}$ ), higher stresses and corresponding strains at the crack tip facilitate the t→m transformation. After t→m initiation at the crack tip, phase transformation propagates toward the regions ahead of the crack tip. Phase transformation continues by increasing the external loading until the whole domain transforms to the monoclinic. The predicted microstructure has the twin plane of  $(100)_m$  which is consistent with experimental observations [91,92]. For the specific conditions of this simulation, such as temperature, loading rate, boundary conditions, etc. crack propagation starts when the majority of the domain has transformed to monoclinic. Because of the loading at the upper part of the domain, the top half of the domain is able to deform as the crack grows. This deformation changes the microstructure and favors the formation of the more strain-accommodating monoclinic variant against the other one. Therefore, the upper part of the domain completely transforms to a single variant monoclinic. This observation is also in agreement with several theoretical and experimental works that showed the formation of unbalanced

martensitic variants under different loadings [23,93]. While it is expected that the crack grows in a straight line, due to mode I loading and isotropic fracture property, the results show that the crack would grow in an anomaly path which is heavily dependent on crystal lattice orientation of zirconia.

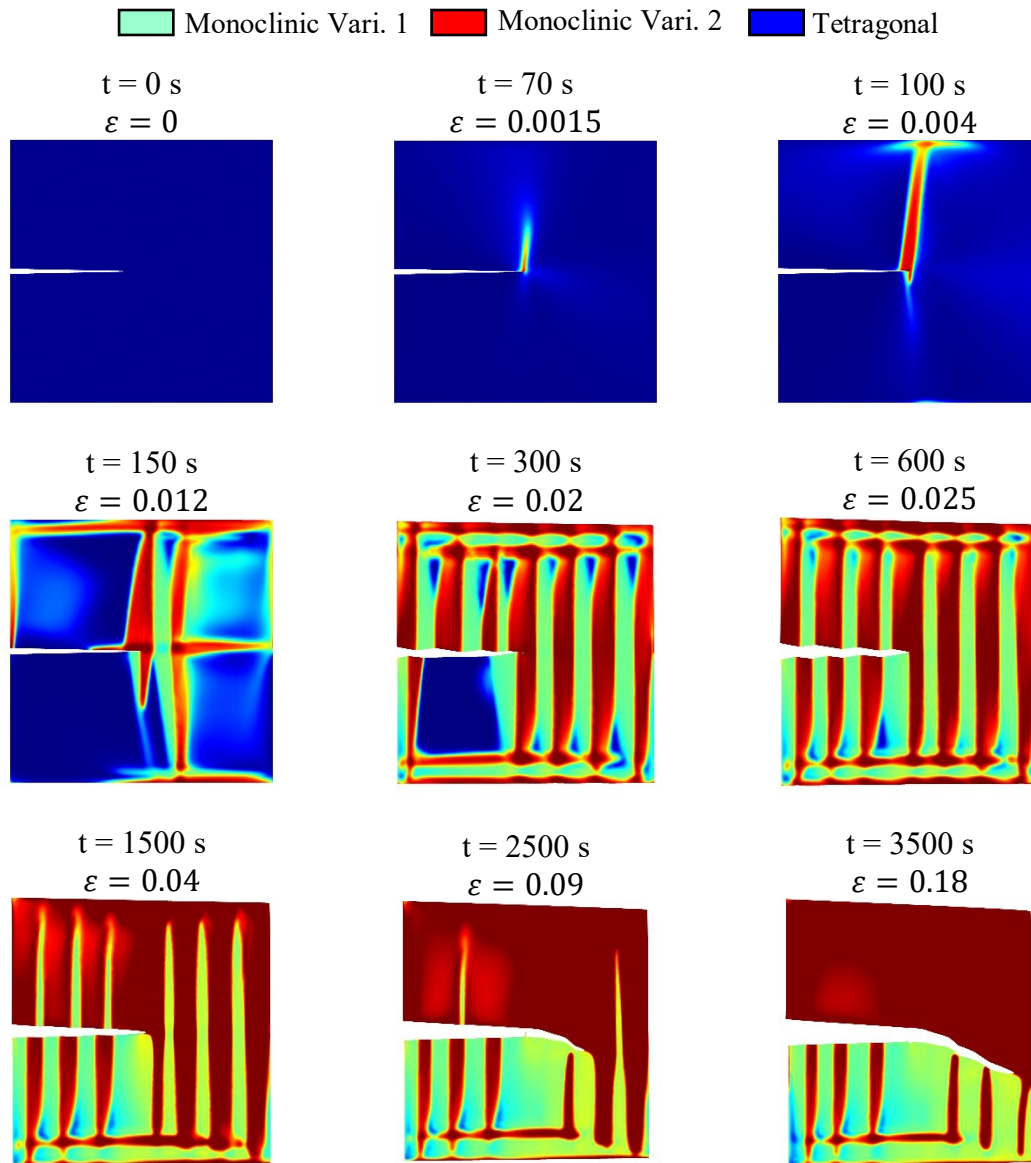


**Figure 6.** The co-evolution of  $t \rightarrow m$  transformation and crack propagation in zirconia under the mode I loading for lattice orientation angle of zero degrees,  $\theta = 0^\circ$ .

Figure 7 shows the stress–strain curve for a faulted single crystal tetragonal zirconia at low strains and the corresponding domain microstructure at different loading conditions. The stress-strain curve is elastic at low stresses, before the initiation of  $t \rightarrow m$  transformation at the crack tip. By  $t \rightarrow m$  initiation and propagation there is an almost flat part in the stress-strain curve due to generated strains during monoclinic propagation. The curve again shows hardening when the microstructure becomes dominantly monoclinic and finally, the curve gets again flattened as the crack grows. We note that Figure 7 is a load-controlled crack propagation simulation and the external stress is continuously increasing. Therefore, we do not observe the typical load drop which is common in displacement-controlled fracture tests and simulations.

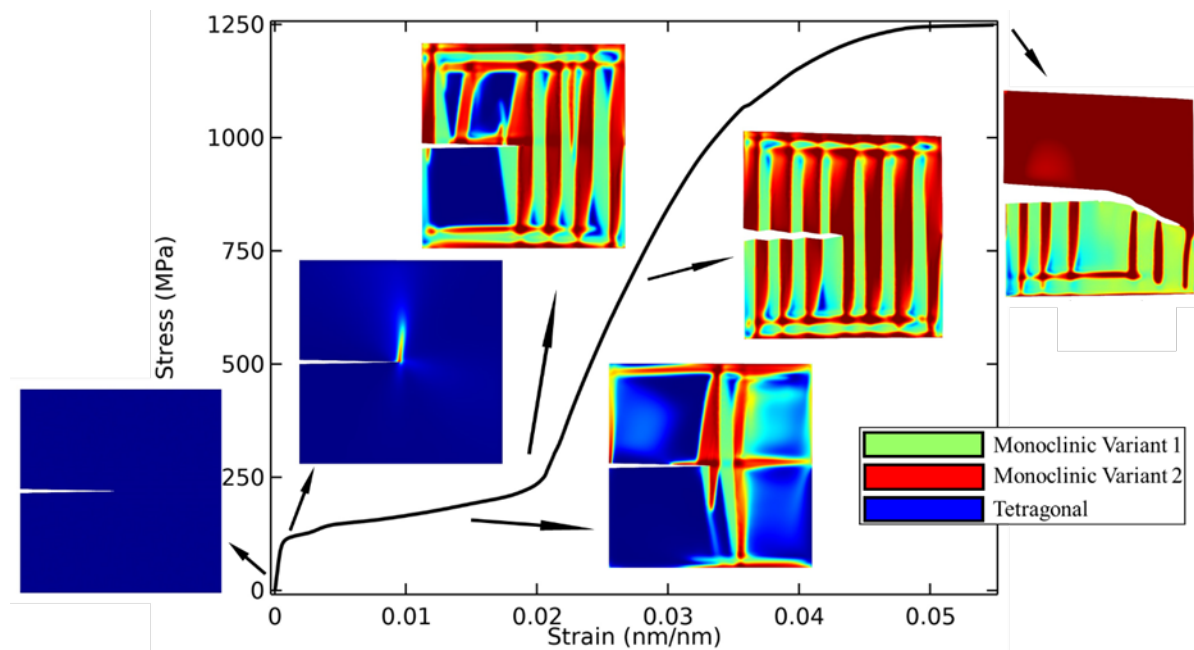


**Figure 7. The stress–strain curve for single crystal tetragonal zirconia under uniaxial tension and its corresponding microstructure evolution and deformed shapes.**

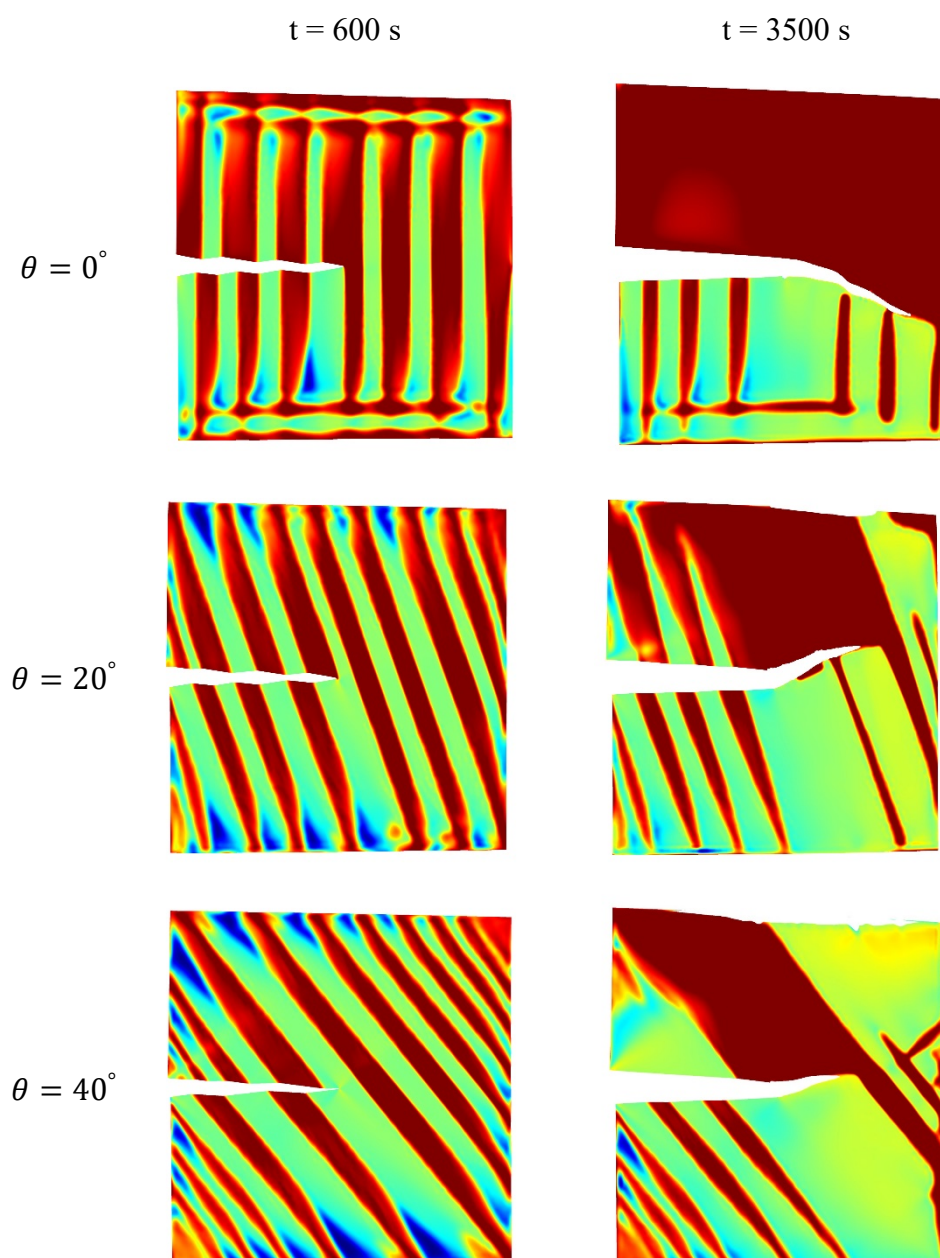
### The Effect of Crystal Lattice Orientation

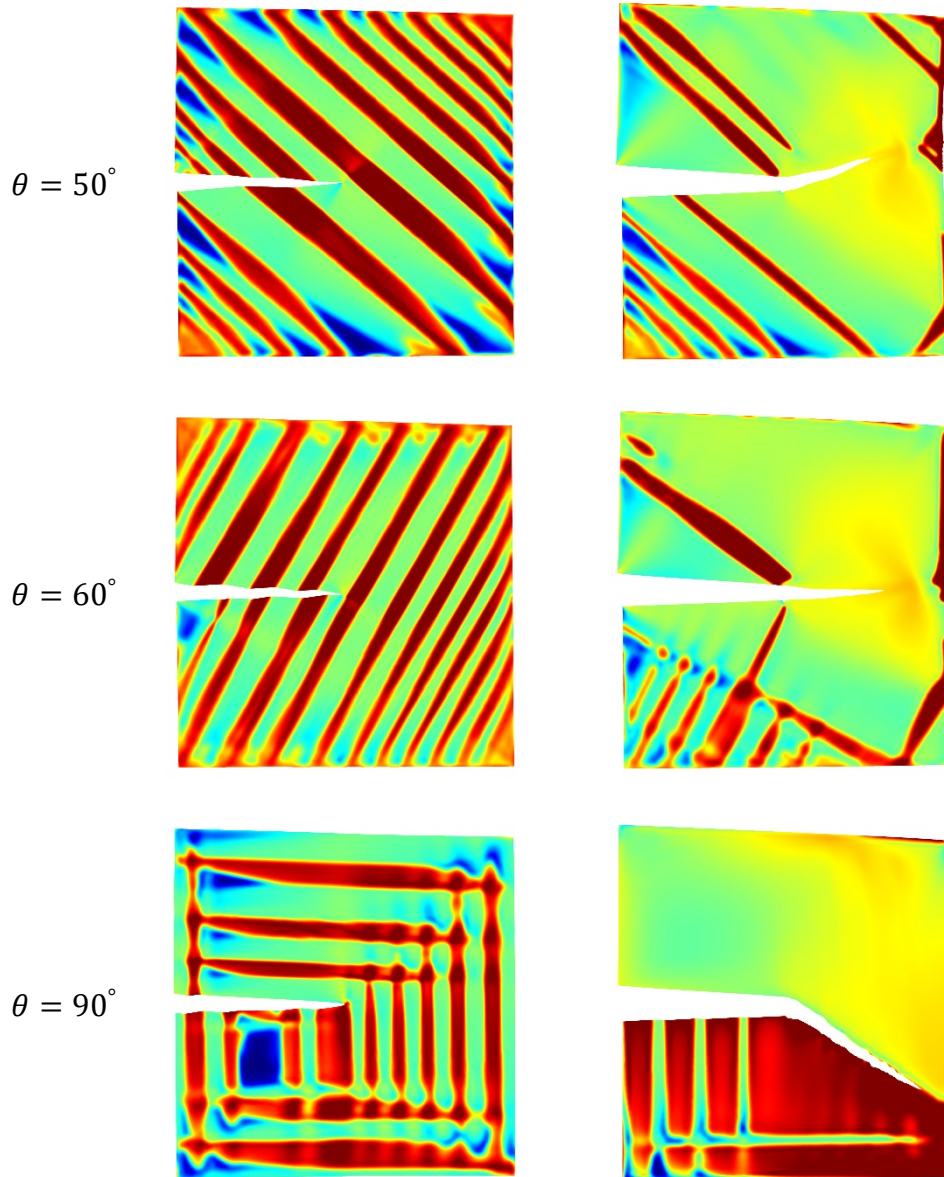
Microstructural patterning during MT is highly dependent on loadings, boundary conditions, and crystal lattice orientations. To elucidate the role of crystal lattice orientation on crack propagation, we investigate the effect of lattice orientation on crack propagation in a single crystal tetragonal zirconia. Loadings and boundary conditions for all these simulations are similar to Figure 4.

Figure 8 shows the crack propagation behavior for six different lattice orientation angles,  $\theta = 0^\circ, 20^\circ, 40^\circ, 50^\circ, 60^\circ,$  and  $90^\circ$  for two different simulation times,  $t = 600$  s, and 3500 s. The initial conditions of all these simulations was a crack notch in a fully tetragonal phase, similar to  $t = 0$  s in Figure 6. At  $t = 600$  s most of the tetragonal phase transformed to monoclinic for all lattice orientations. Main monoclinic phases that form in all simulations have  $(100)_m$  and  $(001)_m$  junction planes, the plane between two different martensite variants, which have been observed in several experimental studies [7,8,27,91,92,94].

The simulation results show that by changing the crystal lattice orientation, the crack growth path, as well as the amount of crack growth (toughening effect), change greatly. This observation clearly indicates that the crystal lattice orientation has a significant influence not only on the crack growth path but also on the magnitude of the transformation toughening.

Monoclinic Vari. 1 Monoclinic Vari. 2 Tetragonal





**Figure 8.** The effect of crystal lattice orientation on the crack growth in a single crystal tetragonal zirconia under the mode I loading. The left and right columns show the concurrent evolution of  $t \rightarrow m$  transformation and crack growth at the times of 600 s and 3500 s, respectively.

We studied the effect of crystal lattice orientation more quantitatively by plotting the applied external stress versus normal average strain in the  $y$ -direction in Figure 9. In these studies, we ran all the simulations for a fixed time with a similar constant loading



rate. Due to the dominant contribution of crack growth on the strain in Figure 9, the higher strains represent more crack growth length. Similarly, a comparison of the different curves in Figure 9 at constant strains indicates that crystal lattice orientations which show higher stresses are more crack resistant, i.e. show stronger crack toughening. Having these metrics in mind, Figure 9 shows that the transformation toughening increases as the crystal lattice orientation increases from  $0^\circ$  to  $50^\circ$  and then decreases from  $50^\circ$  to  $90^\circ$ . A more holistic study of the crystal lattice orientation, from  $0^\circ$  to  $180^\circ$ , leads to the following observations.

- 1) Crystal lattice orientations from  $10^\circ$  to  $50^\circ$  have crack paths that make positive slopes with initial crack surface and the crack path gets straight, zero slopes, at  $60^\circ$ . Then the crack path makes a negative slope with the initial crack surface for crystal lattice orientations of  $70^\circ$  to  $90^\circ$ . For crystal orientations above  $90^\circ$ , the crack path makes a positive slope reaching the peak at approximately  $140^\circ$ . Then the slope of the crack path reduces gradually to the most negative slope at  $180^\circ$ .
- 2) Changing the crystal lattice orientation changes the dominant monoclinic variant at the top surface of the growing crack. For lattice orientations between  $0^\circ$  to  $45^\circ$ , the variant 2 (red color) is dominant, while for  $45^\circ$  to  $90^\circ$  the variant 1 (green color) becomes dominant. Moreover, the results for the lattice orientations of  $90^\circ$  to  $180^\circ$  reveal that the monoclinic variants are completely reversed compare to  $0^\circ$  to  $90^\circ$ .

We note that the martensite lathes patterning and consequently the crack growth path are highly dependent on the loading and boundary conditions and above observations are for mode I loading as depicted in Figure 4.

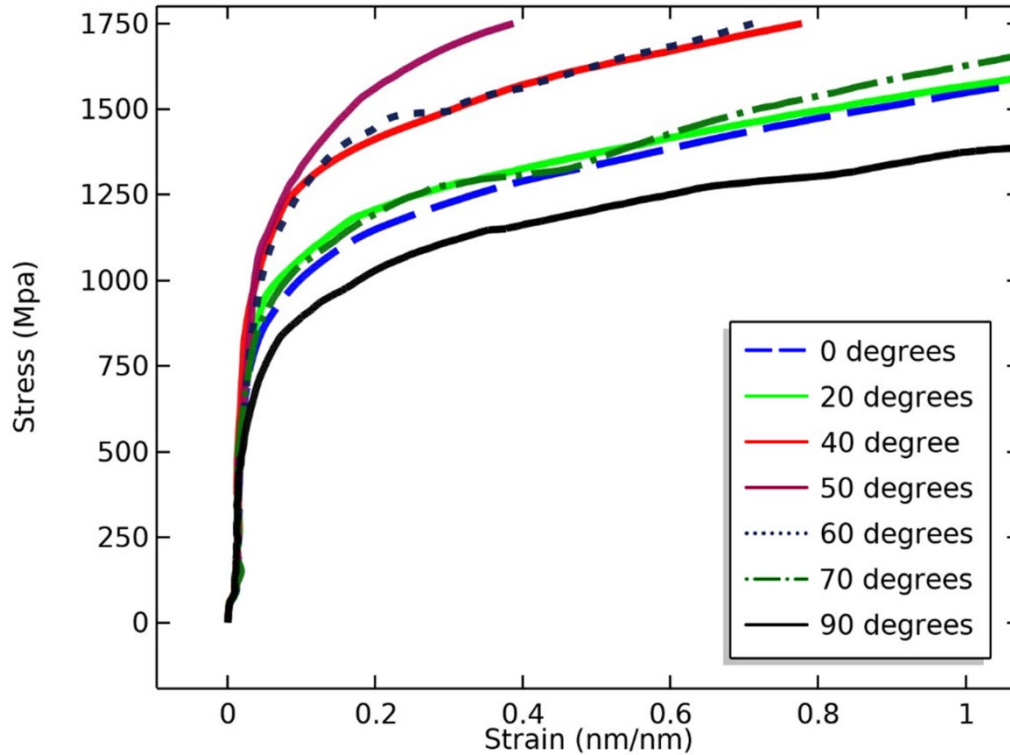


**Figure 9.** The stress-strain curve for crack growth in tetragonal zirconia single crystal with different lattice orientation angles. The loading rate and simulation time are consistent for all simulations. Lattice orientations of 50° and 90° show the maximum and minimum transformation toughening, respectively.

### Crack Propagation in Transformable Versus Untransformable Zirconia

To study the effect of  $t \rightarrow m$  transformation on the fracture behavior of zirconia, we compared the crack propagation of single crystal tetragonal zirconia with and without the phase transformation. In the latter case, we artificially turned off the phase transformation equation, i.e. Eq. 26. Figure 10 shows a comparison between transformable and untransformable zirconia. The first and second columns in Figure 10 show the crack nucleation and propagation in untransformable and transformable zirconia, respectively. In these two columns, the blue domains demonstrate the intact phase ( $\phi = 0$ ), while the red domains illustrate the cracked phase ( $\phi = 1$ ), and the other colors indicate the transitional phases ( $0 < \phi < 1$ ). The third column shows the corresponding

microstructure evolution for the transformable case. Figure 10 clearly shows the effect of  $t \rightarrow m$  transformation on transformation toughening in zirconia. For the untransformable case, the crack starts to grow at  $t = 1000$  s and complete fracture happens at  $t = 2000$  s. While for the case of the transformable zirconia, due to the dilatational strain associated with the phase transformation, the crack propagation is much slower.

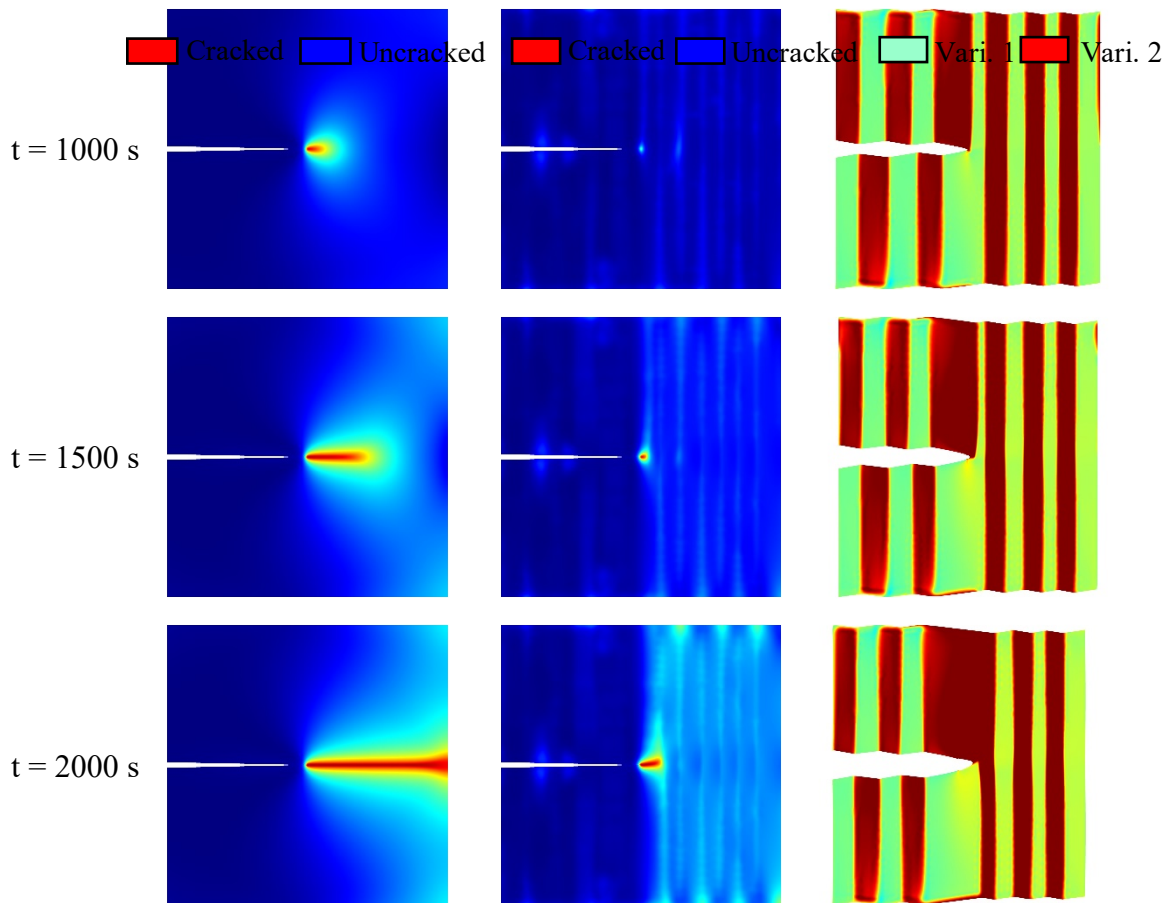


**Figure 10.** The comparison between crack propagation in single crystal tetragonal zirconia with and without phase transformation. The left column shows the crack propagation in untransformable zirconia (phase transformation is artificially turned off), the middle column shows the crack growth in transformable zirconia, and the right column shows the corresponding microstructure for the transformable case.

Figure 11 shows a more quantitative comparison between the stress-strain curves for the edge notched single crystal for transformable and untransformable zirconia. The stress in this plot is the external loading, which increases with time. Therefore, we do not see the typical load drop, which is common for constant displacement tests, as the crack grows. Figure 11 shows that the fracture happens at the higher loads for the transformable zirconia compared to the untransformable one, which indicates to the transformation toughening effect. The difference between the stress-strain curves in Figure 11 at the early stages of loading is due to the  $t \rightarrow m$  transformation which leads to flat stress-strain curve for the transformable case.

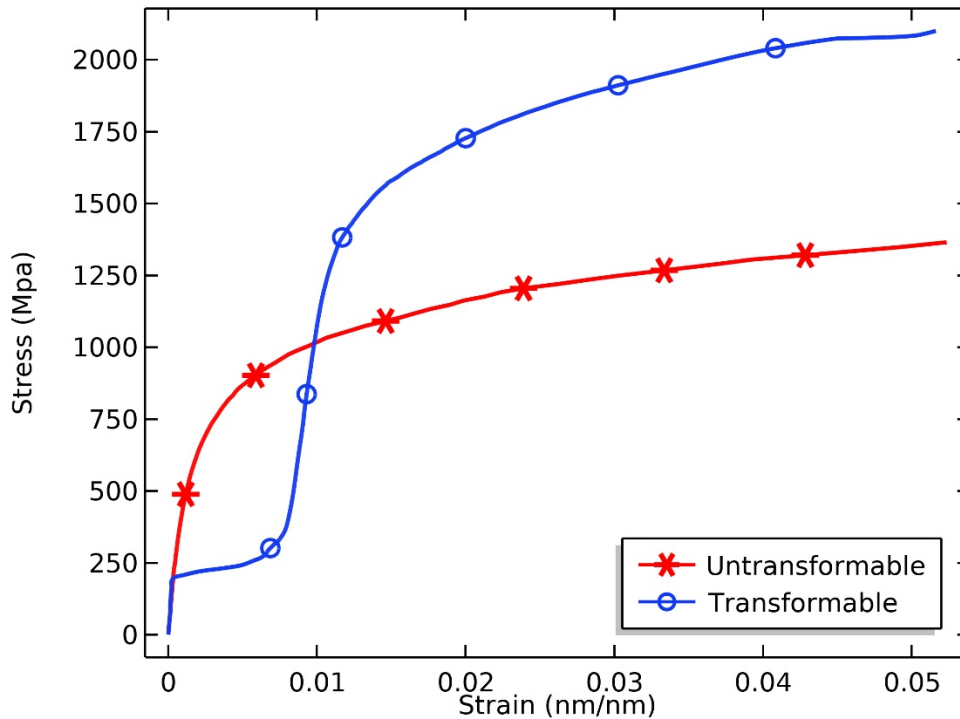


**Figure 11. The stress-strain curve for transformable and untransformable single crystal tetragonal zirconia upon loading to crack growth initiation.**

To elucidate the contribution of elastic anisotropy and phase transformation on the crack propagation path, we have studied and compared the crack growth in three cases: 1) elastic isotropic, 2) elastic anisotropic, and 3) elastic anisotropic with phase transformation under displacement control loading. For elastic isotropic model, we considered the Young modulus of 210 GPa and Poisson's ratio of 0.3.

Figure 11 shows that the crack propagation path for elastic isotropic and anisotropic cases are fairly similar which indicates the minor effect of elastic anisotropy on the crack propagation path. However, it is the MT and its patterning which is the key player in determining the crack propagation path in SMCs.

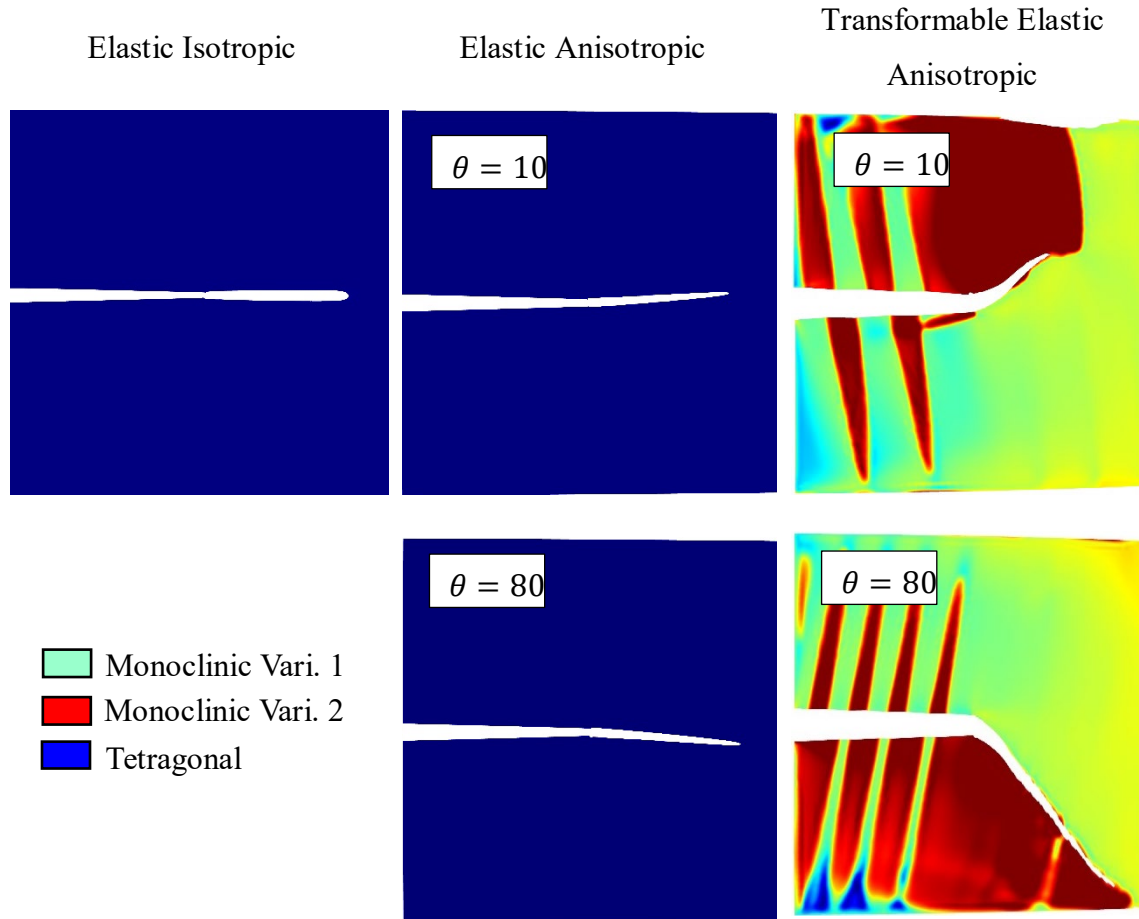


**Figure 12.** Comparisons between crack propagation path in elastic isotropic, elastic anisotropic, and transformable elastic anisotropic models show that the MT is the dominant physics in SMCs cracking.

Figure 13 shows the fracture energy release rate,  $G$ , versus crack extension for two stresses, 900 MPa and 1100 MPa. While the energy release rate is proportional to the square of the applied stress, we observe similar  $G$  for 900 MPa and 1100 MPa at some crack extension lengths. This discrepancy with classical fracture mechanics is due to the dynamic evolution of microstructure during crack propagation and the differences between the time scales for 900 MPa and 1100 MPa to reach the same crack extension, i.e. crack grows faster for higher stress. Therefore, for similar crack extension for 900 MPa and 1100 MPa, we have different microstructures that provide different toughening

effects and consequently, the  $G$  is not solely function of external stress and crack length for transformable materials.

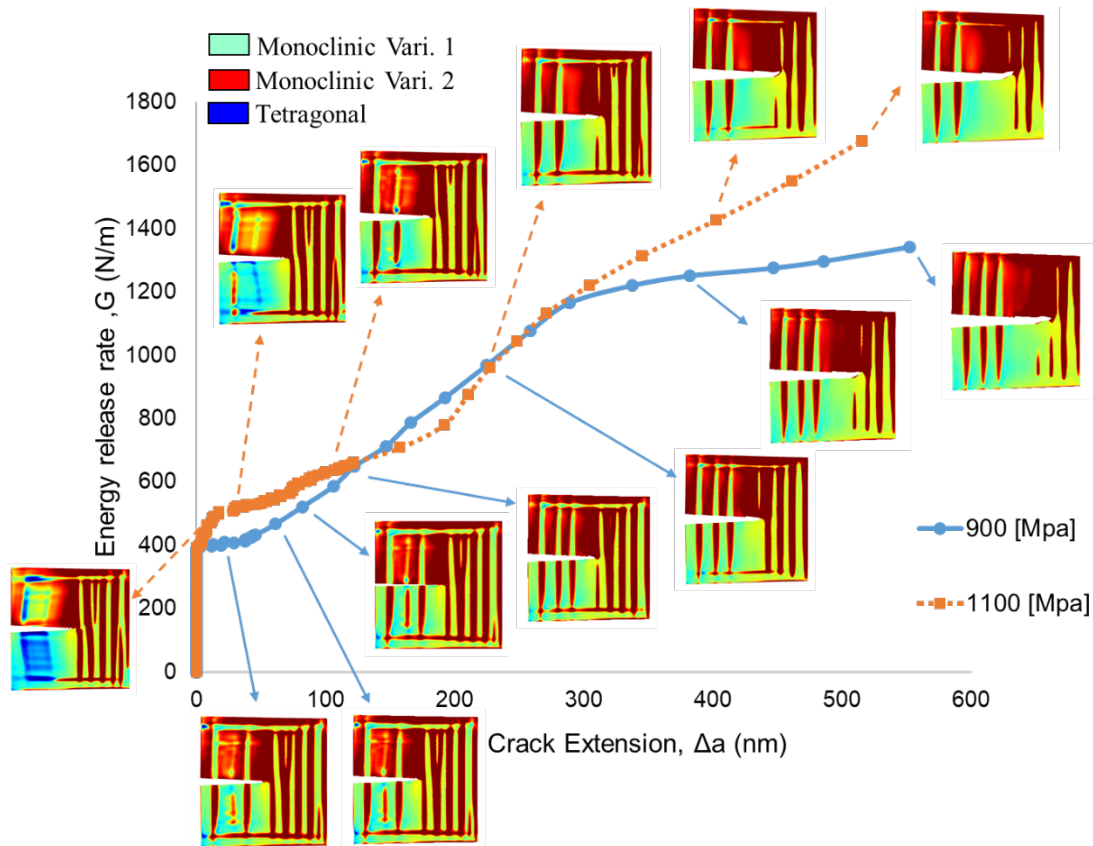


**Figure 13.** Energy release rate versus crack extension for a single crystal zirconia for  $\sigma=900$  and 1100 MPa. Dynamic evolution of the microstructure during the crack propagation and its associated toughening effects, lead to higher energy release rate for 900 MPa compared to 1100 MPa for crack extensions between 120 nm to 250 nm.

### Conclusion

In this chapter, we used the phase field method to couple the martensitic transformation with the variational formulation of brittle fracture. The model is efficiently capable of predicting crack propagation in transformable materials. The model was parameterized for 2D single crystal zirconia and anisotropic elastic properties of the

zirconia were taken into account in the model. The analysis of the crack growth behavior in single crystal zirconia shows an unusual crack growth path at the presence of the martensitic transformation. A comparison between the crack growth in transforming zirconia with the untransformable one reveals the mechanism of phase transformation at the crack tip and its toughening effects. The phase transformation dramatically slows down the crack propagation and reduces the value of the normal stresses in front of the crack tip. The crack propagation path and transformation toughening are strongly dependent to the crystal lattice orientation. Results, for a constrained single crystal under mode I loading, show that the maximum (minimum) transformation toughening happens when the crystal lattice orientation makes the angle of 50 (90) degrees with the crack surface.



## CHAPTER FOUR: POLYCRYSTALLINE MODEL

In this chapter, we parametrize the developed PF model for polycrystalline zirconia and provide the result.

The result provided in this chapter is published as a research paper [95] in the Engineering Fracture Mechanics Journal (Volume 241, January 2021, 107403, <https://doi.org/10.1016/j.engfracmech.2020.107403>).

### **Polycrystalline Model Generation**

In this section, we describe the algorithm that we use to create the two-dimensional (2D) polycrystalline geometry and mesh. The goal is to create a polycrystalline model with different selective grain sizes, grain boundary size, and a suitable tessellation morphology, i.e., Voronoi or grain growth.

First, we use the open-source Neper software [96,97] to create the primary model. However, the Neper does not create the grain boundaries. Therefore, to create an appropriate grain boundary, we use the MATLAB routines developed by Paggi et al. [98]. The polycrystalline geometry and mesh creation algorithm used in this work is as follows:

- 1) We generate polycrystalline models using the Neper software with the following command:

```
neper -T -n 10 -id 1 -reg 1 -dim 2 -format geo -o 10Zirconia -domain
"square(2000,2000)" -morpho "diameq:dirac ,sphericity:lognormal(1,0.03)"
```

This command would create a 2D 2000 x 2000 (in this work nm<sup>2</sup>) polycrystalline model with a grain growth morphology. The number of grains generated by the above

command would be 10, which are approximately equal in size, and the generated file format would be geo.

- 2) The generated geometry in step 1 is imported into Gmsh software [99] to create an appropriate mesh. Using the Gmsh software, the msh file is exported.
- 3) The msh file has to be divided into lines, nodes, and elements before the grain boundary generation based on the Paggi's et al. Matlab code [98].
- 4) We have modified the Paggi's Matlab codes to create internal grain boundaries and generate an msh format output.
- 5) The msh file will be imported into Gmsh software and exported as a bdf file, which is acceptable in COMSOL.
- 6) The final step is to import the file into the COMSOL for multiphysics simulation.

The procedure of geometry and mesh generation is depicted in Figure 14.

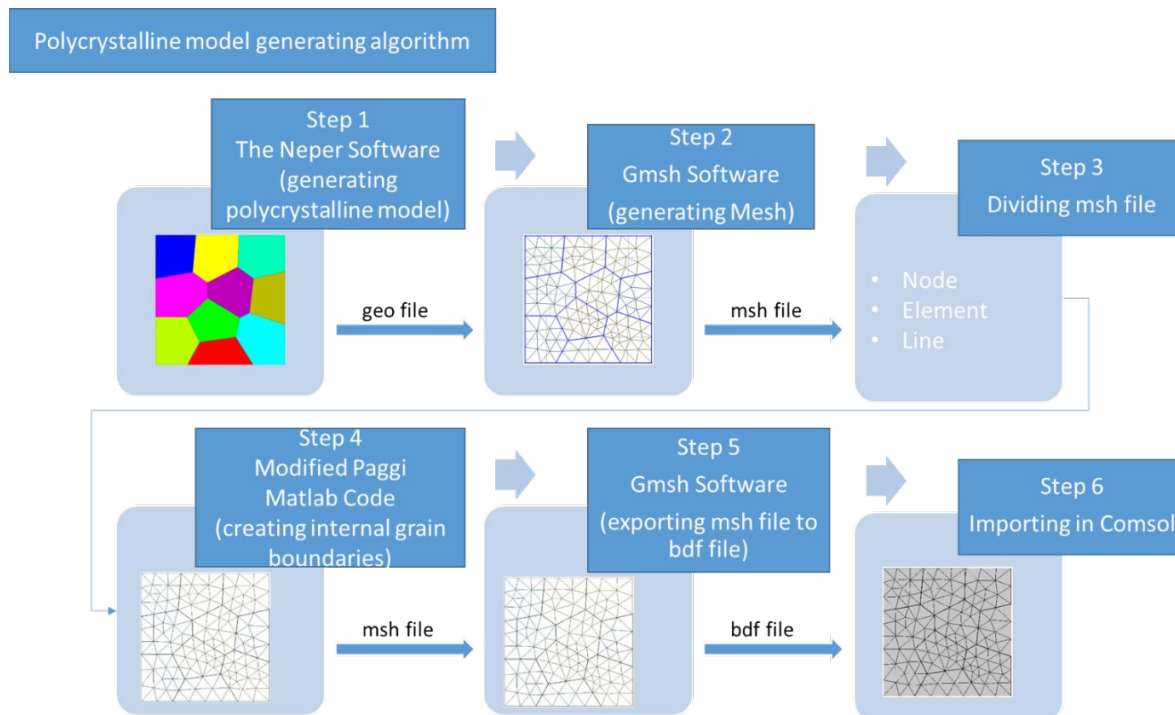


**Figure 13. Algorithm of polycrystalline geometry and mesh generation with distinct internal grain boundaries.**

## Results

In this section, we analyze a 2D Tetragonal Polycrystalline zirconia (TPZ) with a squared geometry of size  $2 \mu\text{m} \times 2 \mu\text{m}$ . The model has an initial edge crack and is embedded in a tetragonal domain, as depicted in Figure 4. The polycrystalline model is

generated using the algorithm described in section 0. Using this algorithm, it is possible to quickly generate a polycrystalline model with different morphology, grain size, and grain boundary size.

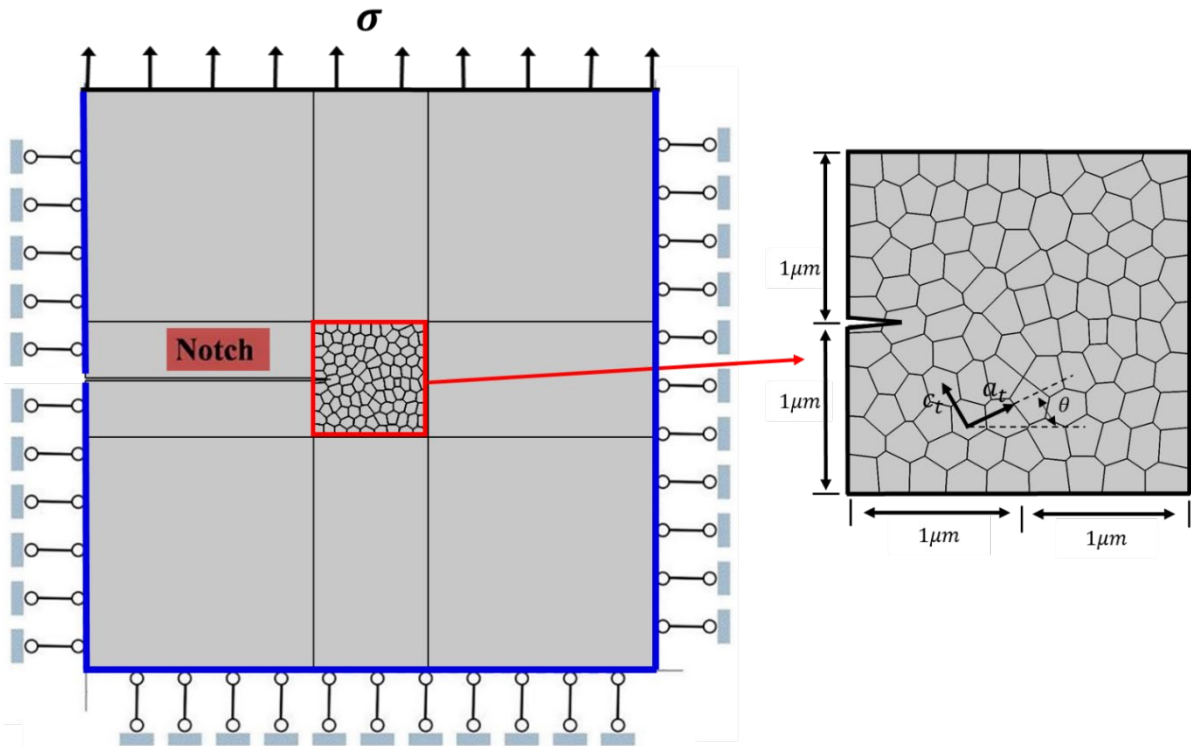


**Figure 14.** The geometry and boundary conditions of the polycrystalline domain embedded in the tetragonal domain.

To assure the numerical convergence, we apply a time-dependent tensile load of  $\Delta\sigma = 1 \text{ MPa/s}$  at the upper boundary of the model. Table 4, Table 5 and Table 6 provide the numerical inputs of the model.

**Table 4. Monoclinic zirconia elastic constants (Gpa) [49].**

$C_{11}$	$C_{22}$	$C_{33}$	$C_{44}$	$C_{55}$	$C_{66}$
361	408	258	100	81	126

$C_{12}$	$C_{13}$	$C_{16}$	$C_{23}$	$C_{26}$	$C_{36}$	$C_{45}$
142	55	-21	196	31	-18	-23

**Table 5. Tetragonal zirconia elastic constants (Gpa) [49,100].**

$C_{11}$	$C_{33}$	$C_{44}$	$C_{66}$	$C_{12}$	$C_{13}$
327	264	59	64	100	62

**Table 6. Numerical parameters utilized in the model calculations.**

Temperature (K) [49]	1170
Chemical driving force, $\Delta G$ ( $J.mol^{-1}$ ) [49]	800 ( $36.8 \times 10^6 J.m^{-3}$ )
Gradient energy coefficient, $\beta$ ( $J.m^{-1}$ ) [49]	$1 \times 10^{-8}$
Energy density coefficient, $a$ [49]	0.14
Energy density coefficient, $b$ [49]	12.42
Energy density coefficient, $c$ [49]	12.28
Kinetic coefficient, $L$ ( $m^3.J^{-1}.s^{-1}$ )	$2 \times 10^{-9}$
Critical energy release rate inside grains, $G_c$ ( $J.m^{-2}$ ) [69]	4.33
Fracture energy ratio ( $G_{GB}/G_G$ ) for pure zirconia	0.2
Fracture energy ratio ( $G_{GB}/G_G$ ) for yttrium stabilized zirconia	0.4
Crack elasticity modification parameter, $k$	$1 \times 10^{-9}$

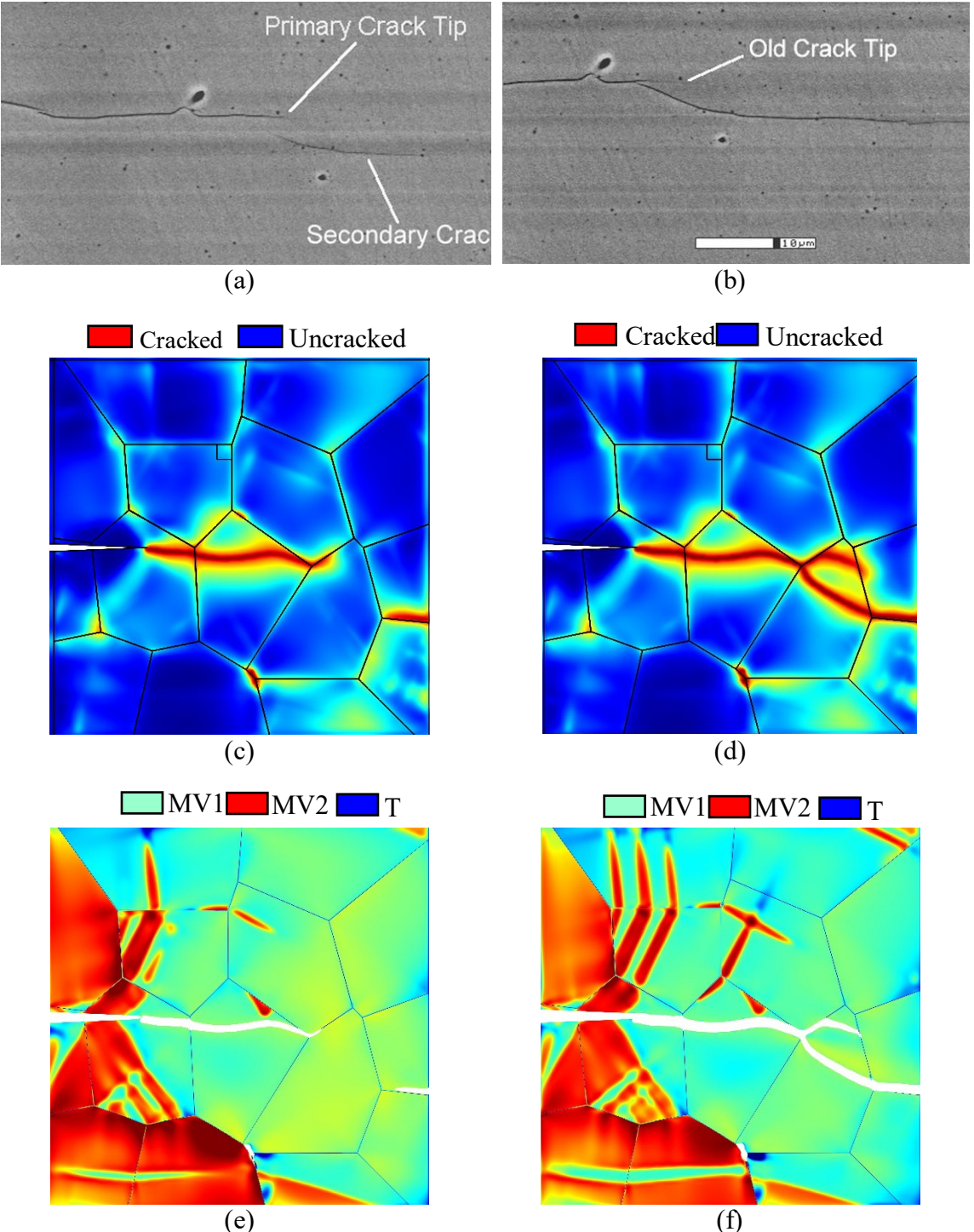
The length parameter, $l_0$ (nm)	20
t→m transformation strains, $\varepsilon^{00}$ [49]	$\varepsilon^{00}(1)$ $= \begin{bmatrix} 0.0049 & 0.0761 \\ 0.0761 & 0.0180 \end{bmatrix}$  $\varepsilon^{00}(2)$ $= \begin{bmatrix} 0.0049 & -0.0761 \\ -0.0761 & 0.0180 \end{bmatrix}$

### Model Verification

The simulation results have been validated by comparing the crack path patterns in polycrystalline zirconia with the experimental results of Kumar et al. [71]. Kumar et al. [71] reported the formation of three different crack patterns in polycrystalline zirconia. The first observation of Kumar et al. was the formation of a new and separate crack, secondary crack, which was appeared ahead of the primary crack tip. Kumar et al. reported that the secondary crack propagated in both directions, i.e. propagated toward and away from the primary crack tip. The backward growth of the secondary crack deflects toward the primary crack and joins it at the location just behind the primary crack tip. The interaction of the primary and the secondary cracks leads to the primary crack tip closer. Kumar et al. could not explain this observation based on the classical fracture mechanics models as in these models, the highest stress intensity belongs to the primary crack tip, and it is expected that the primary crack should grow. However, the developed model in this work indeed predicts the formation of the secondary crack and the way it communicates with the primary crack. The reason underlying this anomaly

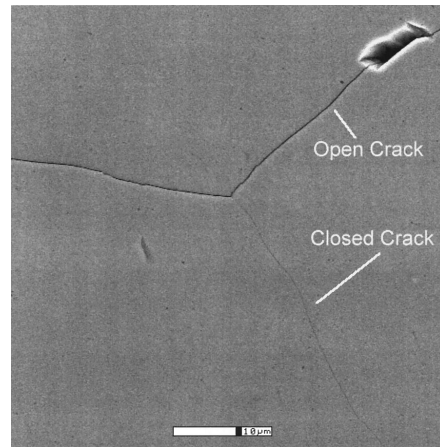
behavior, i.e., primary crack tip closer, is the effects of  $t \rightarrow m$  transformation on zirconia microstructure and its influence on the crack growth path.

Figure 16 shows the crack growth pattern in a polycrystalline zirconia containing 15 grains. First, the primary crack propagates forward. However, after a while, a secondary crack nucleates ahead of the primary crack and propagates in both directions. In its backward propagation, the secondary crack, bend toward the primary crack and arrest its growth.

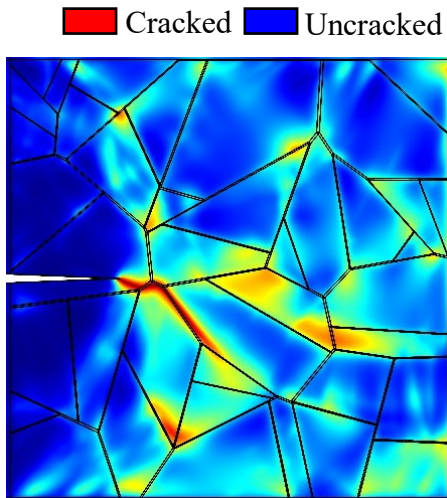


**Figure 16. (a,b) Micrographs showing the secondary crack nucleation, ahead of the primary crack, and backward growth and bending toward the primary crack [71]. (c,d) Simulation results showing the evidence of a secondary crack and its interaction with the primary crack. (e,f) Simulation results showing both microstructure evolution and crack growth simultaneously. (MV1 = Monoclinic Variant 1, MV2 = Monoclinic Variant 2, T = Tetragonal).**

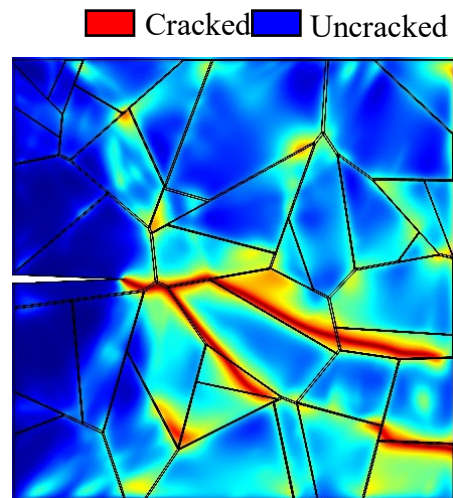
The second form of the crack propagation pattern that Kumar et al. [71] reported was the primary crack branching. Kumar et al. observed that after branching, both branches grow initially, but eventually, one of the branches continues to propagate, whereas the other branch stops. Simulation results in Figure 17 show a similar observation, i.e., the primary crack growth and then branching, and finally, one branch grows, and the other stops.



(a)



(b)



(c)

MV1 MV2 T

MV1 MV2 T



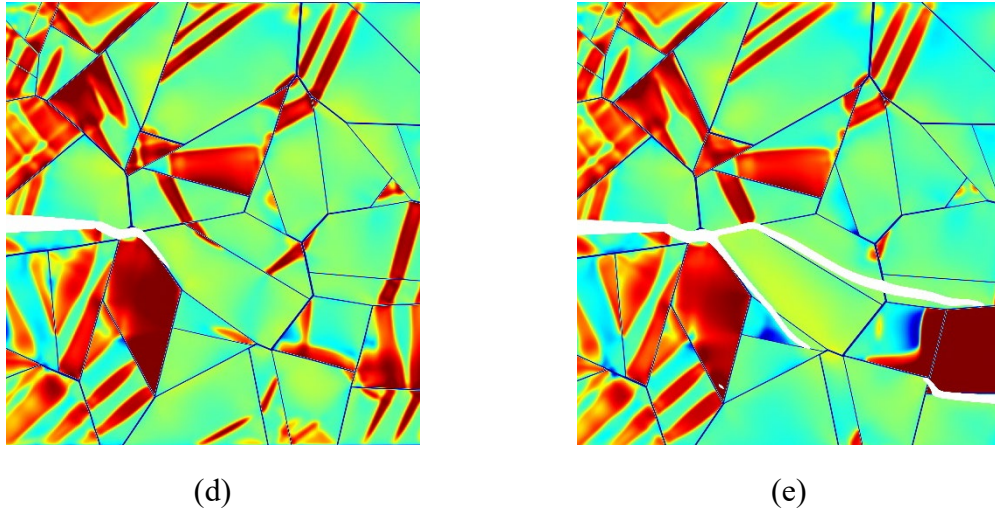
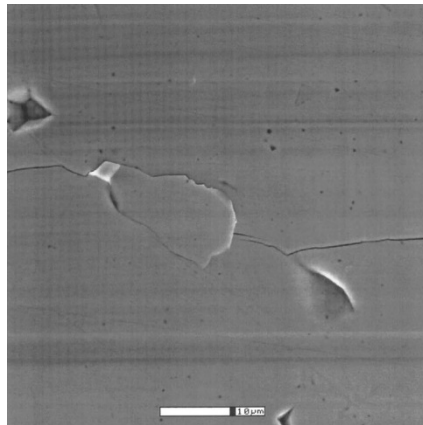
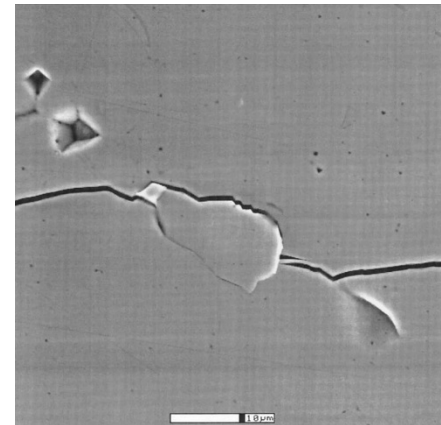


**Figure 17. (a) Micrograph showing a primary crack growth and branching. One branch grows while the other branch stops growing [71]. (b,c) Simulation results showing the crack branching and closer of one branch. (d,e) Simulation results showing both microstructure evolution and crack growth simultaneously. (MV1 = Monoclinic Variant 1, MV2 = Monoclinic Variant 2, T = Tetragonal)**

The last type of crack growth pattern that Kumar et al. reported was grain bridging. In this case, the crack grows along the grain boundary. As the crack grows, the local crack opening increases and the grain is pulled out from its original site. The experimental and simulation observations of this phenomenon are shown in Figure 18.



(a)



(b)

■ Cracked ■ Uncracked

■ Cracked ■ Uncracked

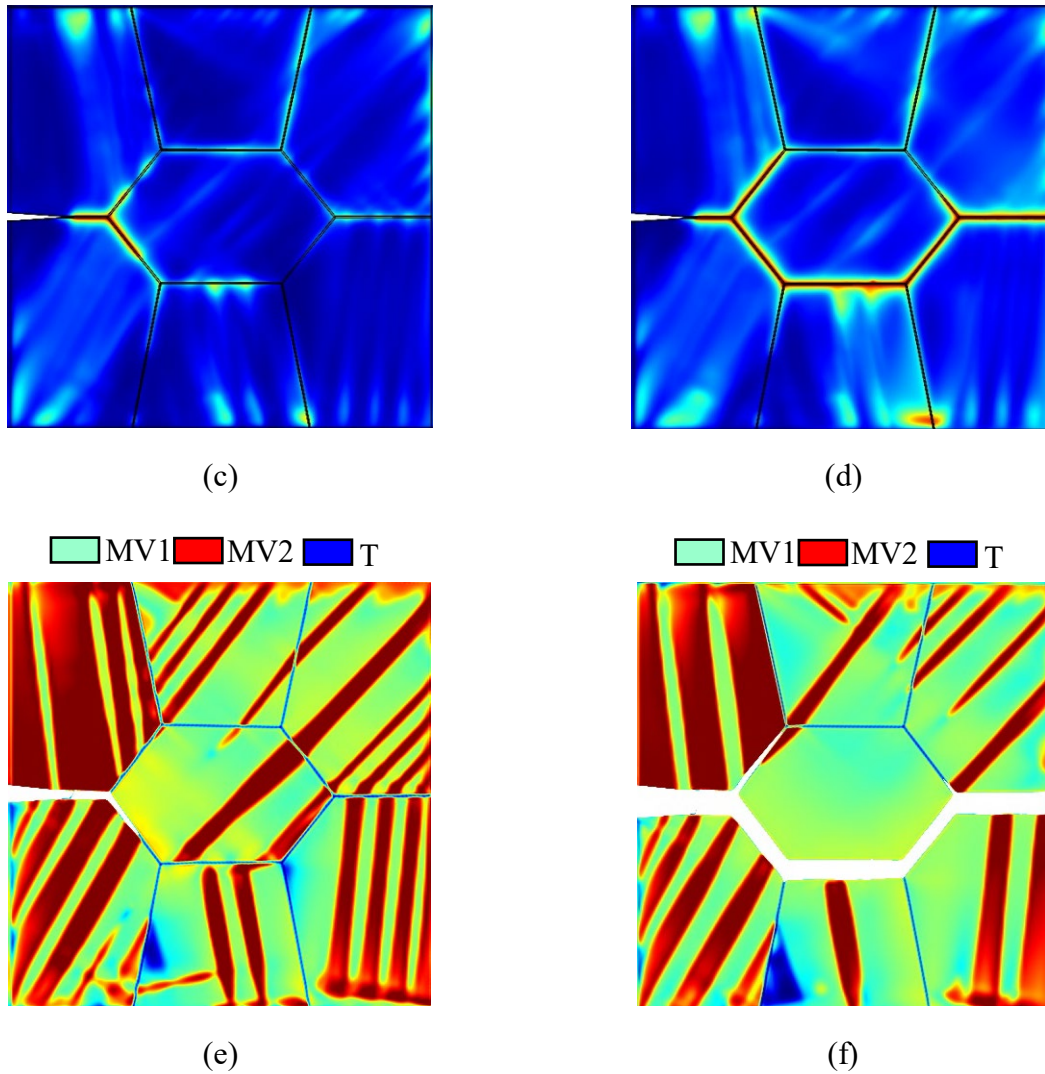
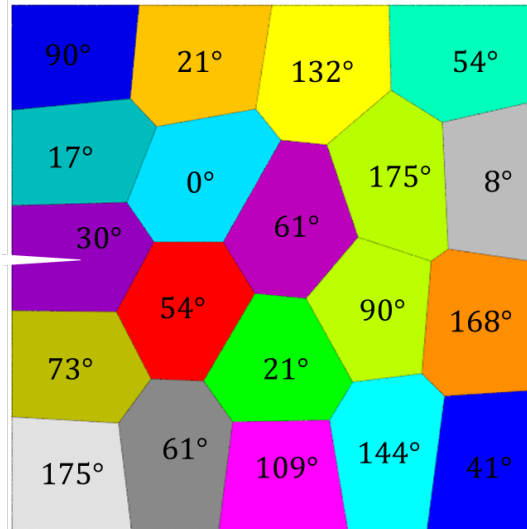


**Figure 18.** (a,b) Micrographs showing interaction between a growing crack and a grain at two stages of crack growth (same location) [71]. (c,d) Simulation results showing the crack grain bridging. (e,f) Simulation results showing both microstructure evolution and crack growth simultaneously. (MV1 = Monoclinic Variant 1, MV2 = Monoclinic Variant 2, T = Tetragonal)

### Temporal and Spatial Evolution of Concurrent T→M Transformation and Crack Propagation in Polycrystalline Zirconia

In this section, we study the concurrent temporal and spatial evolution of the crack growth, mode I, and MT in TPZ. In this simulation, we examine a polycrystalline

microstructure with 20 grains with random lattice orientation angles between 0 to 180 degrees, as depicted in Figure 19.

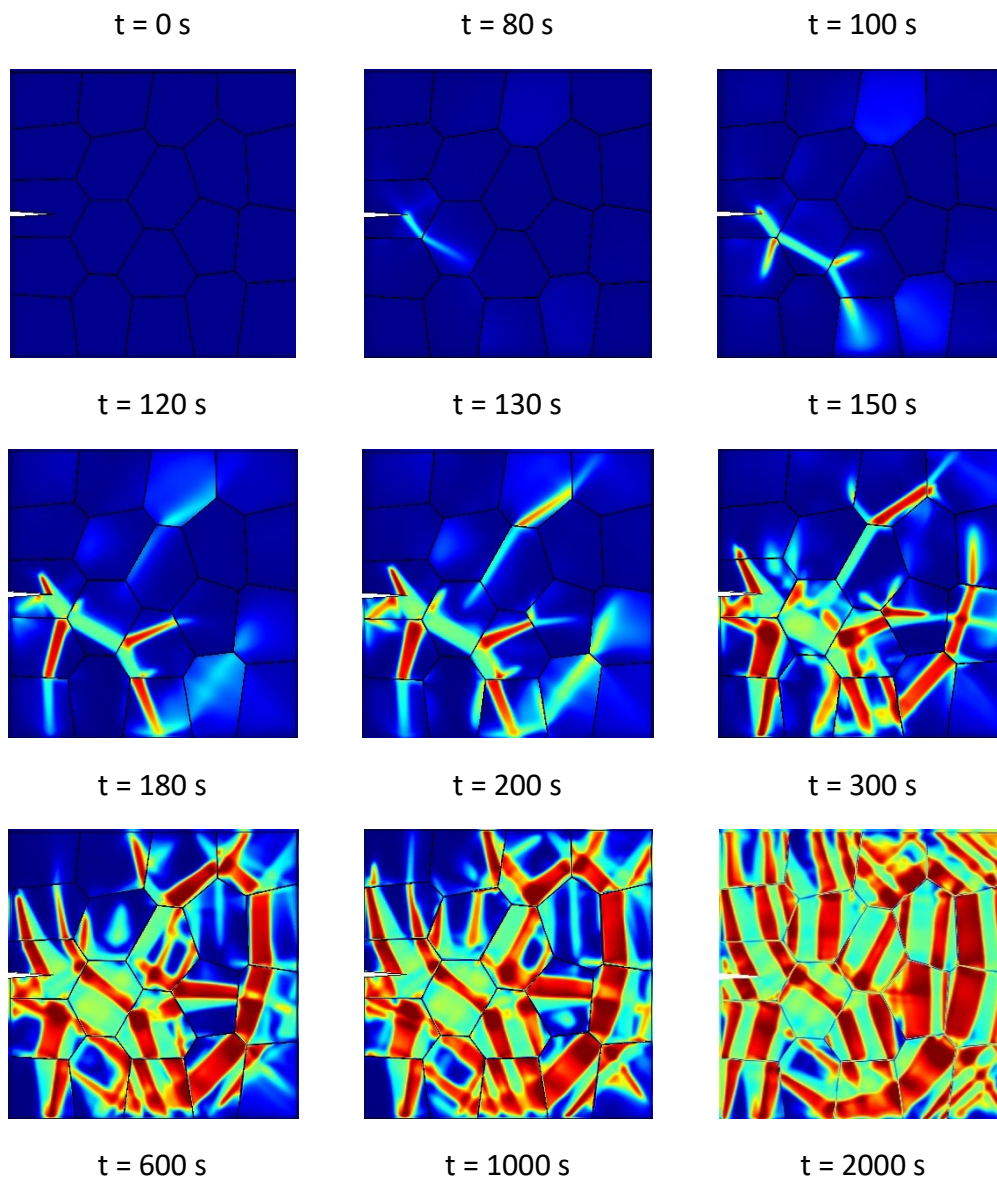


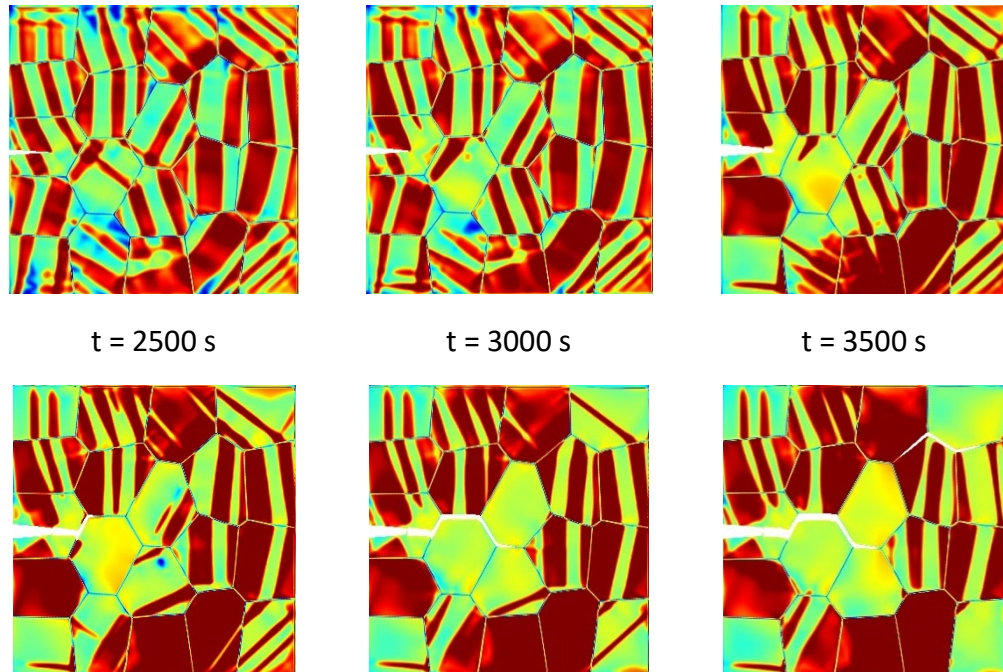
**Figure 15. Polycrystalline configuration and lattice orientation variation in different grains.**

Figure 20 illustrates the co-evolution of MT and fracture in TZP. In the beginning, the tetragonal phase is dominant. Because the thermal driving force is not enough to trigger MT, it is essential to have the external loading to promote the  $t \rightarrow m$  transformation. As we employ the external loading ( $1 \text{ MPa/s}$ ), the higher stresses, and their associated strains, at the crack tip promote the  $t \rightarrow m$  transformation. After  $t \rightarrow m$  initiation at the crack tip, phase transformation spreads at the domains around the crack tip.

When the martensite lathes in one grain grow and reach to the next grain, the local stresses that are much higher than the macroscopic stresses, promote the MT in the neighboring grains. This phenomenon, which is also known as autocatalytic transformation, facilitates the MT spread within the whole domain [8,101]. Figure 20 presents the process of autocatalytic transformation and how it promotes the MT in TPZ.

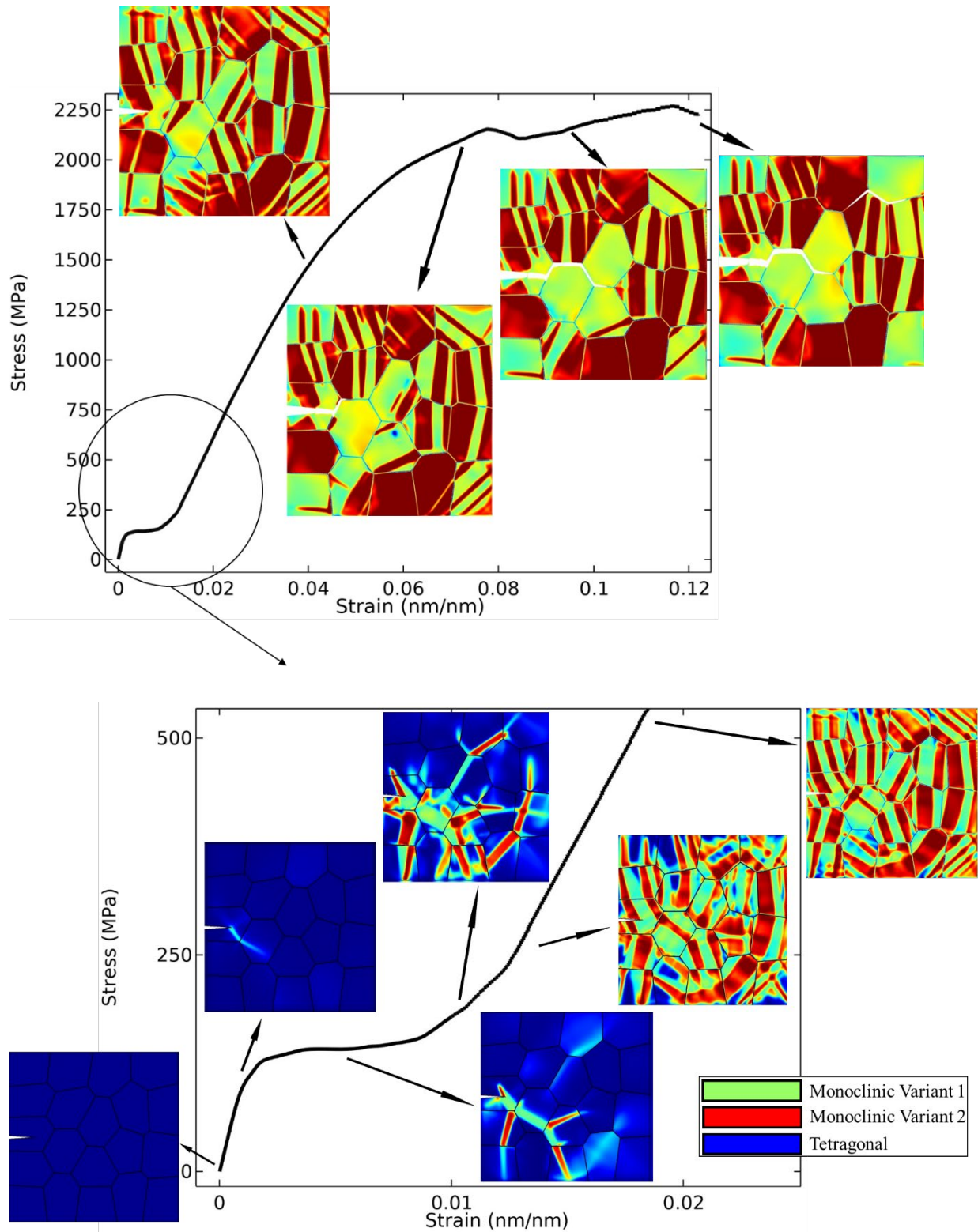
As long as the external load raises, the phase transformation proceeds until the entire domain converts into the monoclinic phase. Microstructure analysis shows the formation of  $(100)_m$  twin planes in the final microstructure that is in agreement with the experimental findings [91,92]. In this study, based on our simulation's initial inputs like boundary conditions, loading rate, etc., the crack begins to grow when most of the field has transformed into the monoclinic.





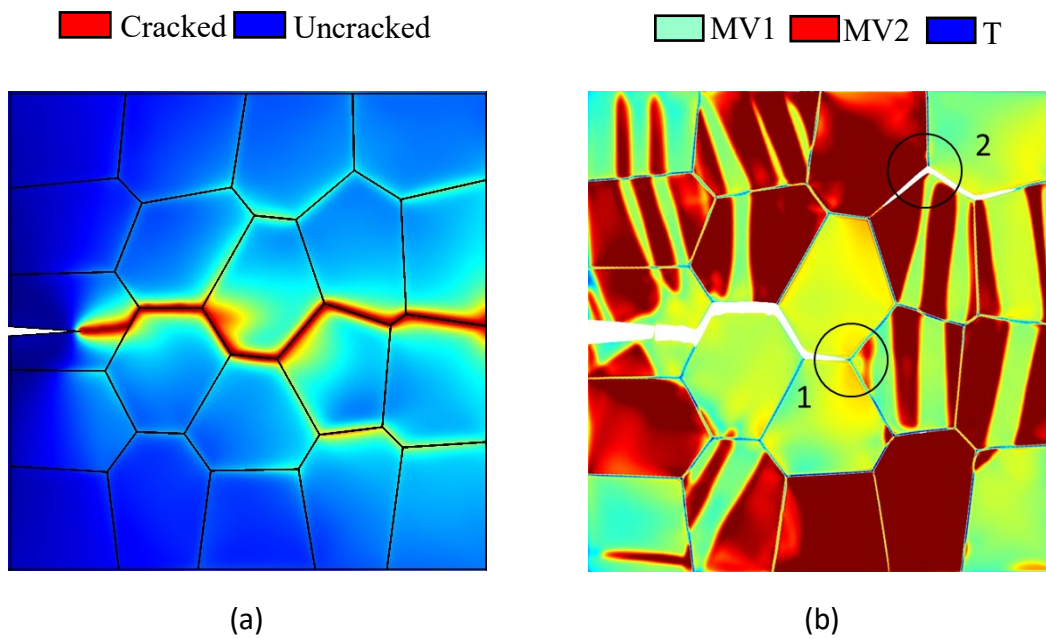
**Figure 16.** The co-evolution of MT and Mode I fracture in TPZ.

Figure 10 shows the stress-strain curve for a TPZ with an initial crack under the Mode I fracture and stress rate of  $1 \text{ MPa/s}$  along with the corresponding microstructure at the different steps. The early stages of the stress-strain curve show a linear elastic behavior. This linear behavior transforms into a flat curve with a negligible hardening by  $t \rightarrow m$  transformation initiation and propagation facilitated by the autocatalytic transformation. The curve shows hardening again when most parts of the domain transform into monoclinic. Eventually, as the crack grows, the stress-strain curve flattens.



**Figure 17.** The stress-strain curve for a faulted TPZ along with the co-evolution of crack and MT.

To elaborate the effects of MT on crack propagation in SMCs, we have compared the crack growth path and stress-strain curve for a transformable microstructure with an untransformable microstructure in Figure 22 and Figure 23, respectively. For polycrystalline materials with intergranular fracture dominancy, it is generally expected that the crack follows the grain boundary typically by chasing the shortest path, as it is possible. To minimize the energy, the customarily expected way would be the nearest route to the straight line, due to the Mode I fracture. This crack behavior is what we see when the microstructure is untransformable, Figure 22-a. However, the results reveal that the crack would propagate in an anomaly route, and it is substantially associated with the crystal lattice orientation of every single grain in the polycrystalline domain, when the microstructure is metastable and can transform. Figure 22-b shows that the crack follows its expected path until  $t = 3000$  s. However, the primary crack stopped then, and a secondary crack started to propagate in the upper section. This anomaly crack growth behavior stems from the changes in the stress state at the crack tip and grain boundaries junctions due to the internal strains associated with MT. The modified stress state makes the crack growth harder in some sites, i.e., spot 1 in Figure 22-b while facilitating crack nucleation and growth in the other sites, spot 2 in Figure 22-b.



**Figure 18.** Crack growth in untransformable TPZ results in an expected, the nearest route to the straight line, crack growth path (a). MT leads to an anomaly crack propagation route in transformable TPZ (b). (MV1 = Monoclinic Variant 1; MV2 = Monoclinic Variant 2, T = Tetragonal).



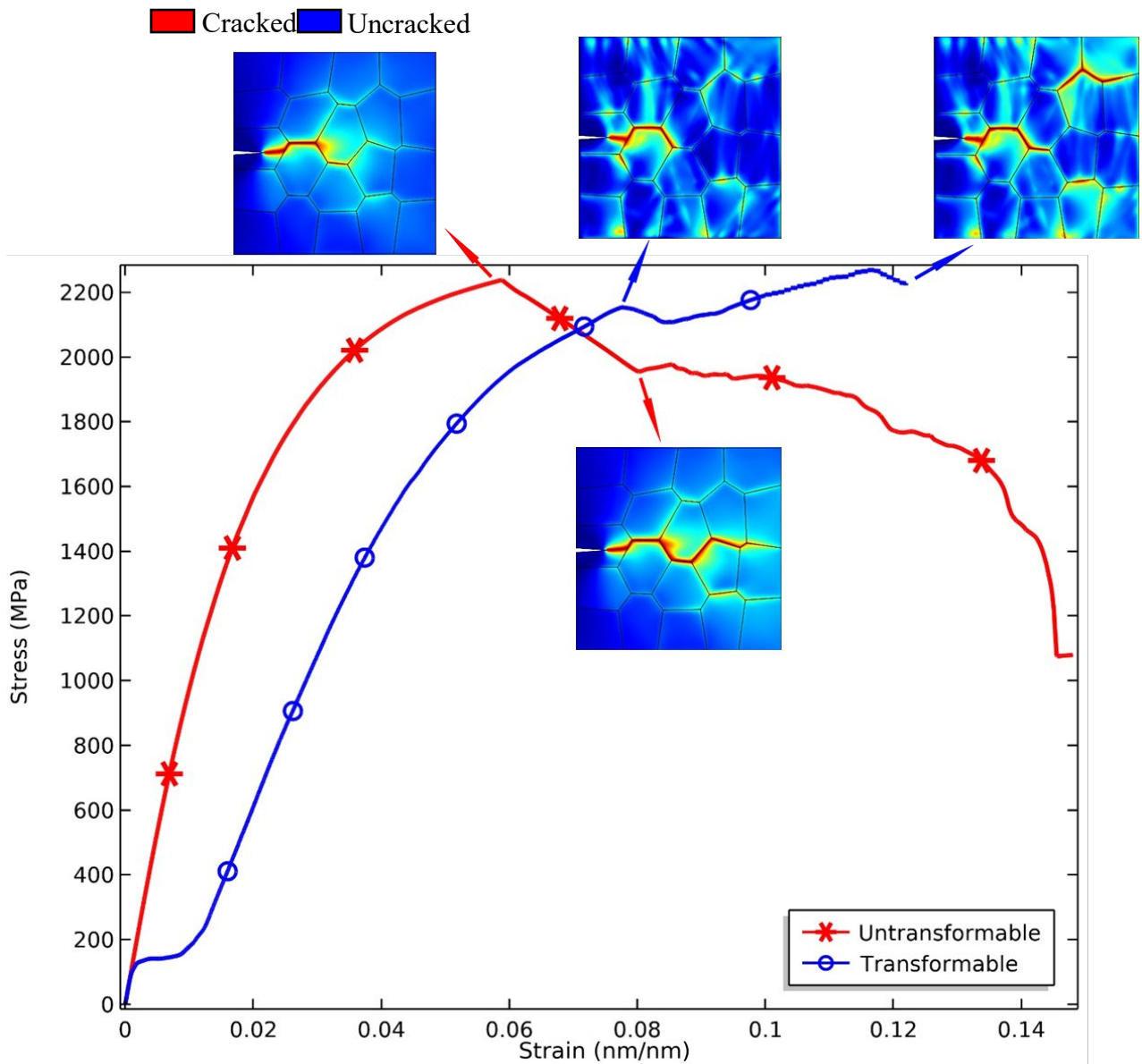


**Figure 19. The stress-strain curve, along with the crack propagation for transformable and untransformable TPZ.**

Figure 23 compares the stress-strain curves for a transformable and untransformable TPZ. Figure 23 shows that the fracture in the transformable case propagates much slower than the untransformable one that indicates to the role of transformation toughening. Two forms of the energy absorption mechanisms in materials with metastable phase contribute into less crack growth in the transformable materials: 1) phase transformation ahead of the crack tip is similar to a non-elastic deformation and

able of absorbing energy otherwise would contribute in crack growth; 2) the volume change during phase transformation can produce several tiny cracks ahead of the bigger crack, and it would significantly enhance the surface area amount created per unit extension of the larger crack and therefore, afterward, substantially raise the absorbed energy during the crack extension [102].

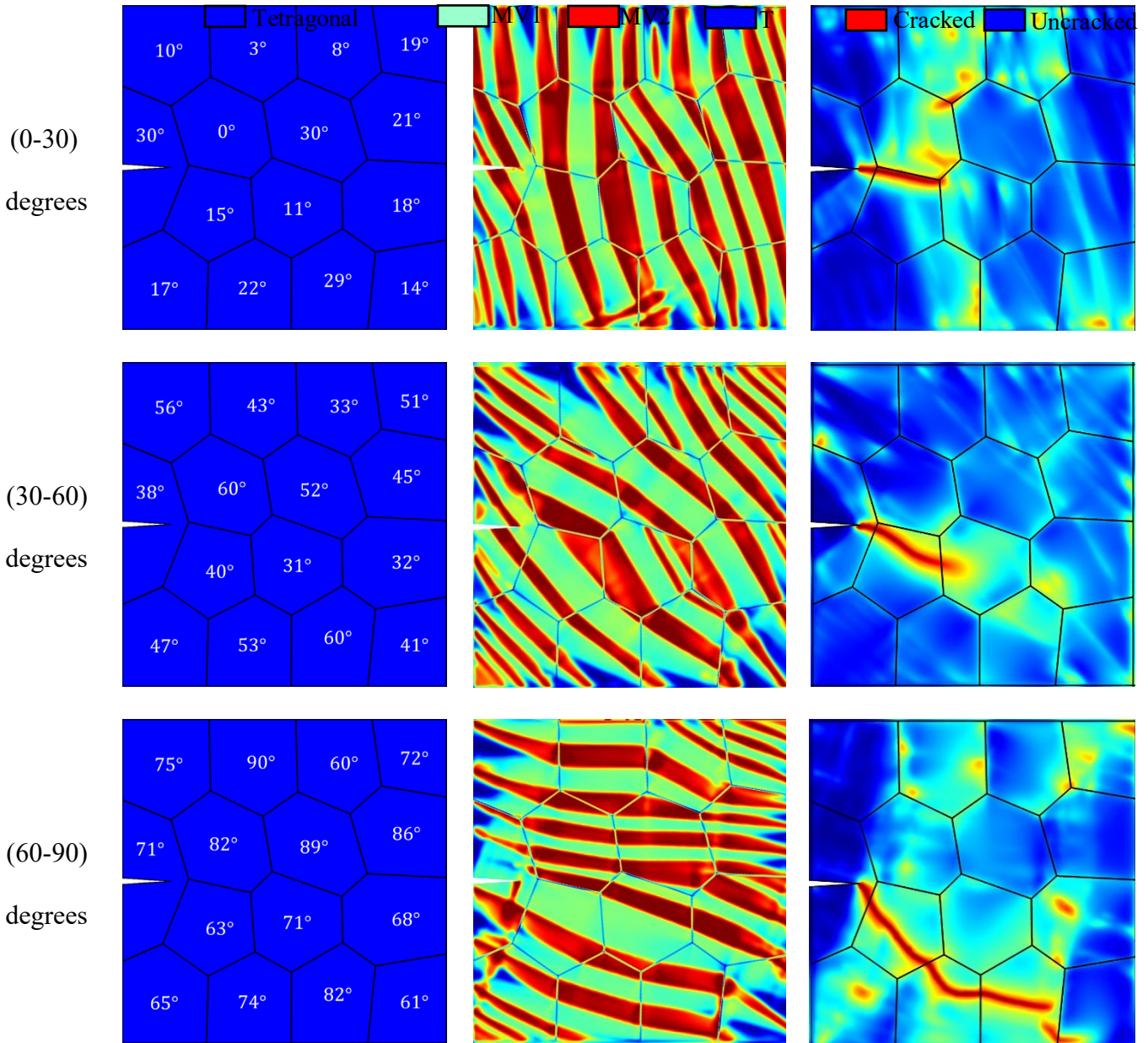
### **The Effects of Lattice Orientation**

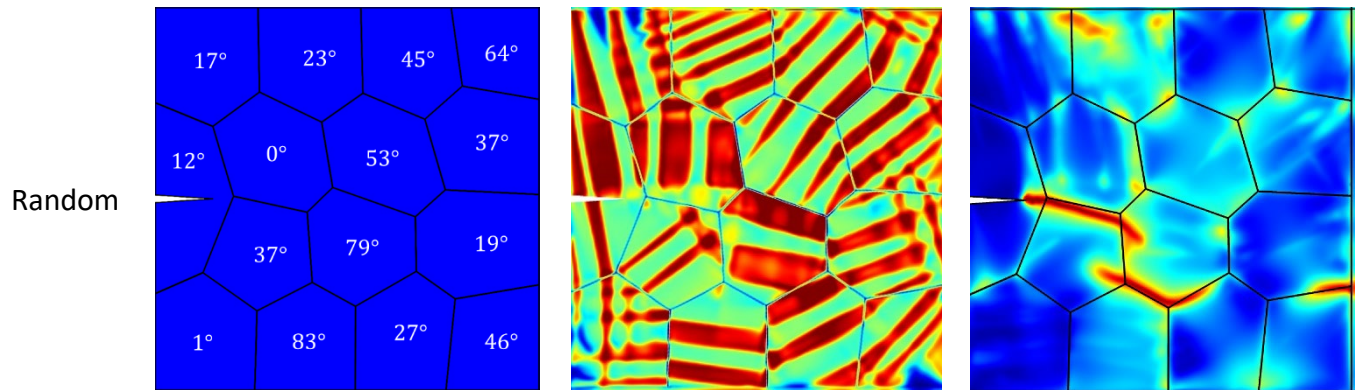
One way that we can develop more crack resistant SMCs is through engineering the microstructure texture. In this section, we study the effects of lattice orientation on crack growth in TPZ. Crystal lattice orientations, loadings, and boundary conditions have a dominant influence on MT microstructural patterning. Therefore, it is expected that the lattice orientation would have noticeable effects on the crack behavior in SMCs. We construct four models with four different lattice orientation patterns in a polycrystalline domain consisting of 15 grains. Three microstructures have lattice orientations confined in 0 – 30 degrees, 30 – 60 degrees, and 60 – 90 degrees, and the last microstructure has a random texture.

To have a better understanding of the effects of lattice orientation on the crack growth in TPZ, we present two sets of results. In the first set, we consider the fracture energy release rate at the grain boundaries equal to that of in the grains ( $R = G_{GB}/G_G = 1$ ). This case would represent transgranular crack growth behavior, which is dominant in zirconia doped ceramics such as yttria-stabilized zirconia. In the second set, we consider energy release rate at the grain boundaries to be 20% of the grains' fracture energy ( $R = G_{GB}/G_G = 0.2$ ). This case would represent intergranular fracture behavior, which is dominant in pure zirconia.

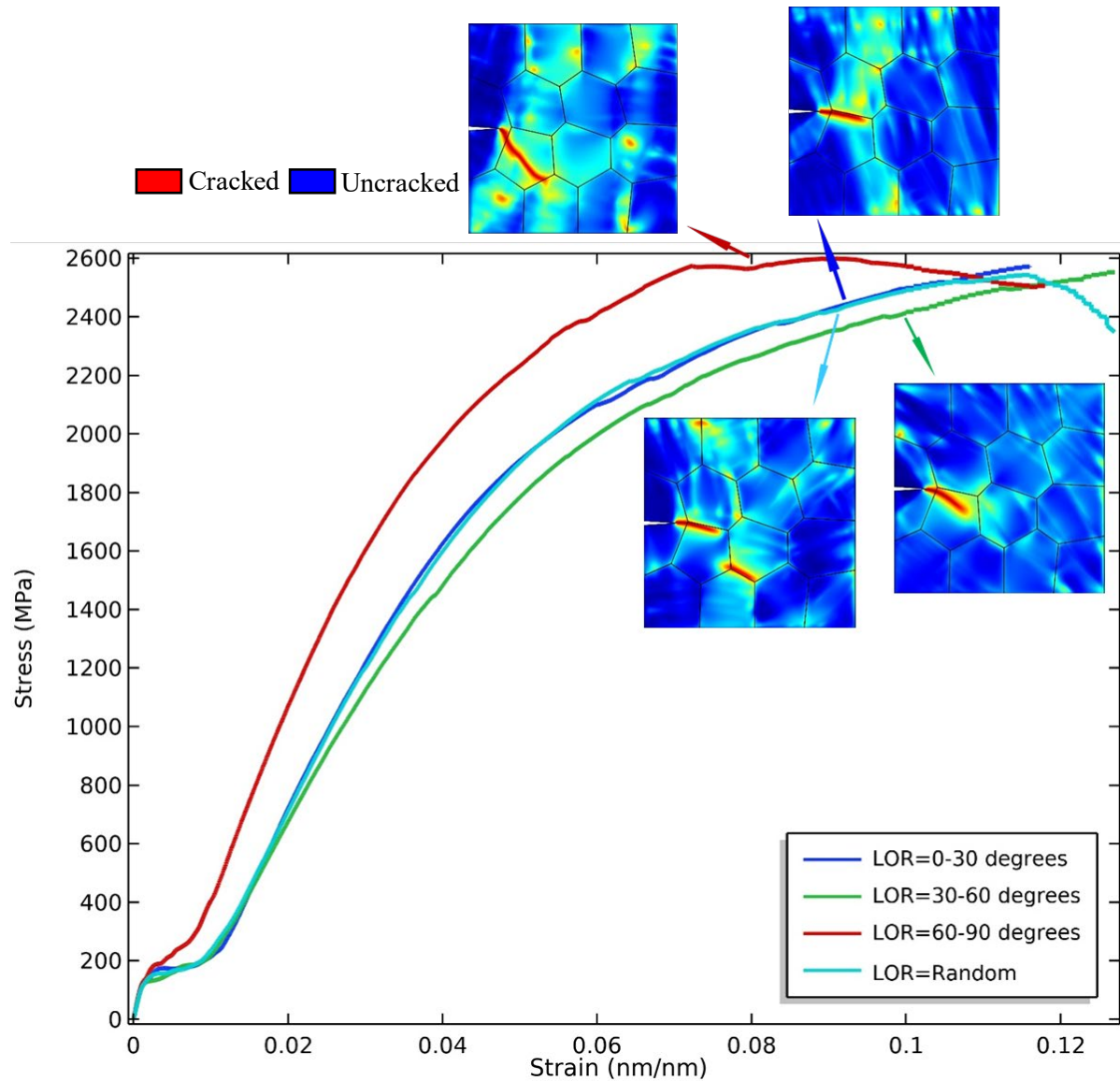
Figure 24 and Figure 26 show the microstructural patterning and the crack growth path for the four described textures for transgranular and intergranular fracture, respectively. In these models, the simulation begins at the entirely tetragonal state, like  $t = 0$  s in Figure 23. At  $t = 600$  s, for all lattice orientations, the majority of the tetragonal phase transforms into monoclinic. The monoclinic phase has  $(100)_m$  and  $(001)_m$  junction planes, the plane between two different martensite variants, that have been noted in many experimental investigations [7,8,27,91,92,94]. The model outcomes reveal that the crack propagation route and the crack size would alter notably by differing the crystal lattice orientation. These observations indicate that the crystal lattice orientation has a considerable impact not only on the crack propagation route but also on the efficacy of the transformation toughening for both transgranular and intergranular fracture.

Figure 24 and Figure 26 also reveal another critical effect of the lattice orientations on the TPZ. For both figures, each texture has its specific crack propagation path, which indicates that different lattice orientations may cause the primary crack to stop at some locations by closing the crack tip and reducing the stress at those spots. In such a situation, the crack has to propagate from the nearest location with the highest amount of stress. Since the internal stresses are governed by the local martensite microstructure and twin-twin interactions, the new crack initiation spot will be lattice orientation-dependent as it dramatically influences the microstructure.





**Figure 20.** The crystal lattice orientation effects on the Mode I transgranular crack propagation in TPZ. The first column shows the lattice orientation angle ranges for each grain. The second column is the microstructure at the onset of crack growth. The last column is the crack growth path and amount for each microstructure (all are at the same time, 3500 s). (MV1 = Monoclinic Variant 1, MV2 = Monoclinic Variant 2, T = Tetragonal).




**Figure 21.** The stress-strain curve for the Mode I transgranular fracture in tetragonal zirconia with different lattice orientation configuration. (LOR: lattice orientation;  $R = G_{GB}/G_G = 1$ ).

Figure 25 and Figure 27 demonstrate the stress-strain curves for the polycrystalline zirconia with four different lattice orientation configurations for transgranular and intergranular fracture, respectively. The graphs show that the cracks propagate more quickly in the microstructure with the grains' lattice orientations in the 60-90 degrees range. The reason for this behavior lies behind the fact that the grains with lattice orientation between 60-90 degrees produce the monoclinic variants with twin

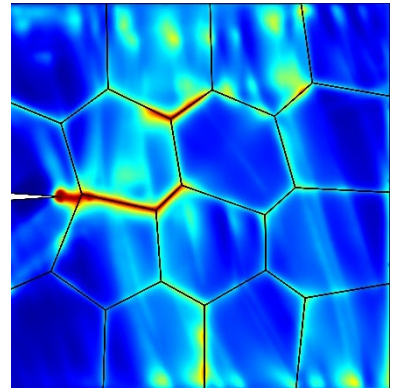
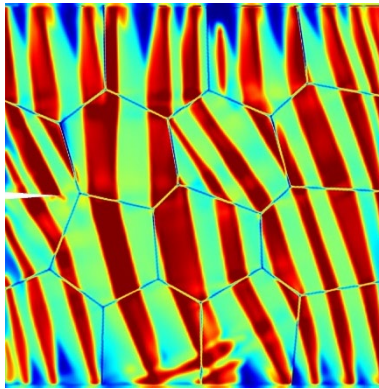
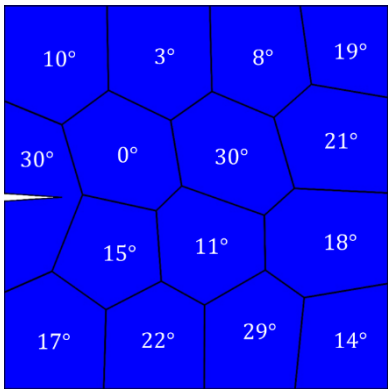
planes almost parallel to the initial crack plane. Therefore, the excess volumetric strain due to  $t \rightarrow m$  transformation releases in the planes parallel to the crack plane. However, in microstructures with lower angle grains, the majority of the excess strain is perpendicular to the crack plane and helps crack closure and eventually postponing the crack growth. The difference in the early stages of the stress-strain curves between the models with grains lattice orientation 60-90 degrees (red line) and the other models also shows that the released strain for red lines is not in the y-direction, i.e., perpendicular to the crack plane.

 Tetragona

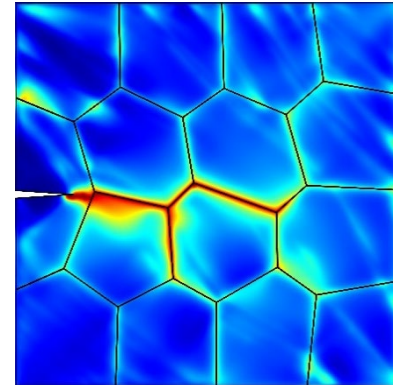
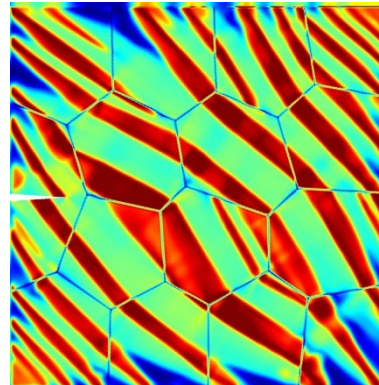
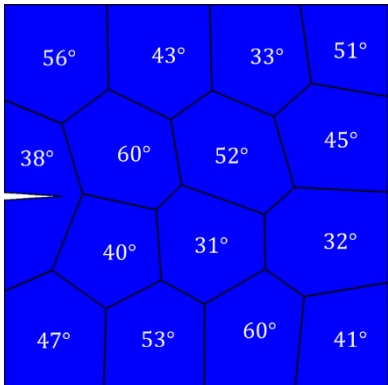
 MV1  MV2  T

 Cracked  Uncracked

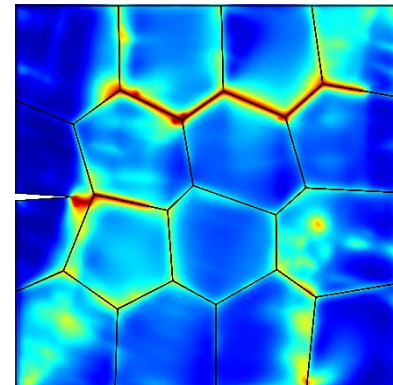
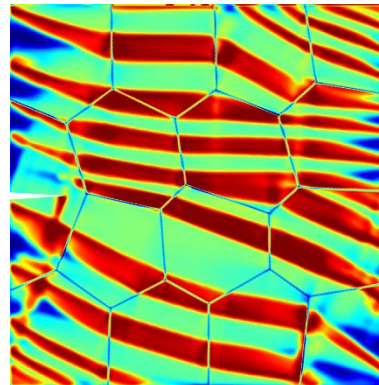
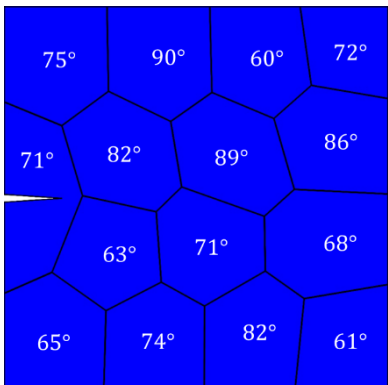
(0-30)  
degrees



(30-60)  
degrees



(60-90)  
degrees





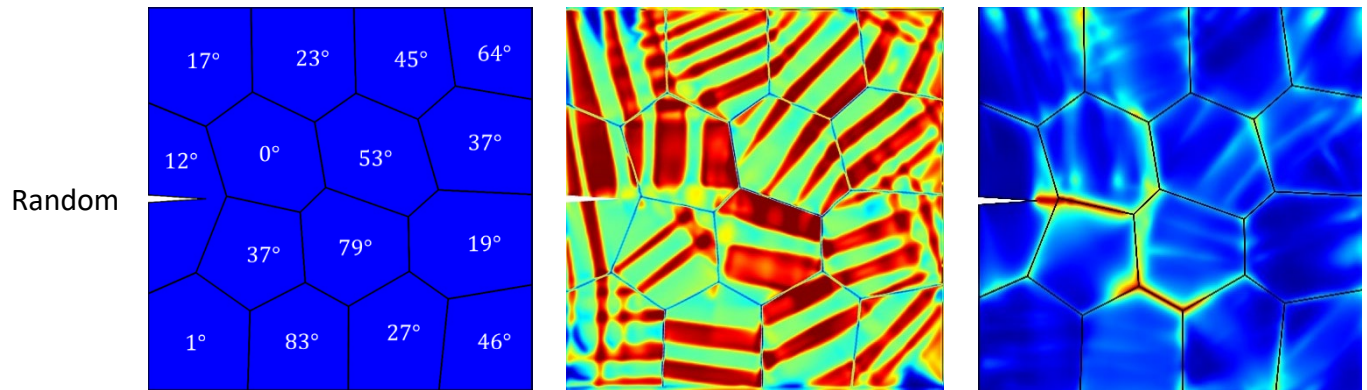


**Figure 22.** The crystal lattice orientation effects on the Mode I intergranular crack propagation in TPZ. The first column shows the lattice orientation angle ranges of each microstructure. The second column is the microstructure at the onset of crack growth. The last column is the crack growth path and amount for each microstructure (all are at the same time, 3500 s). (MV1 = Monoclinic Variant 1, MV2 = Monoclinic Variant 2, T = Tetragonal).

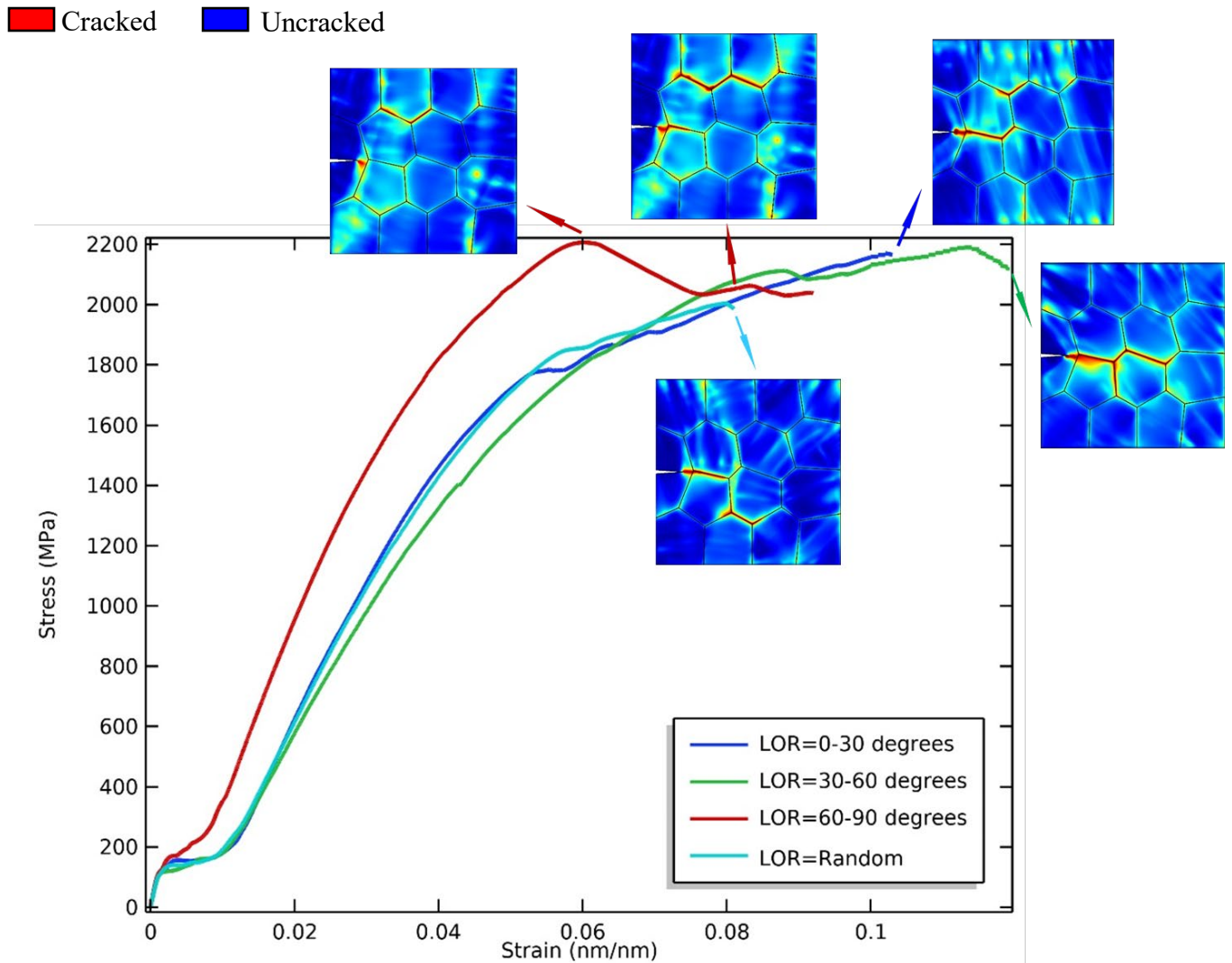


**Figure 23.** The stress-strain curve for the Mode I intergranular fracture in tetragonal zirconia with different lattice orientation configurations. (LOR: lattice orientation;  $R = 0.2$ ). Microstructures with low angle grains show higher resistance to crack growth. See Figure 4 for angle interpretation.

### The Effects of The Grain Size on The Fracture of Polycrystalline Zirconia

Besides texture engineering, grain boundary engineering is also another technique for developing materials with superior properties. In this section, we investigate the effects of grain size on the toughening and fracture of TPZ.

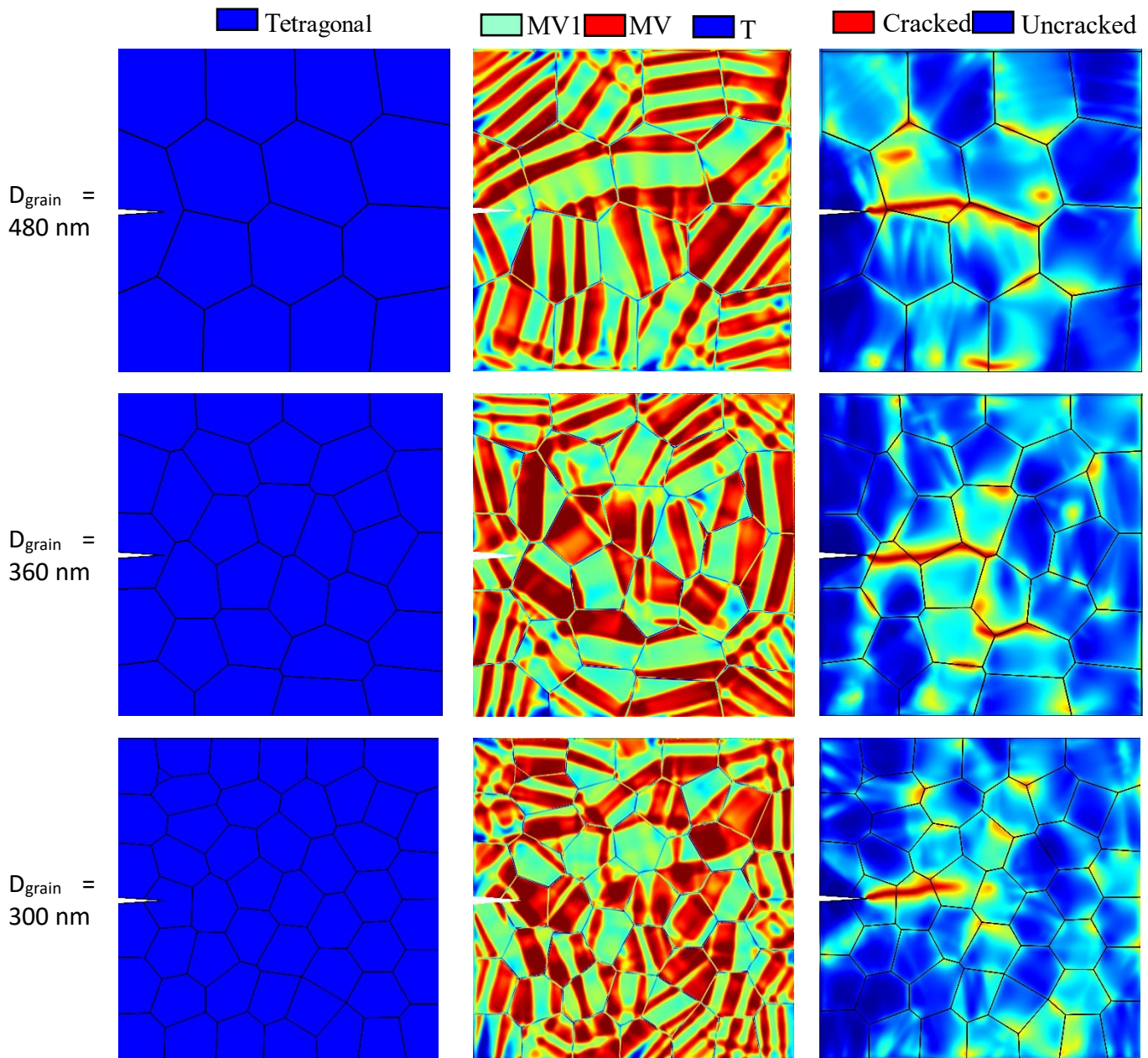
Generally, toughness trend for most materials is inversely related to the grain size, i.e., grain size reduction leads to fracture toughness improvement. However, this is not the case for zirconia because while the grain size reduction makes crack growth harder, it will suppress the MT and its associated transformation toughening [103]. To study these two antagonistic effects, we have modeled the crack growth in polycrystalline zirconia with four different microstructures with average grain sizes of 480, 360, 300, and 200 nm.

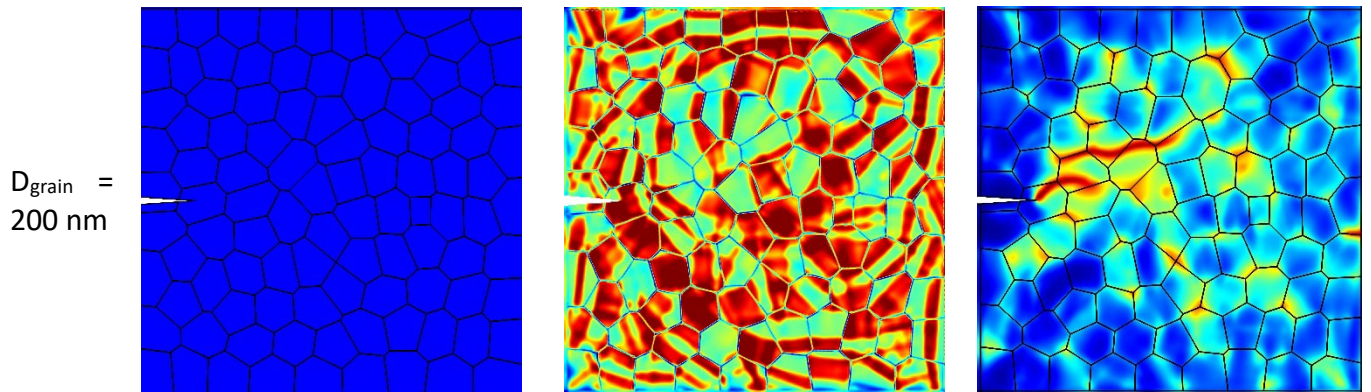
Since most experimental data on zirconia fracture is for yttria-stabilized zirconia and Kumar et al. [71] reported transgranular fracture for yttria-stabilized zirconia, we study the transgranular fracture in this section. Additionally, the Young's modulus at the grain boundaries is chosen to be 85 percent of the grain [69].

Figure 28 shows the crack propagation pattern and amount as well as the microstructural evolution of the monoclinic phase in different time steps for the polycrystalline zirconia with varying average grain size. For more quantitative comparison, the stress-strain curves are also shown in Figure 29. From these two plots, we see that the model with the biggest grain size, 480 nm, shows the weakest crack growth resistance. Fracture toughness increases by decreasing grain size from 480 to 360 and 300 nm. However, the fracture toughness decreases when grain size drops from 300 nm to 200 nm. These results indicate that for zirconia, there is an optimum grain size, which leads to the maximum fracture toughness, in this study 300 nm.

Similar trends were observed in the experimental studies. Eichler et al. [104] studied the effects of grain size on fracture toughness of TPZ doped with 2 mol% yttria (2Y-TPZ) in specimens with average grain sizes between 150 to 900 nm. Their study

explicates that the toughening was improved by increasing the grain size from 150 nm to 300 nm then decreased in the sample with 500 nm grain size. Eichler et al., in another study [103], found that the critical grain size for maximum toughening in 3Y-TPZ was 380 nm.





**Figure 24.** The effects of grain size on the crack propagation in TPZ. The first column is the crack propagation in each microstructure at  $t = 3500 \text{ s}$ . The second column depicts the microstructure at the onset of the crack growth,  $t = 600 \text{ s}$ . The last column is the crack growth pattern at  $t = 3500 \text{ s}$  along with the corresponding microstructure. (MV1 = Monoclinic Variant 1, MV2 = Monoclinic Variant 2, T = Tetragonal).

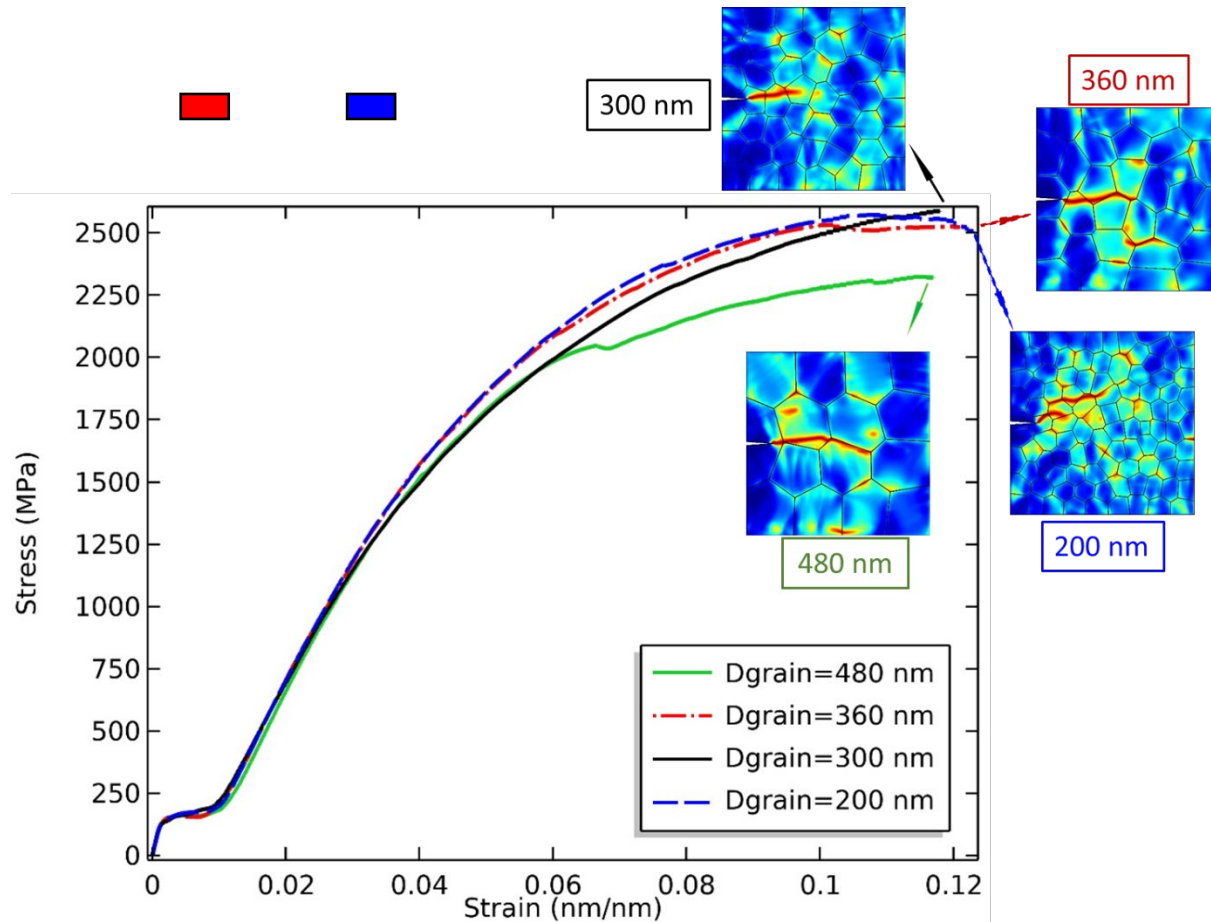


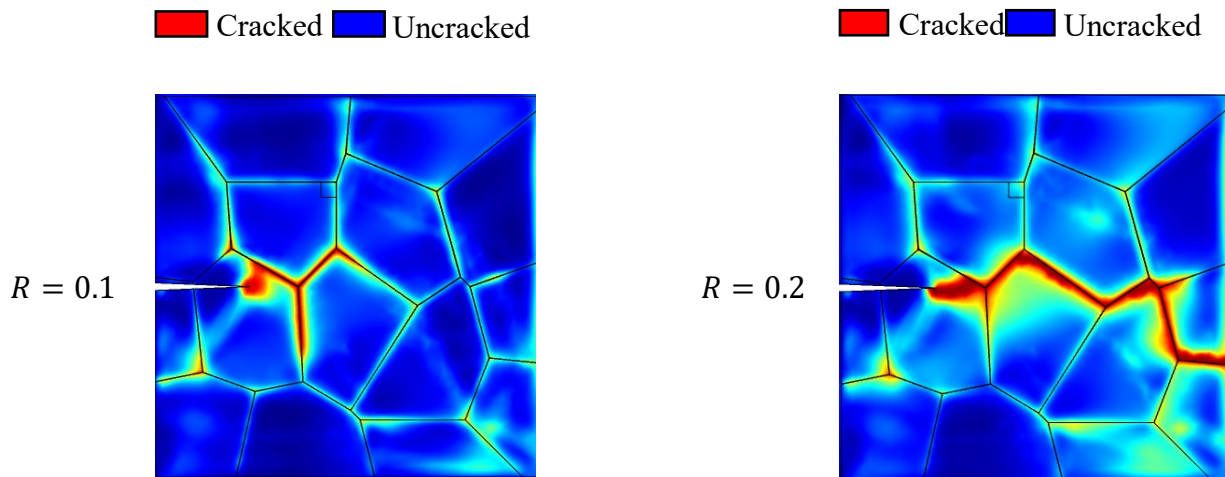
**Figure 25. The stress-strain curve for the transgranular crack propagation in the TPZ with different average grain sizes (Dgrain).**

### The Effects of Grain Boundaries Strength

As it was noted in the previous section, experimental studies have shown that pure zirconia has an intergranular fracture behavior [24,71], while the yttria-stabilized zirconia and aluminum toughened zirconia tends to have a transgranular fracture [24,71]. In this section, we investigate the effects of the fracture energy at the grain boundaries on the crack propagation patterning, which shows the model capability in predicting both transgranular and intergranular fractures in polycrystalline materials.

In order to have a better understanding of the influence of the fracture energy at grain boundaries compared to that of inside the grain, we use a parameter which is called

fracture energy ratio. Fracture energy ratio is the ratio of the grain boundary fracture energy to the fracture energy inside the grains,  $\frac{G_{GB}}{G_G} = R$ . By changing this ratio, it would be possible for our model to show how the fracture patterns tend to change their paths. Our simulations show that  $R = 0.2$  would be an appropriate choice for intergranular crack growth since several simulations with wide ranges of grains' lattice orientations showed intergranular crack growth. However, when  $R$  starts to rise from 0.2 to 0.3, the crack tends to get away from the grain boundaries. When  $R$  increase to over 0.4, the crack path is transgranular with a majority of the area perpendicular to the tensile load direction no matter if it is in the middle of the grain or it is at the grain boundary. In this work, since we study the Mode I fracture, the typical path is straight. Therefore, the crack tends to grow straight. Figure 30 depicts the role of the fracture energy ratio on the crack propagation path.



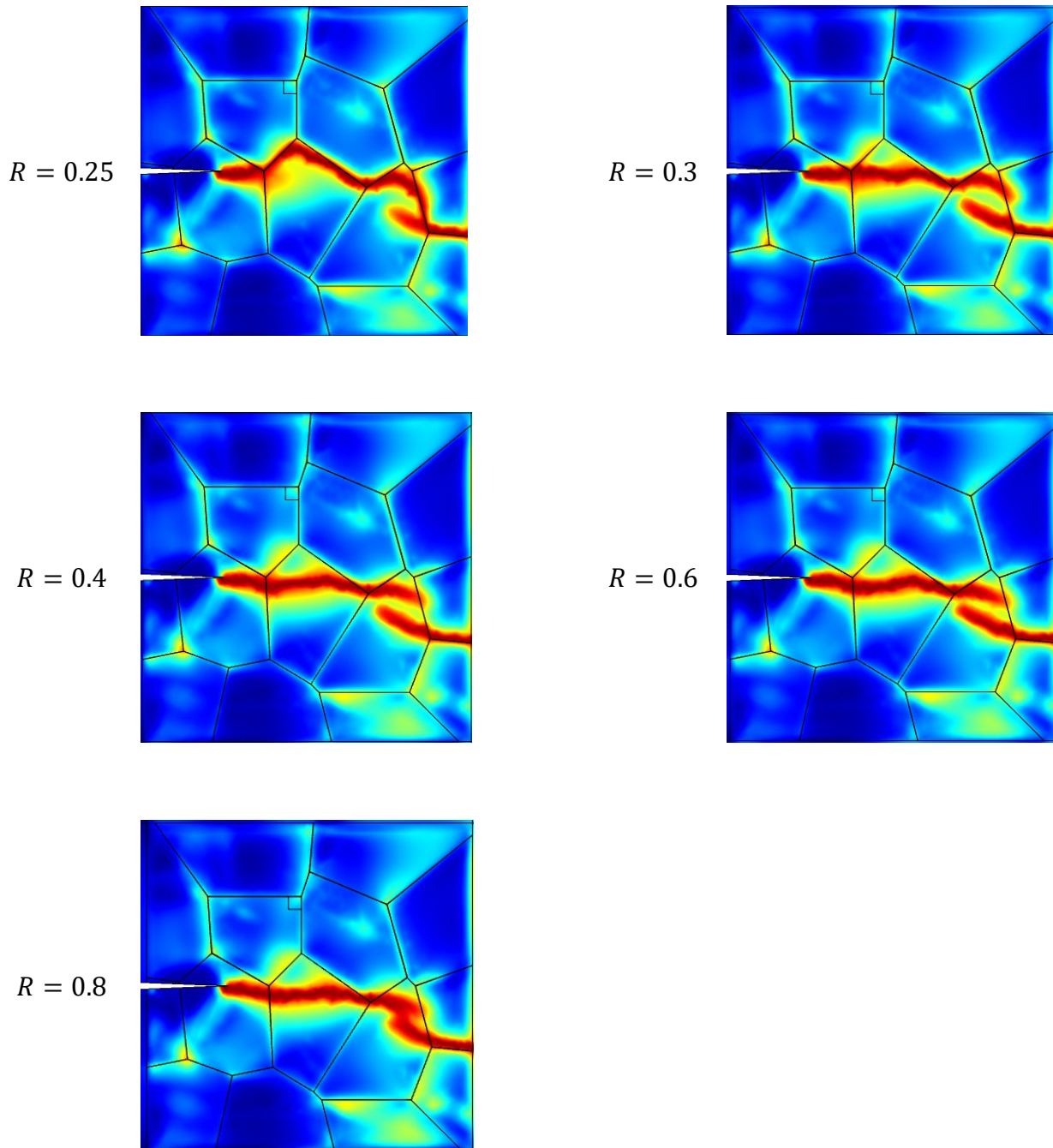


**Figure 26.** The fracture propagation path in TPZ with different fracture energy ratio ( $R$ ), the ratio of grain boundary fracture energy to the fracture energy inside the grains. The crack tends to depart from the grain boundaries when the ratio increases.



## Conclusion

In this chapter, we developed a multiphysics/multiphase phase-field model for crack growth in polycrystalline shape memory ceramics and parameterized it for zirconia. The model captures the three main forms of fracture mechanisms in polycrystalline zirconia, including the secondary crack initiation and growth ahead of the primary crack, crack branching, and grain boundary bridging. We employed an appropriate algorithm for generating polycrystalline geometry, which makes it feasible to implement models with different morphologies, grain sizes, and grain boundary sizes. The model shows that the texture and grain boundary engineering can be effectively used to design polycrystalline zirconia with enhanced fracture toughness. Texturing the grains to form low angles between  $a_t$  ( $a$ -axis in tetragonal) and the crack plane increases the fracture toughness. The competition between the fracture toughness improvement and the martensitic transformation suppression due to grain size reduction creates a scenario in which the maximum fracture toughness happens in an optimum grain size.

## CHAPTER FIVE: THREE-DIMENSIONAL MODEL

In this chapter, we parametrize the model for 3D single crystal zirconia. All 12 monoclinic variants are considered in the model. This study would enable us to have a more realistic understanding of the MT and crack growth's concurrent evolution in shape memory ceramics.

The result provided in this chapter is submitted as a research paper in the International Journal of Mechanical Sciences (March 2021) [105].

### **Crystallography of Tetragonal to Monoclinic Transformation in Zirconia**

Monoclinic variants that are derived from tetragonal are categorized into three main correspondences, namely correspondence *A*, *B*, and *C*. These correspondences are defined based on the monoclinic axis that is derived from the  $c_t$  (axis *c* in tetragonal). For example, correspondence *A* indicates that  $c_t$  becomes  $a_m$  (axis *a* in monoclinic). However, we need a more comprehensive notation as in the case of correspondence *A*,  $a_t$  and  $b_t$  to have this chance to become either  $b_m$  or  $c_m$ . Therefore, in this study, we use the Hayakawa et al. [106–108] notation system to identify all monoclinic variants. This notation technique uses a three-letter-sign for each monoclinic variant. If we consider  $a_t$ ,  $b_t$  and  $c_t$  as the tetragonal axes and  $a_m$ ,  $b_m$  and  $c_m$  as the monoclinic axes, the three letters in Hayakawa's notation, from left to right, show which monoclinic axes are derived from  $a_t$ ,  $b_t$ , and  $c_t$ . For instance, the *BCA* variant indicates that  $b_m$  is derived from  $a_t$ ,  $c_m$  is derived from  $b_t$ , and  $a_m$  is derived from  $c_t$ . The angles between  $a_m$  and  $c_m$  in the monoclinic phase is about  $99^\circ$  [8]. Therefore, there are two possible

orientations for each monoclinic variant, *OR1*, and *OR2*. *OR1* (*OR2*) indicates that  $a_m$  ( $c_m$ ) is aligned with its correspondent axis in tetragonal and  $c_m$  ( $a_m$ ) is tilted. Figure 31 demonstrates four possible monoclinic variants of the correspondence *C*.

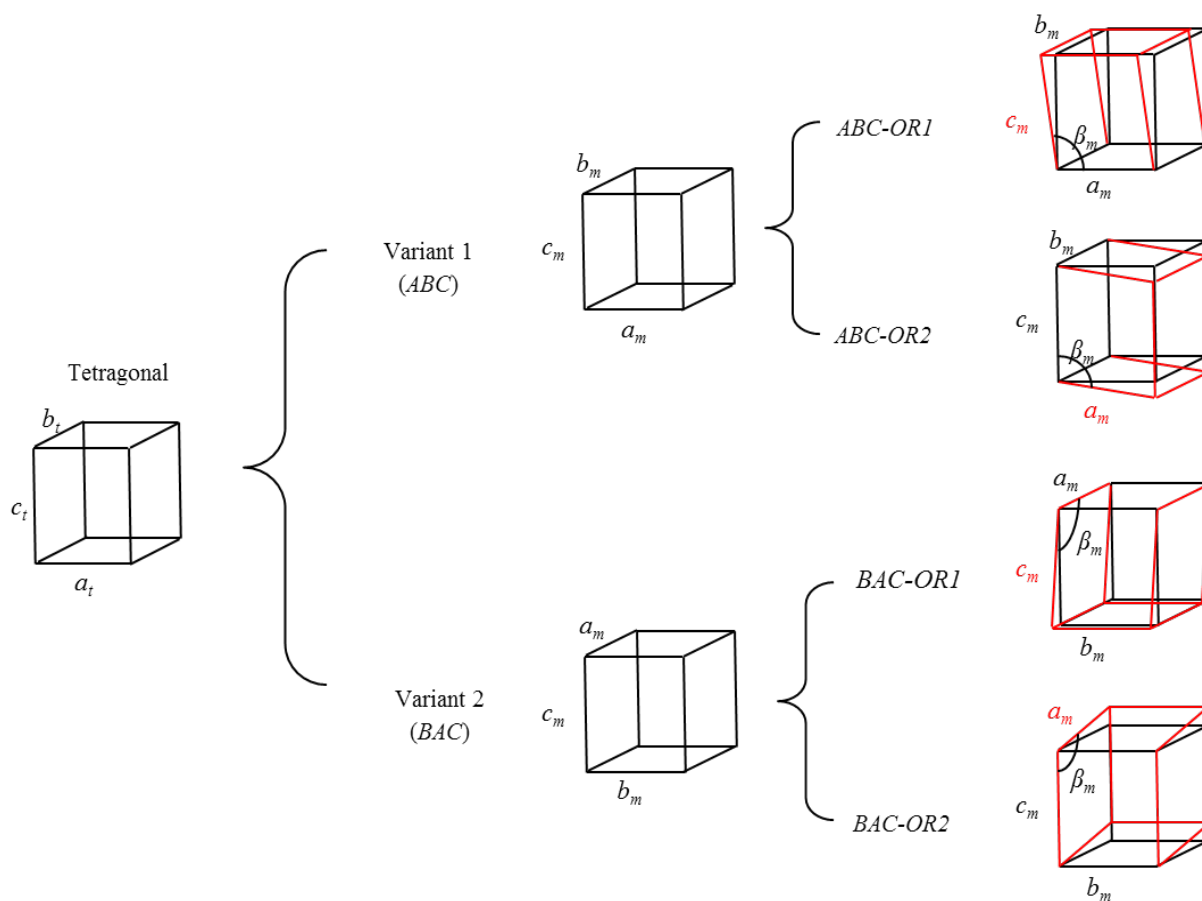


**Figure 27.** Schematic representation of possible monoclinic variants derived from the correspondence *C*, i.e.,  $c_t$  become  $c_m$  [76].

In the  $t \rightarrow m$  transformation, the incorporation of orientations, variants, and correspondences leads to 12 feasible monoclinic crystals for each tetragonal crystal. Figure 32 shows the monoclinic correspondences, orientations, variants, and their self-accommodating variants in  $t \rightarrow m$  transformation.

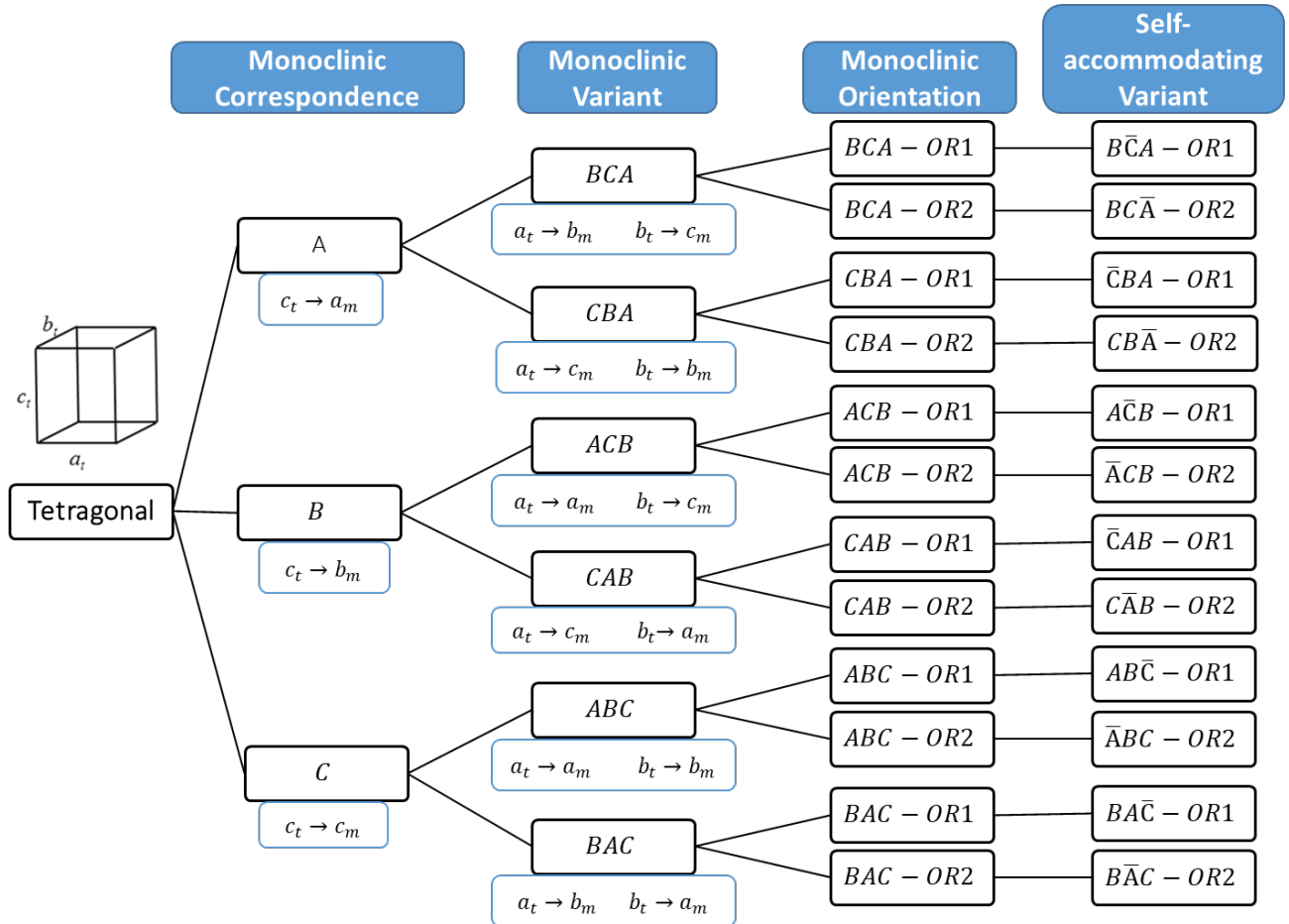


**Figure 28.** The feasible monoclinic variants and their self-accommodating variants in  $t \rightarrow m$  transformation [76].

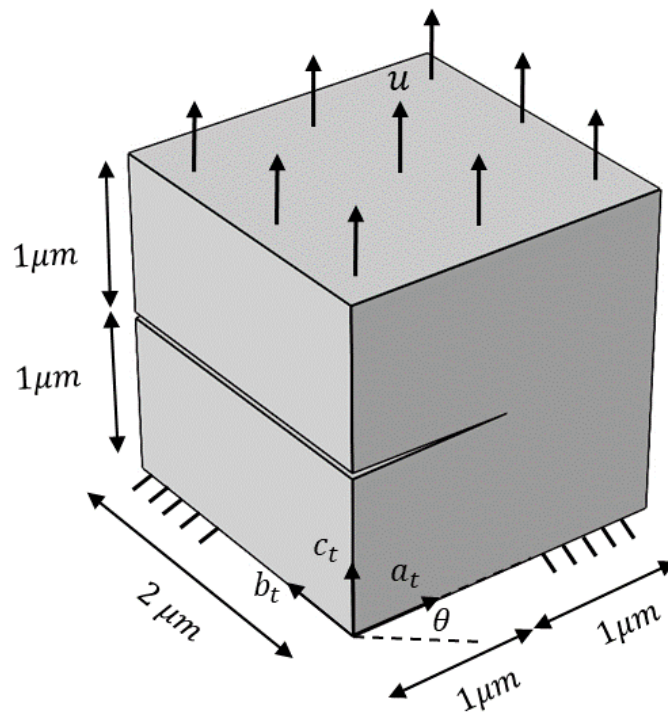
### Results

In this section, we model the 3D single crystal zirconia fracture in a cube with a length of  $2 \mu m$ . The cube has an initial crack and a monotonic increasing displacement load,  $\Delta u = 1 \frac{nm}{s}$ , has been applied at the upper surface, and the bottom boundary is clamped. A fine mesh has been applied. The geometry and boundary conditions are depicted in Figure 33.

The numerical parameters that are used in this model are provided in Table 7.

**Table 7. Parameters applied in the model.**

Temperature (K)	1170
A (N/m <sup>2</sup> ) [49]	$2.5 \times 10^6$
Chemical driving force, ( $J \cdot mol^{-1}$ ) [49]	800 ( $36.8 \times 10^6 J \cdot m^{-3}$ )
Gradient energy coefficient, $\beta$ ( $J \cdot m^{-1}$ ) [49]	$2.5 \times 10^{-9}$
Kinetic coefficient, $L$ ( $m^3 \cdot J^{-1} \cdot s^{-1}$ )	$2 \times 10^{-9}$
Critical energy release rate, $G_c$ ( $J \cdot m^{-2}$ ) [69]	4.33
Crack elasticity modification parameter, $k$	$1 \times 10^{-9}$
The length parameter, $l_0$ (nm)	20

**Figure 29. The boundary conditions and geometry of a cube with an initial crack.**

## Model Verification

We validate the proposed model by comparing the results with the experiments. Figure 34 shows a comparison between the PF model results and an Atomic Force Microscopy (AFM) micrograph of the surface relief obtained from the martensitic  $t \rightarrow m$  transformation in ceria-stabilized zirconia [109]. The high resolution AFM experiments of Deville et al. [109] make it feasible to follow and capture the transition-induced relief at the surface precisely. AFM observations at the crack zone in Figure 34 show self-accommodated martensite pairs development in the vicinity of crack areas with arrows indicating such pairs' junction planes. As in Deville et al.'s [109] experimental observations, transformed variants are distinctly visible when  $c_t$  axis of the grain is almost perpendicular to the surface. We adopt the same orientation for the single crystal in this simulation and the results depict similar morphologies for the monoclinic variants. Figure 34-a shows the crack pattern and the microstructure of the transformed domain from the simulation. Four different martensitic variants emerged from the simulation, namely  $ABC$ ,  $ABC\bar{}$ ,  $BAC$  and  $BAC\bar{}$ . Figure 34-b shows the surrounding of a propagated crack in ceria-stabilized zirconia, which depicts the martensitic variants in the transformed zone. A magnified frame of the crack zone, illustrated in Figure 34-c, shows the primary and secondary junction planes of the martensitic variants.

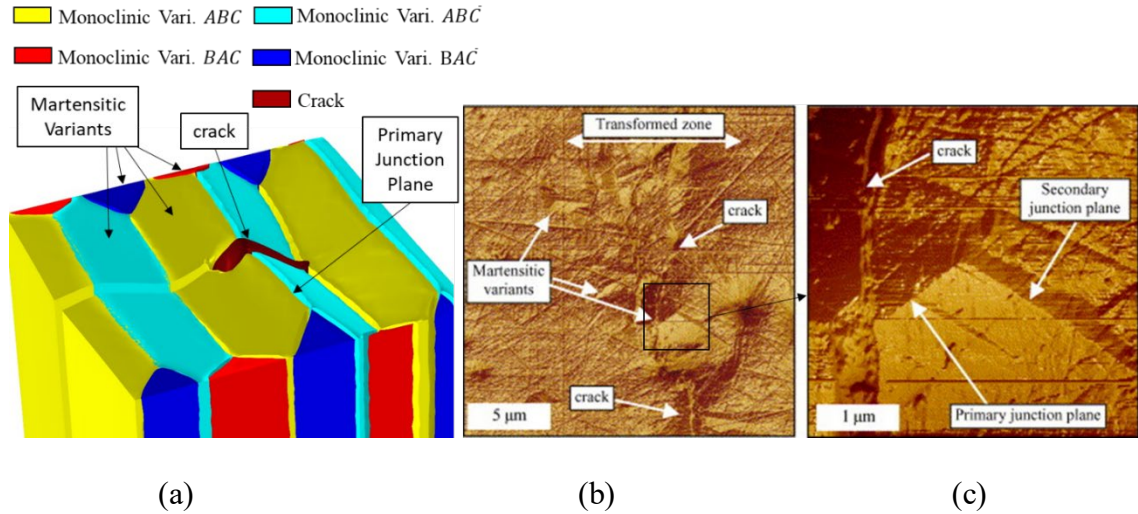


**Figure 30. PF model simulation result for martensitic transformation and crack propagation in a 3D single crystal zirconia (a) and comparison with the experiment (b) (c) [109].**

The detailed investigation of Deville et al. [109] on transformation-induced relief leads to brand-new knowledge regarding the toughening mechanism order. Deville et al. [109] reported the fragmentation of the transformed zones caused by the crack growth. This observation indicates to the domain phase transition before the crack arrival. Phase field simulation also shows a similar observation, Figure 35. The reason behind this phenomenon is the fact that the stress state around the crack tip is increasing due to loading, and this stress can trigger the phase transformation, which absorbs some of the stress that otherwise would be available for crack growth. In the case of increasing the stress further, it leads to crack propagation in the transformed areas. Figure 35-c shows a propagated crack in ceria-stabilized zirconia. The crack propagated throughout the transformed grain and fragmented it. In this particular case, i.e.  $c_t$  is perpendicular to the top surface, we have a transformation strain that is accommodated vertically, so there is no residual stress in the domain, and it is possible for the crack to run through the transformed grain rather than passing alongside. Figure 35-a shows that the crack has

started to grow while there are martensitic transformed variants in the domain, and the crack is passing through them. Figure 35-b shows that the crack propagated more and breaks the transformed plane.

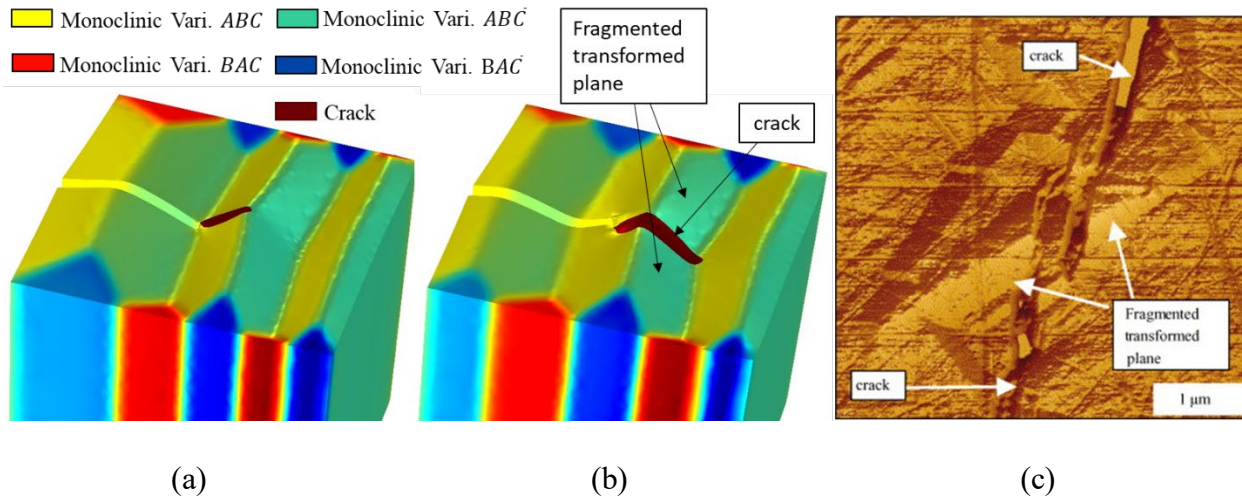


**Figure 31. Observation of the fragmented transformed plane in both simulation (a)-(b) and experiment, AFM (c) [109].**

### Temporal and Spatial Evolution of Crack Propagation in Transformable Domains

In this section, we have considered the coupled PF model to investigate the crack growth, mode I, in a 3D tetragonal single crystal zirconia. In this part, we picked zero degrees, i.e.,  $\theta = 0^\circ$ , in Figure 33 for the lattice orientation angle. The results show the importance of the phase transformation on the crack growth as well as toughening.

Figure 36 depicts the co-evolution of  $t \rightarrow m$  transformation and crack propagation in a 3D domain. The domain is fully tetragonal in the beginning. As the external loading is applied on the upper surface, the stress escalates at the crack tip and promotes the  $t \rightarrow m$  transformation. As predicted from our simulation results and observed in the experimental studies, the phase transformation originates from the crack tip. The transition process



proceeds by raising the displacement loading until the monoclinic phase dominates the crystal body.

Although there are 12 possible monoclinic variants in 3D, experimental studies have observed some of them more frequently. According to empirical and theoretical studies [90–92], correspondence  $C$  is the predominant direction for the transformation because of its relatively smaller strain energy than the other correspondences, i.e.,  $A$  and  $B$ . The equations and model parameters are set in a way to consider all 12 monoclinic variants without any preferences or differences in their emergence chance and development. Nevertheless, only a few of them will show up in the final microstructure, which will be chosen by innate minimum formation energy principles.

For the current simulation set, i.e., the lattice orientation angle is zero degrees,  $\theta = 0^\circ$ , only the monoclinic variants of  $ABC$  and  $ABC\bar{C}$  from the correspondence  $C$  show up in the microstructure, and the other variants do not appear while they have similar initial chances. After nucleation of favorable variants in the early stages of the phase transition, the variants rearrange and grow in a way to accommodate the highest possible amount of strain. When the monoclinic phase becomes dominant in the crystal, the crack propagates in its straight expected direction, as it is a mode I crack growth model. Since the model has the displacement loading normal to the upper boundary, which is the direction of  $c_t$  in this simulation, the correspondence  $C$  is expected to form and eventually change the microstructure until the whole upper crack part alters to the single monoclinic variant. This phenomenon agrees with the experimental and theoretical studies that observed the development of different martensitic variants in favor of the loading conditions [23,93].

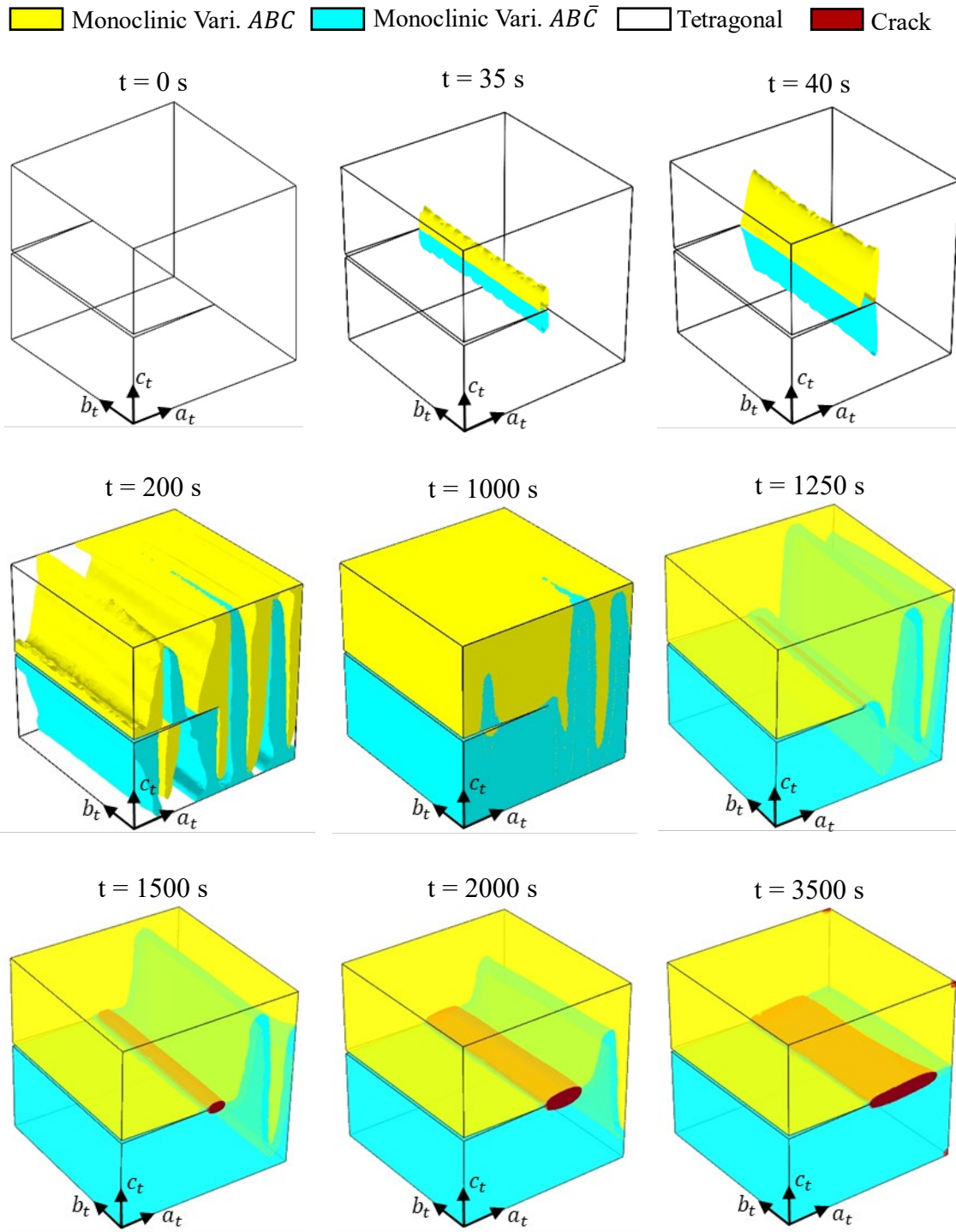


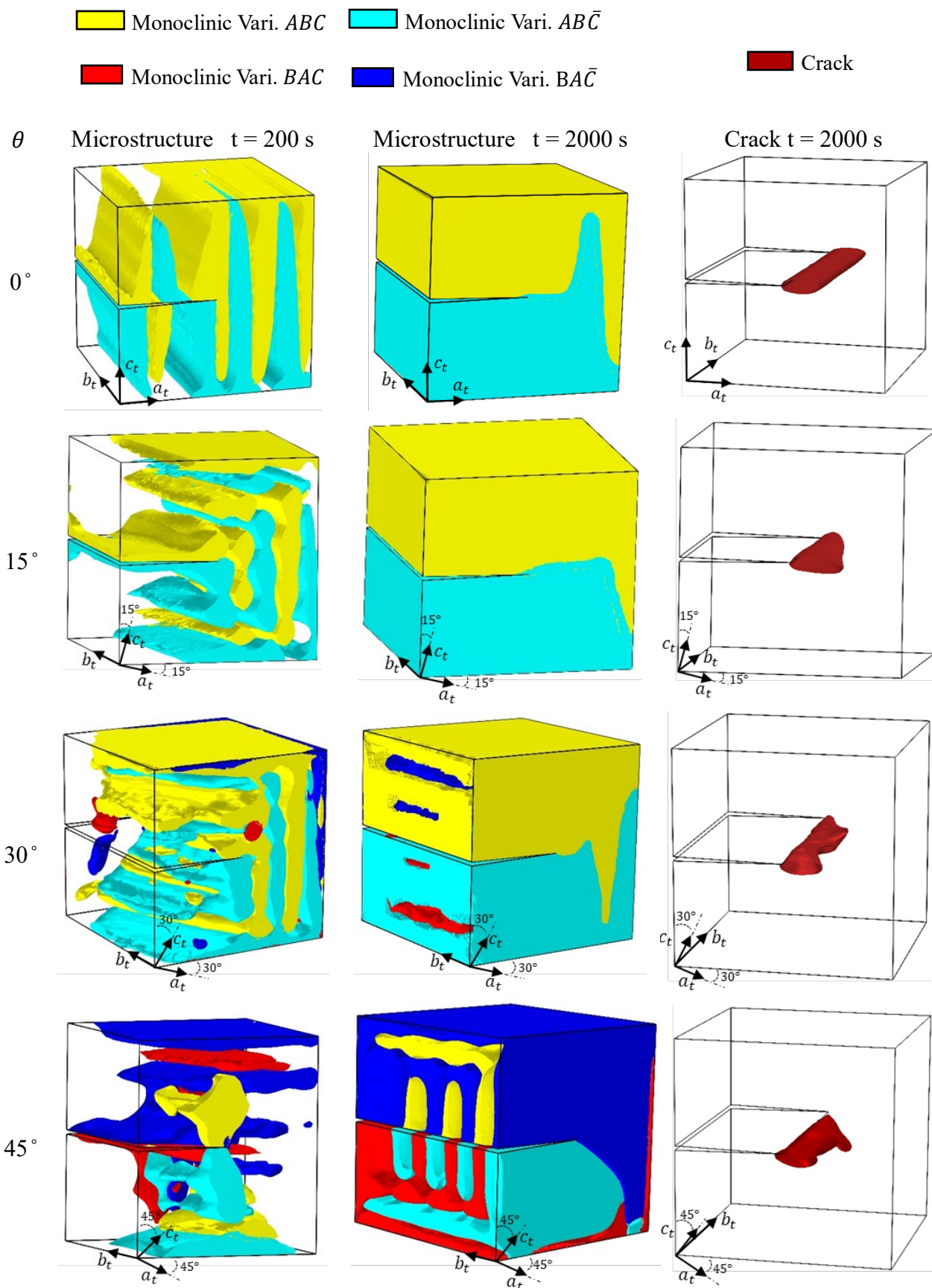
**Figure 32.** The concurrent evolution of  $t \rightarrow m$  transformation and monoclinic variants reorientation with crack propagation in 3D single crystal zirconia in isosurface ( $\eta = 0.5$ ). (Vacant domain is tetragonal, yellow is monoclinic variant  $ABC$ , cyan is monoclinic variant  $ABC\bar{C}$ , and brown is crack)

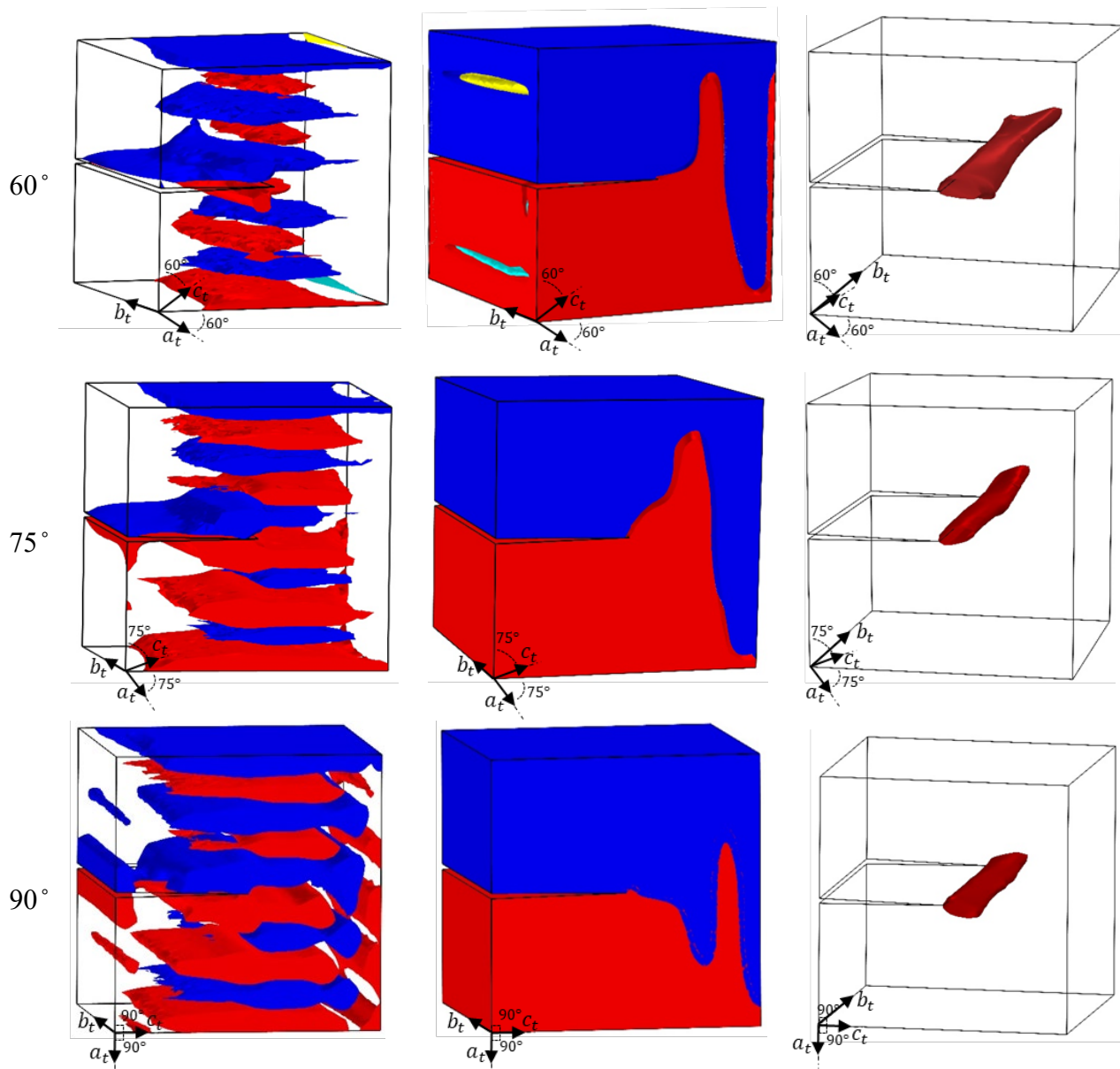
### The Effects of Crystal Lattice Orientation

To gain more profound knowledge on how the lattice orientation would affect the monoclinic variants formation and crack growth pattern and toughening, we have studied a set of simulations for crack growth in a 3D single crystal zirconia for different lattice orientations (LORs) in the  $a_t$ - $c_t$  plane, i.e., the rotation angle is around the  $b_t$ -axis.

Figure 37 depicts the microstructure at  $t = 200$  s and  $2000$  s and the crack pattern at  $t = 2000$  s for the lattice orientations of  $0^\circ$ ,  $15^\circ$ ,  $30^\circ$ ,  $45^\circ$ ,  $60^\circ$ ,  $75^\circ$ , and  $90^\circ$ . The results show that the initial emerging and final monoclinic variants are different for different lattice orientations. For instance, in the model with LOR  $0^\circ$  and  $15^\circ$ , only monoclinic variants of  $ABC$  and  $ABC\bar{C}$  form. However, the arrangement of these variants are different in LOR  $0^\circ$  and  $15^\circ$ ; the dominant twin plane for LOR  $0^\circ$  is  $(100)_m$  plane, while for LOR  $15^\circ$ , we see both  $(100)_m$  and  $(001)_m$  planes. For LOR  $0^\circ$ , the crack grows evenly through the thickness while it is not even for LOR  $15^\circ$ . For  $30^\circ$ ,  $45^\circ$ , and  $60^\circ$  we observe the formation of four monoclinic variants, i.e.,  $ABC$ ,  $ABC\bar{C}$ ,  $BAC$  and  $BAC\bar{C}$ . The presence of  $ABC$  and  $ABC\bar{C}$  variants are more dominant for LOR  $30^\circ$  while the dominancy changes to  $BAC$  and  $BAC\bar{C}$  variants for LOR  $60^\circ$ . For LOR  $75^\circ$  and  $90^\circ$  only variants  $BAC$  and  $BAC\bar{C}$  form. The results reveal the profound influence of the lattice orientation on both microstructure and crack growth. As the lattice orientation changes, the configuration and the type of the monoclinic variants alter, affecting the crack pattern and crack propagation amount or toughness. For instance, in the model with LOR  $0^\circ$ , the crack grows in a straight path and even throughout the thickness, because the displacement loading is in the  $c_t$  direction and the  $ABC$  and  $ABC\bar{C}$  monoclinic variants emerge symmetrically, whereas, in the model with LOR  $15^\circ$ , the crack is not even within the

thickness because of the uneven microstructure formation that leads to the different stress states at various spots.

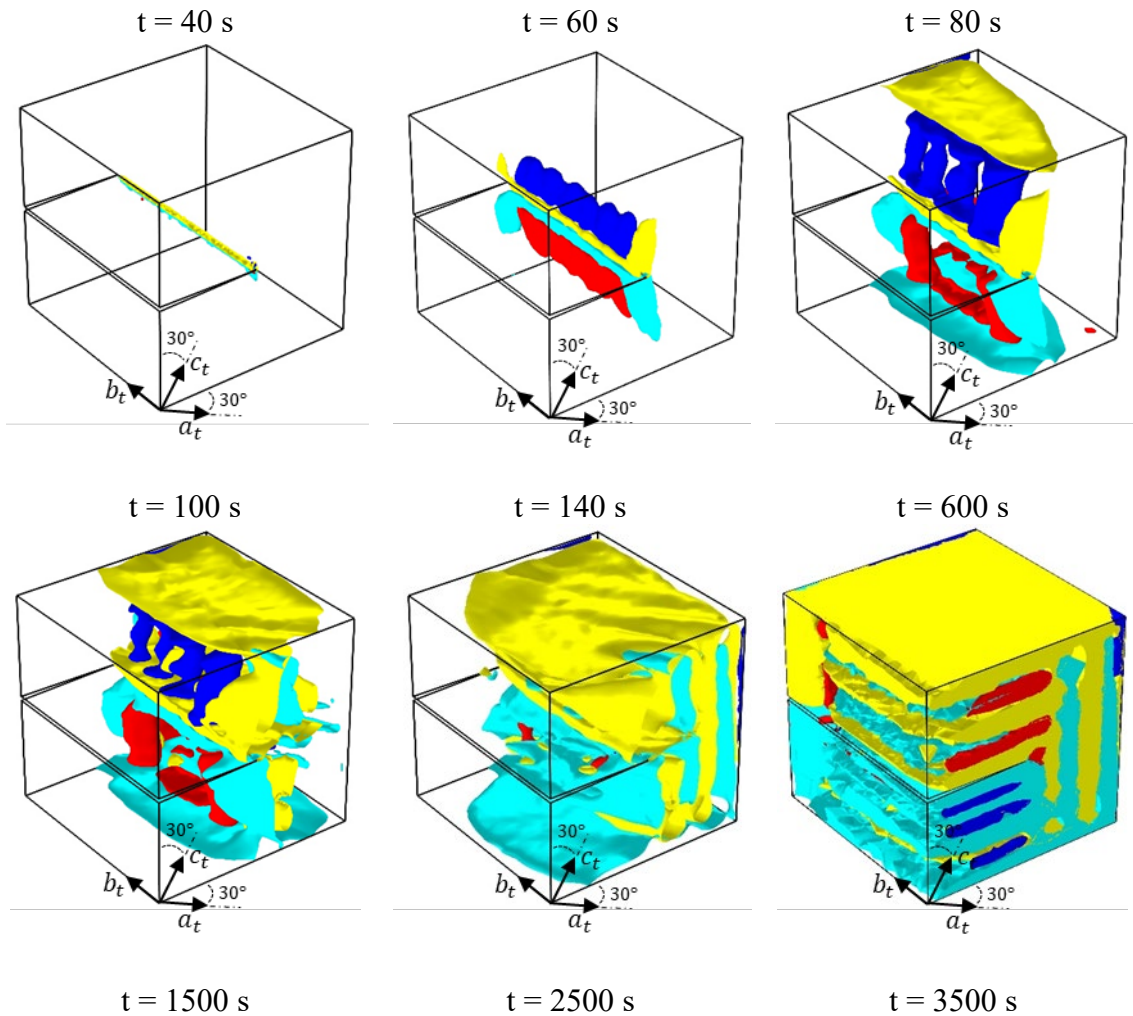
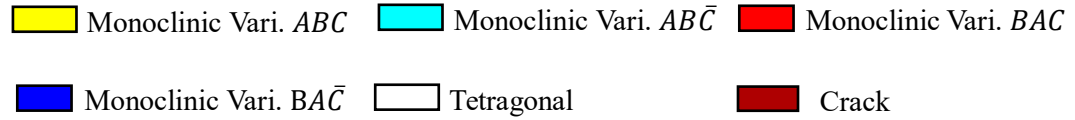




**Figure 33.** Microstructure and crack pattern in 3D single crystal zirconia with different lattice orientations. The first column shows the microstructure at  $t = 200$  s, the second column shows the microstructure at  $t = 2000$  s, and the last column shows the crack pattern at  $t = 2000$  s.

To elaborate the concurrent evolution of crack and  $t \rightarrow m$  transformation for the cases that the crack propagation deviates from the even growth through the thickness and gets deflected from the initial crack plane, we present the temporal and spatial concurrent evolution of MT and crack for LOR  $30^\circ$  in Figure 38. Originally, the entire crystal body

is tetragonal. In the early stages of the loading, among all 12 possible variants of monoclinic, only four monoclinic variants, i.e.,  $ABC$ ,  $ABC\bar{}$ ,  $BAC$  and  $BAC\bar{}$ , form at the crack tip because of the high stress concentration. The monoclinic variants rearrange to accommodate the maximum strain. The crack starts to grow when most of the crystal body has converted to monoclinic.



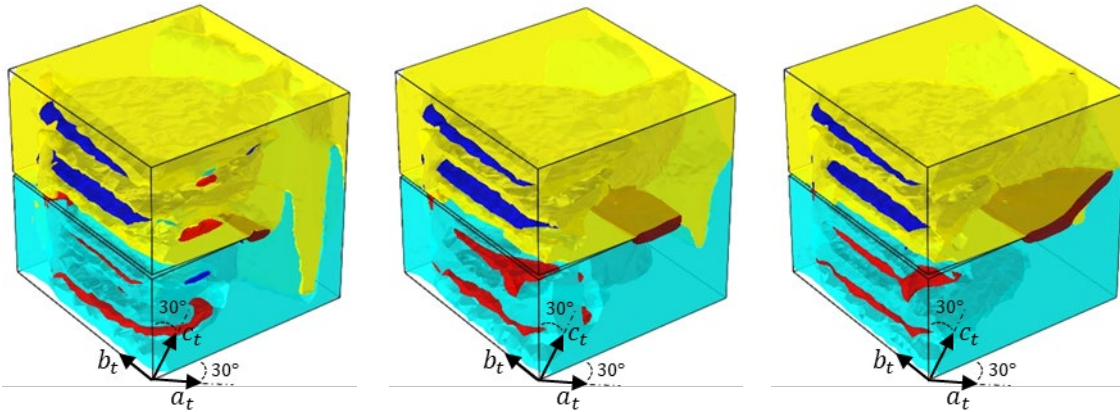


**Figure 34.** The temporal and spatial co-evolution of MT and crack for lattice orientation of 30 degrees in 3D single crystal zirconia.

To show the crack pattern clearly, we have removed the microstructure in Figure 39. Figure 39 (a)-(b) show that the crack starts growing at the  $t = 1100$  s at  $(0\bar{1}0)_t$  plane and then gradually propagates through the thickness. The difference in the crack growth amount is because of the phase transformation's local toughening effects, which vary at different locations, and consequently, these local monoclinic variants determine the stress states and crack growth driving force. This observation shows the impact of the local microstructure on the transformation toughening in shape memory ceramics. When monoclinic variants arrangement is in a way that produces more toughening, it is difficult for the crack to grow in some spots and vice versa. Figure 39(d) shows the crack pattern at  $t = 3500$  s. At this stage, the crack has deflected upward in the  $(0\bar{1}0)_t$  plane, while it is deflected slightly downward in the  $(010)_t$  plane. Interestingly the uneven crack tip pattern through the thickness is not uniform; it is parabolic initially and then gets linear, Figure 39(e). This behavior is because of the evolving microstructural patterns constructed from different monoclinic variants in each spot; they create different local stresses through the thickness. Therefore, the crack tip pattern is not uniform and grows more in areas with more favorable stress states. Looking more closely at the



microstructures, it turns out that the crack tip at  $(0\bar{1}0)_t$  plane is more surrounded by monoclinic variant  $ABC$  and have the monoclinic variant  $AB\bar{C}$  at the bottom. The configuration of monoclinic variants and the accommodated stress state in  $(0\bar{1}0)_t$  plane leads to the upward deflection of the crack, whereas crack tip in the  $(010)_t$  plane is surrounded almost evenly by variants  $ABC$  and  $AB\bar{C}$  which leads to slight downward deflection. The presence of monoclinic variants  $BAC$  in the  $(010)_t$  plane is the reason that the crack in this plane started very late compare to the other areas. Additionally, the middle part of the crack is surrounded by monoclinic variants  $\bar{C}$ , which made it difficult for this part of the crack to grow at the same pace as the other sections and eventually leading to the parabolic pattern of the crack tip in this area.

Since in this simulation we have lattice orientation of 30 degrees, the loading direction is not aligned with the  $c_t$ -axis and this leads to an unbalanced and un-symmetrical microstructural domain. This would result in uneven stress state at crack tip in different areas, resulting in an uneven crack growth throughout the thickness. The non-uniform growth of the crack tip through the thickness, which the 3D simulation enables us to observe, indicates to the local behavior of transformation toughening within a single crystal zirconia.

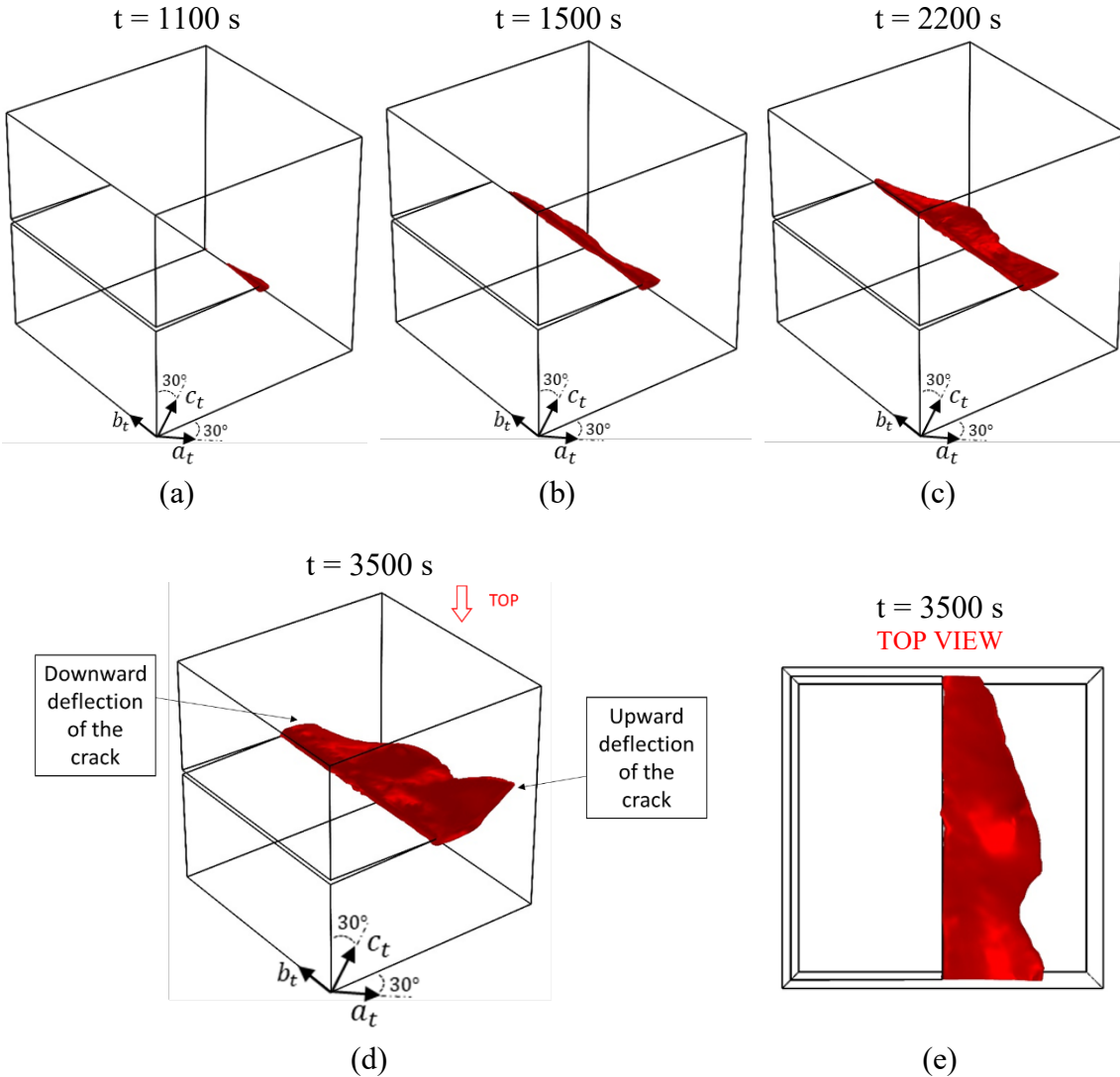


**Figure 35.** The Isosurface plots of the crack propagation in a single crystal zirconia for lattice orientation of 30 degrees around  $b_r$ -axis.

### Conclusion

This chapter presented a three-dimensional phase field model to study the concurrent evolution of martensitic transformation and crack growth in the shape memory ceramics. Zirconia is used as the model material with emphasis on the tetragonal to monoclinic transformation. The three-dimensional modeling empowers us to acquire all twelve variants of the monoclinic phase. By implementing all twelve monoclinic variants in the martensitic transformation model's equations and coupling them with the

variational formulation of fracture, the developed model predicts the experimentally observed results, such as the surface uplifting and self-accommodated martensite formation in the crack vicinity. The model also agrees with the experimentally observed fragmented transformed zones resulting from the crack propagation throughout the transformed planes. Investigating the lattice orientation effects on zirconia fracture reveals the “local” nature of transformation toughening within a single crystal. Results also show that the angles that the tetragonal axes make with the loading direction profoundly impact the selection of the monoclinic variants that nucleate at the crack tip and their further growth and eventual morphology and consequently on the crack growth path and toughening.

## CHAPTER SIX: CONCLUSION AND FUTURE WORKS

This dissertation attempts to provide a mathematical framework for fracture in shape memory ceramics that experience martensitic transformation. To address the shortage of classical methods, we have developed an anisotropic phase field model that coupled the Ginzburg-Landau equations of martensitic transformation to the variational formulation of brittle fracture based on the Griffith theory. The model is efficiently capable of predicting crack propagation in transformable materials.

We used zirconia as the model material for this study. In the first step, we started from the simplest model and constructed a model for single crystal zirconia. The phase transformation dramatically slows down the crack propagation and reduces the value of the normal stresses in front of the crack tip. The analysis of the crack growth behavior in single crystal zirconia shows an unusual crack growth path in the presence of the martensitic transformation. For mode I of fracture, the opening mode, crack shows an unusual propagation path that is in good agreement with the experiments and indicates the significant role of phase transformation on the crack propagation path. The investigation on the effect of lattice orientation on crack propagation shows that the lattice orientation has a considerable influence not only on the crack propagation path but also on the magnitude of the transformation toughening.

When the lattice orientation changed in the crystal, the final microstructure patterns would change after phase transition. Therefore, the stress state in the domain changed, and each spot in the field has different stress states that make it harder for the

crack to grow in some regions and easier to grow in some other areas to minimize the energy. This leads to the crack deflection and changes the magnitude of the transformation toughening. This mainly happened in the lattice orientations that cause the unsymmetrical final microstructures in the monoclinic phase.

At the second step, we expanded the single crystal model to polycrystalline by introducing the interfaces and grain boundaries into the model. The model is parameterized for tetragonal polycrystalline zirconia, and the experimental data from literature were used to validate the model. We employed an appropriate algorithm for generating polycrystalline geometry, making it feasible to implement models with different morphologies, grain sizes, and grain boundary sizes. The model predicts the three dominant crack propagation patterns observed experimentally, including the secondary crack initiation, crack branching, and grain bridging. The model shows the critical role of texture engineering in toughening enhancement. With grains that make low angles between the  $a$ -axis in the tetragonal phase and the crack plane, polycrystalline zirconia samples show higher transformation toughening due to maximum hydrostatic strain release perpendicular to the crack tip. The model also shows the grain boundary engineering as a way to enhance the transformation toughening. The maximum fracture toughness occurs at a specific grain size, and further coarsening or refinement reduces the fracture toughness. This optimum grain size results from the competition between the toughening enhancement and MT suppression with grain refinement.

In the final step, we expanded the model to 3D to capture more realistic results and overcome the lackings of the 2D model. The 2D model could not consider all monoclinic variants and some of the features was ignored. The developed three-

dimensional model considers all 12 monoclinic variants, making it possible to acquire realistic microstructures. Surface uplifting, self-accommodated martensite pairs formation, and transformed zone fragmentation were observed by the model, which agrees with the experimental observations. The influence of the crystal lattice orientation is investigated in this study, which changed the microstructure patterns and altered the transformation toughening and deflected the crack propagation path. Examining the lattice orientation effects on zirconia fracture reveals the “local” nature of transformation toughening within a single crystal. Results also show that the angles that the tetragonal axes make with the loading direction changed the selection of the monoclinic variants that nucleate at the crack tip and their further growth and eventual morphology and consequently on the crack growth path and toughening.

### **Future Works**

Cyclic degradation is one of the grand challenges in shape memory materials (SMMs). This work is the first step in our group toward addressing mechanical degradation in SMMs. In the following, we provide some information about how it is possible to expand this study in the future.

- Improve the model to consider heterogeneous fracture. The current study considers a fixed amount for critical energy release rate ( $G_c$ ) for both tetragonal and monoclinic phases. It was primarily because of the unavailability of the data in the literature. With recent advancements in interatomic potential development, atomistic simulations can be used to estimate  $G_c$  for both tetragonal and monoclinic.
- Expand the model to study the fatigue in SMCs. Based on the fracture framework developed in this study, it is possible to develop a fatigue phase field model, for

example see Carrara et al. [110]. Fatigue in SMCs has been the subject of extensive experimental studies at the macroscale. However, we are not aware of any microstructure-informed model that has elucidated the fundamental mechanisms of fatigue degradation in zirconia, or other SMCs.

- Enhance the model beyond ceramics. The fatigue and fracture of shape memory alloys have been important problems both in mechanical engineering and materials science communities. The primary challenge is related to the fracture model. While the variational formulation of fracture exists for brittle materials, it does not for ductile materials. Recently some models have been developed to address this challenge. This work would be a suitable starting point for studying mechanical degradations of shape memory alloys by adding plasticity to both phase transformation and fracture models.
- Improving the algorithms to enable simulations at the component scale. The current model has been applied to the microscale geometries. Expanding the model to the component scale would be very beneficial considering the wide range of applications of zirconia in aerospace to biomedical.

## REFERENCES

- [1] M. Asle Zaeem, N. Zhang, M. Mamivand, A review of computational modeling techniques in study and design of shape memory ceramics, *Comput. Mater. Sci.* 160 (2019) 120–136. doi:10.1016/j.commatsci.2018.12.062.
- [2] X.Q. Cao, R. Vassen, D. Stoeber, Ceramic materials for thermal barrier coatings, *J. Eur. Ceram. Soc.* 24 (2004) 1–10. doi:10.1016/S0955-2219(03)00129-8.
- [3] R.A. Miller, Current status of thermal barrier coatings — An overview, *Surf. Coatings Technol.* 30 (1987) 1–11. doi:10.1016/0257-8972(87)90003-X.
- [4] C. Piconi, G. Maccauro, Zirconia as a ceramic biomaterial, *Biomaterials.* 20 (1999) 1–25. doi:10.1016/S0142-9612(98)00010-6.
- [5] J. Chevalier, What future for zirconia as a biomaterial?, *Biomaterials.* 27 (2006) 535–543. doi:10.1016/J.BIOMATERIALS.2005.07.034.
- [6] I. Denry, J.R. Kelly, State of the art of zirconia for dental applications, *Dent. Mater.* 24 (2008) 299–307. doi:10.1016/J.DENTAL.2007.05.007.
- [7] R.H. Hannink, P.M. an. M. Kelly, B. C, Transformation toughening in zirconia-containing ceramics, *J. Am. Ceram. Soc.* 83 (2000) 461–487.
- [8] P.M. Kelly, L.R. Francis Rose, The martensitic transformation in ceramics — its role in transformation toughening, *Prog. Mater. Sci.* 47 (2002) 463–557. doi:10.1016/S0079-6425(00)00005-0.
- [9] J. Luo, Z.M. Xiao, Transformation toughening behavior of two edge cracks emanating from a circular hole in zirconia ceramics, *Int. J. Fract.* 131 (2005) 351–366. doi:10.1007/s10704-004-5678-1.
- [10] R.C. GARVIE, R.H. HANNINK, R.T. PASCOE, Ceramic steel?, *Nature.* 258 (1975) 703–704. doi:10.1038/258703a0.



- [11] A. Lai, Z. Du, C.L. Gan, C.A. Schuh, Shape Memory and Superelastic Ceramics at Small Scales, *Science* (80-. ). 341 (2013) 1505. doi:10.1126/science.1239745.
- [12] R.M. McMEEKING, A.G. EVANS, Mechanics of Transformation-Toughening in Brittle Materials, *J. Am. Ceram. Soc.* 65 (1982) 242–246. doi:10.1111/j.1151-2916.1982.tb10426.x.
- [13] B. Budiansky, J.W. Hutchinson, J.C. Lambropoulos, Continuum theory of dilatant transformation toughening in ceramics, *Int. J. Solids Struct.* 19 (1983) 337–355. doi:10.1016/0020-7683(83)90031-8.
- [14] J.C. LAMBROPOULOS, Effect of Nucleation on Transformation Toughening, *J. Am. Ceram. Soc.* 69 (1986) 218–222. doi:10.1111/j.1151-2916.1986.tb07411.x.
- [15] D.M. Stump, B. Budiansky, Crack-growth resistance in transformation-toughened ceramics, *Int. J. Solids Struct.* 25 (1989) 635–646. doi:10.1016/0020-7683(89)90030-9.
- [16] I.-W. Chen, Model of Transformation Toughening in Brittle Materials, *J. Am. Ceram. Soc.* 74 (1991) 2564–2572. doi:10.1111/j.1151-2916.1991.tb06800.x.
- [17] G.T.M. Stam, E. van der Giessen, P. Meijers, Effect of transformation-induced shear strains on crack growth in zirconia-containing ceramics, *Int. J. Solids Struct.* 31 (1994) 1923–1948. doi:10.1016/0020-7683(94)90200-3.
- [18] R.M. an. E. McMeeking, A. G, Mechanics of transformation-toughening in brittle materials, *J. Am. Ceram. Soc.* 65 (1982) 242–246.
- [19] B. Liu, N. Liu, J. Luo, Z. Xiao, Study of Transformation Toughening Behavior of an Edge Through Crack in Zirconia Ceramics with the Cohesive Zone Model, *Int. J. Appl. Mech.* 10 (2018) 1850066. doi:10.1142/S1758825118500667.
- [20] A.G. Evans, R.M. Cannon, Toughening of brittle solids by martensitic transformations, *Acta Metall.* 34 (1986) 761–800.
- [21] C. Cisse, W. Zaki, T. Ben Zineb, A review of modeling techniques for advanced effects in shape memory alloy behavior, *Smart Mater. Struct.* 25 (2016) 103001. doi:10.1088/0964-1726/25/10/103001.

- [22] T. Baxevanis, D.C. Lagoudas, Fracture mechanics of shape memory alloys: review and perspectives, *Int. J. Fract.* 191 (2015) 191–213. doi:10.1007/s10704-015-9999-z.
- [23] M. Mamivand, M. Asle Zaeem, H. El Kadiri, Phase field modeling of stress-induced tetragonal-to-monoclinic transformation in zirconia and its effect on transformation toughening, *Acta Mater.* 64 (2014) 208–219. doi:10.1016/j.actamat.2013.10.031.
- [24] A. Celli, A. Tucci, L. Esposito, C. Palmonari, Fractal analysis of cracks in alumina–zirconia composites, *J. Eur. Ceram. Soc.* 23 (2003) 469–479. doi:10.1016/S0955-2219(02)00148-6.
- [25] A. Onuki, Ginzburg-Landau Approach to Elastic Effects in the Phase Separation of Solids, *J. Phys. Soc. Japan.* 58 (1989) 3065–3068. doi:10.1143/JPSJ.58.3065.
- [26] L.-Q. Chen, A.G. Khachaturyan, Computer simulation of structural transformations during precipitation of an ordered intermetallic phase, *Acta Metall. Mater.* 39 (1991) 2533–2551. doi:10.1016/0956-7151(91)90069-D.
- [27] Y. Wang, A.G. Khachaturyan, Three-dimensional field model and computer modeling of martensitic transformations, *Acta Mater.* 45 (1997) 759–773. doi:10.1016/S1359-6454(96)00180-2.
- [28] M.A. Zaeem, S.D. Mesarovic, Morphological instabilities in thin films: Evolution maps, *Comput. Mater. Sci.* 50 (2011) 1030–1036. doi:10.1016/j.commatsci.2010.10.043.
- [29] M. Asle Zaeem, H. El Kadiri, S.D. Mesarovic, M.F. Horstemeyer, P.T. Wang, Effect of the Compositional Strain on the Diffusive Interface Thickness and on the Phase Transformation in a Phase-Field Model for Binary Alloys, *J. Phase Equilibria Diffus.* 32 (2011) 302–308. doi:10.1007/s11669-011-9905-y.
- [30] C. Miehe, M. Hofacker, F. Welschinger, A phase field model for rate-independent crack propagation: Robust algorithmic implementation based on operator splits, *Comput. Methods Appl. Mech. Eng.* 199 (2010) 2765–2778. doi:10.1016/j.cma.2010.04.011.

- [31] R. Spatschek, E. Brener, A. Karma, Phase field modeling of crack propagation, *Philos Mag.* 91 (2011) 75–95.
- [32] C. Kuhn, A continuum phase field model for fracture, *Eng. Fract. Mech.* 77 (2010) 3625–3634. doi:10.1016/j.engfracmech.2010.08.009.
- [33] V. Hakim, A. Karma, Laws of crack motion and phase-field models of fracture, *J. Mech. Phys. Solids.* 57 (2009) 342–368. doi:10.1016/j.jmps.2008.10.012.
- [34] A. Abdollahi, I. Arias, Phase-field simulation of anisotropic crack propagation in ferroelectric single crystals: effect of microstructure on the fracture process, *Model. Simul. Mater. Sci. Eng.* 19 (2011) 074010. doi:10.1088/0965-0393/19/7/074010.
- [35] W.J. Boettinger, J.A. Warren, C. Beckermann, A. Karma, Phase-Field Simulation of Solidification, *Annu. Rev. Mater. Res.* 32 (2002) 163–194. doi:10.1146/annurev.matsci.32.101901.155803.
- [36] C. Beckermann, H.-J. Diepers, I. Steinbach, A. Karma, X. Tong, Modeling Melt Convection in Phase-Field Simulations of Solidification, *J. Comput. Phys.* 154 (1999) 468–496. doi:10.1006/jcph.1999.6323.
- [37] M.A. Zaeem, H. Yin, S.D. Felicelli, Comparison of Cellular Automaton and Phase Field Models to Simulate Dendrite Growth in Hexagonal Crystals, *J. Mater. Sci. Technol.* 28 (2012) 137–146. doi:10.1016/S1005-0302(12)60034-6.
- [38] R. Kobayashi, Modeling and numerical simulations of dendritic crystal growth, *Phys. D Nonlinear Phenom.* 63 (1993) 410–423. doi:10.1016/0167-2789(93)90120-P.
- [39] L.-Q. Chen, Phase-Field Models for Microstructure Evolution, *Annu. Rev. Mater. Res.* 32 (2002) 113–140. doi:10.1146/annurev.matsci.32.112001.132041.
- [40] M. Mamivand, M.A. Zaeem, H. El Kadiri, A review on phase field modeling of martensitic phase transformation, *Comput. Mater. Sci.* 77 (2013) 304–311. doi:10.1016/j.commatsci.2013.04.059.

- [41] P.W. Anderson, E.I. Blount, Symmetry Considerations on Martensitic Transformations: &quot;Ferroelectric&quot; Metals?, *Phys. Rev. Lett.* 14 (1965) 217–219. doi:10.1103/PhysRevLett.14.217.
- [42] J.D. Axe, Y. Yamada, Cubic-tetragonal elastic phase transformations in solids, *Phys. Rev. B.* 24 (1981) 2567–2569. doi:10.1103/PhysRevB.24.2567.
- [43] Y.-W. Cui, T. Koyama, I. Ohnuma, K. Oikawa, R. Kainuma, K. Ishida, Simulation of hexagonal–orthorhombic phase transformation in polycrystals, *Acta Mater.* 55 (2007) 233–241. doi:10.1016/j.actamat.2006.07.026.
- [44] Y.H. Wen, Y. Wang, L.Q. Chen, Phase-field simulation of domain structure evolution during a coherent hexagonal-to-orthorhombic transformation, *Philos. Mag. A.* 80 (2000) 1967–1982. doi:10.1080/01418610008212146.
- [45] Y.H. Wen, Y. Wang, L.Q. Chen, Effect of elastic interaction on the formation of a complex multi-domain microstructural pattern during a coherent hexagonal to orthorhombic transformation, *Acta Mater.* 47 (1999) 4375–4386. doi:10.1016/S1359-6454(99)00247-5.
- [46] O. Shchyglo, U. Salman, A. Finel, Martensitic phase transformations in Ni–Ti-based shape memory alloys: The Landau theory, *Acta Mater.* 60 (2012) 6784–6792. doi:10.1016/j.actamat.2012.08.056.
- [47] W.Z. Zhu, Grain size dependence of the transformation temperature of tetragonal to monoclinic phase in ZrO<sub>2</sub>(Y<sub>2</sub>O<sub>3</sub>) ceramics, *Ceram. Int.* 22 (1996) 389–395. doi:10.1016/0272-8842(95)00120-4.
- [48] R.C. Garvie, Thermodynamic analysis of the tetragonal to monoclinic transformation in a constrained zirconia microcrystal, *J. Mater. Sci.* 20 (1985) 3479–3486. doi:10.1007/BF01113754.
- [49] M. Mamivand, M. Asle Zaeem, H. El Kadiri, L.-Q. Chen, Phase field modeling of the tetragonal-to-monoclinic phase transformation in zirconia, *Acta Mater.* 61 (2013) 5223–5235. doi:10.1016/J.ACTAMAT.2013.05.015.

- [50] C. Miehe, F. Welschinger, M. Hofacker, Thermodynamically consistent phase-field models of fracture: Variational principles and multi-field FE implementations, *Int. J. Numer. Methods Eng.* 83 (2010) 1273–1311. doi:10.1002/nme.2861.
- [51] M.J. Borden, C. V. Verhoosel, M.A. Scott, T.J.R. Hughes, C.M. Landis, A phase-field description of dynamic brittle fracture, *Comput. Methods Appl. Mech. Eng.* 217 (2012) 77–95. doi:10.1016/j.cma.2012.01.008.
- [52] C. Hesch, K. Weinberg, Thermodynamically consistent algorithms for a finite-deformation phase-field approach to fracture, *Int. J. Numer. Methods Eng.* 99 (2014) 906–924. doi:10.1002/nme.4709.
- [53] T. Rabczuk, *Computational Methods for Fracture in Brittle and Quasi-Brittle Solids: State-of-the-Art Review and Future Perspectives*, ISRN Appl. Math. 2013 (2013). doi:10.1155/2013/849231.
- [54] I. S. Aranson, V.A. Kalatsky, V. Vinokur, *Continuum Field Description of Crack Propagation*, 2000. doi:10.1103/PhysRevLett.85.118.
- [55] A. Karma, D.A. Kessler, H. Levine, Phase-Field Model of Mode III Dynamic Fracture, *Phys. Rev. Lett.* 87 (2001) 45501. doi:10.1103/PhysRevLett.87.045501.
- [56] R. Spatschek, E. Brener, A. Karma, Phase field modeling of crack propagation, *Philos. Mag.* 91 (2011) 75–95. doi:10.1080/14786431003773015.
- [57] L.O. Eastgate, J.P. Sethna, M. Rauscher, T. Cretegnny, C.-S. Chen, C.R. Myers, Fracture in mode I using a conserved phase-field model, *Phys. Rev. E.* 65 (2002) 36117. doi:10.1103/PhysRevE.65.036117.
- [58] H. Henry, H. Levine, Dynamic Instabilities of Fracture under Biaxial Strain Using a Phase Field Model, *Phys. Rev. Lett.* 93 (2004) 105504. doi:10.1103/PhysRevLett.93.105504.
- [59] B. Bourdin, G.A. Francfort, J.-J. Marigo, Numerical experiments in revisited brittle fracture, *J. Mech. Phys. Solids.* 48 (2000) 797–826. doi:https://doi.org/10.1016/S0022-5096(99)00028-9.

- [60] B. Bourdin, G.A. Francfort, J.-J. Marigo, The Variational Approach to Fracture, *J. Elast.* 91 (2008) 5–148. doi:10.1007/s10659-007-9107-3.
- [61] C. Kuhn, R. Müller, A phase field model for fracture, *Proc Appl Math Mech.* 8 (2008) 10223–10224.
- [62] H. Amor, J.J. Marigo, C. Maurini, Regularized formulation of the variational brittle fracture with unilateral contact: numerical experiments, *J Mech Phys Solids.* 57 (2009) 1209–1229.
- [63] M.J. Borden, H. Tjr, C.M. Landis, C. V Verhoosel, A higher-order phase-field model for brittle fracture: formulation and analysis within the isogeometric analysis framework, *Comput Methods Appl Mech Eng.* 273 (2014) 100–118.
- [64] L.D. Landau, E.M. Lifshitz, *Statistical physics*, Pergamon Press, Oxford, 1980.
- [65] G.A. Francfort, J.-J. Marigo, Revisiting brittle fracture as an energy minimization problem, *J. Mech. Phys. Solids.* 46 (1998) 1319–1342. doi:10.1016/S0022-5096(98)00034-9.
- [66] M. Ambati, T. Gerasimov, L. De Lorenzis, A review on phase-field models of brittle fracture and a new fast hybrid formulation, *Comput. Mech.* 55 (2015) 383–405. doi:10.1007/s00466-014-1109-y.
- [67] J.D. Clayton, J. Knap, Phase field modeling of directional fracture in anisotropic polycrystals, *Comput. Mater. Sci.* 98 (2015) 158–169. doi:https://doi.org/10.1016/j.commatsci.2014.11.009.
- [68] T.T. Nguyen, J. Réthoré, M.-C. Baietto, Phase field modelling of anisotropic crack propagation, *Eur. J. Mech. - A/Solids.* 65 (2017) 279–288. doi:https://doi.org/10.1016/j.euromechsol.2017.05.002.
- [69] T. Zhao, J. Zhu, J. Luo, Study of crack propagation behavior in single crystalline tetragonal zirconia with the phase field method, *Eng. Fract. Mech.* 159 (2016) 155–173. doi:10.1016/J.ENGFRACMECH.2016.03.035.

- [70] T. Coyle, W. Coblenz, B. A. Bender, Transformation Toughening in Large-Grain-Size CeO<sub>2</sub>-Doped ZrO<sub>2</sub> Polycrystals, *J. Am. Ceram. Soc.* 71 (2005) C-88-C-92. doi:10.1111/j.1151-2916.1988.tb05838.x.
- [71] A. Kumar, B. Sørensen, Fracture Resistance and Stable Crack-Growth Behavior of 8-mol%-Yttria-Stabilized Zirconia, *J. Am. Ceram. Soc.* 83 (2004) 1199–1206. doi:10.1111/j.1151-2916.2000.tb01354.x.
- [72] A.E. Lupercio, E. Moshkelgosha, R.C. Winters, C. Doyle, M. Mamivand, A.T. Nelson, B.J. Jaques, Ball-on-ring test validation for equibiaxial flexural strength testing of engineered ceramics, *Int. J. Ceram. Eng. Sci.* n/a (n.d.). doi:https://doi.org/10.1002/ces2.10085.
- [73] E. Moshkelgosha, M. Mamivand, Anisotropic Phase-Field Modeling of Crack Growth in Shape Memory Ceramics: Application to Zirconia, Vol. 12 *Adv. Mater. Des. Process. Charact. Appl.* 12 (2019) 9. doi:10.1115/IMECE2019-11695.
- [74] N. Moelans, B. Blanpain, P. Wollants, An introduction to phase-field modeling of microstructure evolution, *Calphad.* 32 (2008) 268–294. doi:10.1016/j.calphad.2007.11.003.
- [75] M. Mamivand, M. Asle Zaeem, H. El Kadiri, Shape memory effect and pseudoelasticity behavior in tetragonal zirconia polycrystals: A phase field study, *Int. J. Plast.* 60 (2014) 71–86. doi:10.1016/j.ijplas.2014.03.018.
- [76] M. Mamivand, M. Asle Zaeem, H. El Kadiri, Effect of variant strain accommodation on the three-dimensional microstructure formation during martensitic transformation: Application to zirconia, *Acta Mater.* 87 (2015) 45–55. doi:10.1016/j.actamat.2014.12.036.
- [77] L.D. LANDAU, *Collected Papers of L.D. Landau*, Oxford: Pergamon Press, 1965.
- [78] A. Khachaturyan, *Theory of structural transformations in solids*, 1983.
- [79] A. Hafver, E. Jettestuen, J. Feder, P. Meakin, A. Malthe-Sørensen, A node-splitting discrete element model for fluid-structure interaction, *Phys. A Stat. Mech. Its Appl.* 416 (2014) 61–79. doi:10.1016/j.physa.2014.08.039.

- [80] P.O. Bouchard, F. Bay, Y. Chastel, Numerical modelling of crack propagation: Automatic remeshing and comparison of different criteria, *Comput. Methods Appl. Mech. Eng.* 192 (2003) 3887–3908. doi:10.1016/S0045-7825(03)00391-8.
- [81] B. Carrier, S. Granet, Numerical modeling of hydraulic fracture problem in permeable medium using cohesive zone model, *Eng. Fract. Mech.* 79 (2012) 312–328. doi:10.1016/j.engfracmech.2011.11.012.
- [82] J. Oliver, A.E. Huespe, P.J. Sánchez, A comparative study on finite elements for capturing strong discontinuities: E-FEM vs X-FEM, *Comput. Methods Appl. Mech. Eng.* 195 (2006) 4732–4752. doi:10.1016/j.cma.2005.09.020.
- [83] A. Karma, D.A. Kessler, H. Levine, Phase-Field Model of Mode III Dynamic Fracture, *Phys. Rev. Lett.* 87 (2001) 045501. doi:10.1103/PhysRevLett.87.045501.
- [84] G.A. Francfort, J.J. Marigo, Revisiting brittle fractures as an energy minimization problem, *J Mech Phys Solids*. 46 (n.d.) 1319–1342.
- [85] S. Zhou, T. Rabczuk, X. Zhuang, Phase field modeling of quasi-static and dynamic crack propagation: COMSOL implementation and case studies, *Adv. Eng. Softw.* 122 (2018) 31–49. doi:10.1016/J.ADVENGSOFT.2018.03.012.
- [86] T.-T. Nguyen, J. Réthoré, J. Yvonnet, M.-C. Baietto, Multi-phase-field modeling of anisotropic crack propagation for polycrystalline materials, *Comput. Mech.* 60 (2017) 289–314. doi:10.1007/s00466-017-1409-0.
- [87] T.T. Nguyen, J. Yvonnet, Q.-Z. Zhu, M. Bornert, C. Chateau, A phase field method to simulate crack nucleation and propagation in strongly heterogeneous materials from direct imaging of their microstructure, *Eng. Fract. Mech.* 139 (2015) 18–39.
- [88] M.J. Borden, Isogeometric analysis of phase-field models for dynamic brittle and ductile fracture, The University of Texas at Austin, 2012. <http://hdl.handle.net/2152/ETD-UT-2012-08-6113>.
- [89] E. Moshkelgosha, M. Mamivand, Phase field modeling of crack propagation in shape memory ceramics – Application to zirconia, *Comput. Mater. Sci.* 174 (2020) 109509. doi:10.1016/J.COMMATSCI.2019.109509.



- [90] N.K. Simha, Twin and habit plane microstructures due to the tetragonal to monoclinic transformation of zirconia, *J. Mech. Phys. Solids*. 45 (1997) 261–292. doi:10.1016/S0022-5096(96)00074-9.
- [91] G.. Bansal, A.. Heuer, On a martensitic phase transformation in zirconia ( $ZrO_2$ )—II. Crystallographic aspects, *Acta Metall.* 22 (1974) 409–417. doi:10.1016/0001-6160(74)90093-5.
- [92] G.. Bansal, A.. Heuer, On a martensitic phase transformation in zirconia ( $ZrO_2$ )—I. Metallographic evidence, *Acta Metall.* 20 (1972) 1281–1289. doi:10.1016/0001-6160(72)90059-4.
- [93] A. Artemev, Y. Wang, A.. Khachaturyan, Three-dimensional phase field model and simulation of martensitic transformation in multilayer systems under applied stresses, *Acta Mater.* 48 (2000) 2503–2518. doi:10.1016/S1359-6454(00)00071-9.
- [94] A. Artemev, Y. Jin, A.G. Khachaturyan, Three-dimensional phase field model of proper martensitic transformation, *Acta Mater.* 49 (2001) 1165–1177. doi:10.1016/S1359-6454(01)00021-0.
- [95] E. Moshkelgosha, M. Mamivand, Concurrent modeling of martensitic transformation and crack growth in polycrystalline shape memory ceramics, *Eng. Fract. Mech.* (2020) 107403. doi:10.1016/j.engfracmech.2020.107403.
- [96] R. Quey, P.R. Dawson, F. Barbe, Large-scale 3D random polycrystals for the finite element method: Generation, meshing and remeshing, *Comput. Methods Appl. Mech. Eng.* 200 (2011) 1729–1745. doi:10.1016/J.CMA.2011.01.002.
- [97] R. Quey, L. Renversade, Optimal polyhedral description of 3D polycrystals: Method and application to statistical and synchrotron X-ray diffraction data, *Comput. Methods Appl. Mech. Eng.* 330 (2018) 308–333. doi:10.1016/J.CMA.2017.10.029.
- [98] M. Paggi, M. Corrado, J. Reinoso, Fracture of solar-grade anisotropic polycrystalline Silicon: A combined phase field–cohesive zone model approach, *Comput. Methods Appl. Mech. Eng.* 330 (2018) 123–148. doi:10.1016/J.CMA.2017.10.021.

- [99] C. Geuzaine, J.-F. Remacle, Gmsh: A 3-D finite element mesh generator with built-in pre- and post-processing facilities, *Int. J. Numer. Methods Eng.* 79 (2009) 1309–1331. doi:10.1002/nme.2579.
- [100] E. Moshkelgosha, E. Askari, K.H. Jeong, A.A. Shafiee, Fluid-structure coupling of concentric double FGM shells with different lengths, *Struct. Eng. Mech.* 61 (2017) 231–244. doi:10.12989/sem.2017.61.2.231.
- [101] P.E. REYES-MOREL, J.-S. CHERNG, I.-W. CHEN, Transformation Plasticity of CeO<sub>2</sub>-Stabilized Tetragonal Zirconia Polycrystals: II, Pseudoelasticity and Shape Memory Effect, *J. Am. Ceram. Soc.* 71 (1988) 648–657. doi:10.1111/j.1151-2916.1988.tb06383.x.
- [102] F.F. and B.J.H. Gupta T. K. and Lange, Effect of stress-induced phase transformation on the properties of polycrystalline zirconia containing metastable tetragonal phase, *J. Mater. Sci.* 13 (1978) 1464–1470. doi:10.1007/BF00553200.
- [103] J. Eichler, J. Rödel, U. Eisele, M. Hoffman, Effect of grain size on mechanical properties of submicrometer 3Y-TZP: fracture strength and hydrothermal degradation, *J. Am. Ceram. Soc.* 90 (2007) 2830–2836.
- [104] J. Eichler, M. Hoffman, U. Eisele, J. Rödel, R-curve behaviour of 2Y-TZP with submicron grain size, *J. Eur. Ceram. Soc.* 26 (2006) 3575–3582. doi:10.1016/J.JEURCERAMSOC.2005.11.012.
- [105] E. Moshkelgosha, M. Mamivand, Three-dimensional Phase Field Modeling of Fracture in Shape Memory Ceramics, *Int. J. Mech. Sci.* (2021).
- [106] M. Hayakawa, K. Adachi, M. Oka, Crystallographic analysis of the monoclinic herringbone structure in an arc-melted ZrO<sub>2</sub>-2 mol% Y<sub>2</sub>O<sub>3</sub> alloy, *Acta Metall. Mater.* 38 (1990) 1753–1759. doi:https://doi.org/10.1016/0956-7151(90)90017-B.
- [107] M. Hayakawa, N. Kuntani, M. Oka, Structural study on the tetragonal to monoclinic transformation in arc-melted ZrO<sub>2</sub>-2mol.%Y<sub>2</sub>O<sub>3</sub>—I. Experimental observations, *Acta Metall.* 37 (1989) 2223–2228. doi:https://doi.org/10.1016/0001-6160(89)90148-X.

- [108] M. Hayakawa, M. Oka, Structural study on the tetragonal to monoclinic transformation in arc-melted  $\text{ZrO}_2\text{-}2\text{mol.}\% \text{Y}_2\text{O}_3$ —II. Quantitative analysis, *Acta Metall.* 37 (1989) 2229–2235. doi:[https://doi.org/10.1016/0001-6160\(89\)90149-1](https://doi.org/10.1016/0001-6160(89)90149-1).
- [109] S. Deville, H. El Attaoui, J. Chevalier, Atomic force microscopy of transformation toughening in ceria-stabilized zirconia, *J. Eur. Ceram. Soc.* 25 (2005) 3089–3096. doi:<https://doi.org/10.1016/j.jeurceramsoc.2004.07.029>.
- [110] P. Carrara, M. Ambati, R. Alessi, L. De Lorenzis, A framework to model the fatigue behavior of brittle materials based on a variational phase-field approach, *Comput. Methods Appl. Mech. Eng.* 361 (2020) 112731. doi:<https://doi.org/10.1016/j.cma.2019.112731>.